Triple-resonant Frequency Conversion in Gallium Phosphide Integrated Photonic Resonators

Alan Logan

A dissertation
submitted in partial fulfillment of the
requirements for the degree of

Doctor of Philosophy

University of Washington

2023

Reading Committee:

Kai-Mei C. Fu, Chair

Arka Majumdar

Mo Li

Program Authorized to Offer Degree:
Electrical and Computer Engineering

University of Washington

Abstract

Triple-resonant Frequency Conversion in Gallium Phosphide Integrated Photonic Resonators

Alan Logan

Chair of the Supervisory Committee:
Professor Kai-Mei C. Fu
Electrical and Computer Engineering

The development of scalable quantum repeaters to extend entanglement distribution beyond the transmission range of single photons is vital to the implementation large-scale quantum networks, which could be used to secure communications with quantum key distribution among other applications. Quantum emitters that can be entangled remotely, such as the diamond nitrogen-vacancy (NV) center, can be used as memory-based quantum repeaters. However, the maximum practical distance between repeaters is limited by high attenuation in optical fiber at the emission wavelength of NV centers (637 nm) and similar emitters. Scalable frequency conversion of single photons from the emission wavelength to a low-loss telecom band would extend the remote entanglement range, reducing cost and improving performance of a fiber-based quantum repeater network. As a step toward low-power visible-to-telecom single-photon frequency conversion for diamond NV centers, this thesis presents frequency conversion of coherent light inputs with quasi-phase matched multi-resonant enhancement in gallium phosphide (GaP) nonlinear ring resonators on a silicon oxide substrate. The methods for designing, fabricating, and testing the GaP ring resonators and input/output coupling structures are presented, including tests for quickly and reliably identifying devices that are close to double or triple resonance. In the first two design generations, double-resonant quasi-phase matched (QPM) second harmonic generation (SHG) from telecom (1550 nm) to near-visible (775 nm) wavelengths is demonstrated with a small-signal conversion efficiency of up to 400%/W. In the third design generation, triple-resonant, quasi-phase matched sum-frequency generation (SFG) from the telecom C-band (1532 nm) to visible red (647 nm) is realized with a small-signal photon conversion efficiency of 2100-4000%/W. On-chip conversion efficiencies as high as 45,000%/W are projected to be attainable in GaP ring resonators, indicating that GaP nonlinear resonators are a promising and competitive platform for extending entanglement range by frequency conversion.

TABLE OF CONTENTS

Page

LIST OF FIGURES

LIST OF TABLES

ACKNOWLEDGMENTS

I would like to thank the many people who made this project possible:

Michael Gould, for helping get this project started, as well as actually fabricating the first generations of devices.

Emma Schmidgall, for training in fabrication processes and assistance in device characterization. I still haven't gotten the SEM to look that good.

Shivangi Shree, for invaluable assistance in testing and analyzing the third generation devices.

Srivatsa Chakravarthi, for constant efforts in refining and adapting the GaP fabrication process, which gave my chips some hope of actually working. Also, thank you for suggesting that the supercontinuum laser could be used for frequency conversion.

Fariba Hatami and Karine Hestroffer, for growing the high-quality GaP membranes used in this project.

Alejandro Rodriguez and Zin Lin, for assistance with the theoretical model used for device design.

Arka Majumdar, for lending the lasers and test setup used to test the first two generations of devices.

Mo Li, for lending the EOM and AOM that made high power frequency conversion measurements possible.

N. Shane Patrick, for assistance with troubleshooting and optimizing the electron beam lithography process.

...and many more, especially everyone else in the UW Quantum Defect Lab, past and present. I try to remember everything, but not all at the same time.

DEDICATION

Dear grad students of the future: here's what I've figured out so far.

Chapter 1

INTRODUCTION

The development of quantum networks for long-range entanglement distribution is currently a subject of global interest. Fast, reliable entanglement of distant qubits would allow multiple quantum computers to be combined into a unified cluster with vastly expanded computation capabilities. Quantum information processing promises efficient solutions to mathematical problems that are costly or intractable for classical computation, such as detailed simulations of complex molecules and materials or search and optimization problems in difficult parameter spaces. Entangled qubit pairs can also be used for quantum key distribution (QKD), providing cryptographic communication security that is not vulnerable to mathematical decryption, including decryption by quantum computers. However, the implementation of the sprawling quantum networks required for practical quantum key distribution or networked quantum computing is hindered by the difficulty of transmitting quantum states, typically encoded in single photons, over long distances. QKD has been demonstrated through 420 km of optical fiber [10] and in free space between a low-orbit satellite and ground [37]. However, reliable, scalable quantum repeaters are required to extend a network beyond the transmission range of a single photon.

A memory-based quantum repeater can be implemented by entangling each endpoint qubit with a different intermediate qubit in a repeater node [59]. A Bell measurement on the intermediate qubits teleports the entanglement to the endpoints. This process can be repeated to entangle qubits at arbitrary distances, which can then be used for QKD or other quantum computation algorithms [6]. This type of quantum repeater requires memory qubits that can be entangled remotely [59, 7], such as the negatively-charged nitrogen-vacancy (NV) in diamond. The NV center's spin-dependent optical transition allows heralded entanglement between two centers if indistinguishable photons from both can be measured at some intermediate point [7, 52]. The range for direct entanglement

between two qubits is still limited by photon transmission. Ideally, a large-scale quantum network would be able to use existing telecommunication infrastructure for entanglement distribution. Complicating this goal, the NV center and other qubit candidates with optical and coherence properties favorable for use as repeaters do not emit light in low-loss telecommunication wavelength bands. The increased attenuation at the emission wavelengths imposes uneconomical constraints on the maximum distance between repeaters, substantially increasing the cost and complexity of building and maintaining a quantum network.

The practical range of entanglement could be extended by converting the photons from the qubit's emission wavelength into a telecom band by quantum frequency conversion (QFC), which is frequency conversion involving non-classical states of light. Frequency conversion processes use the nonlinear susceptibility of a medium to couple modes of light at disparate frequencies, with conversion efficiency scaling with field strength. Typically, macroscopic optical cavities (such as large-etalon resonators [22, 71, 38, 76]) or waveguides [72, 17] are used to concentrate light and engineer modes at the desired wavelengths to satisfy the requisite phase matching conditions [13]. However, the small footprint, low mode volume, and wider bandwidth offered by integrated photonic devices could drastically improve scalability in size, cost, and power consumption [34, 15, 35, 56, 27, 28, 47, 53, 48].

As a step toward low-power visible-to-telecom QFC for diamond NV centers, this thesis presents frequency conversion of coherent light inputs with quasi-phase matched multi-resonant enhancement in gallium phosphide (GaP) nonlinear ring resonators on a silicon oxide substrate. Gallium phosphide was selected as the nonlinear photonic material due to its high refractive index and high second-order nonlinearity for a material that is transparent into the visible band, which makes it particularly promising for converting photons from diamond NV centers and other solid-state quantum emitters to telecom wavelengths. Ring resonators combine high intrinsic quality factors with moderately small mode volumes to provide strong enhancement to mode field strength and nonlinear interactions, while allowing resonant modes and coupling to be controlled with a small number of intuitive design variables. In the first two design generations, double-resonant quasi-phase matched (QPM) second harmonic generation (SHG) from telecom (1550 nm) to near-visible (775 nm) wavelengths is demonstrated with a small-signal power conversion efficiency of up to 400%/W. In

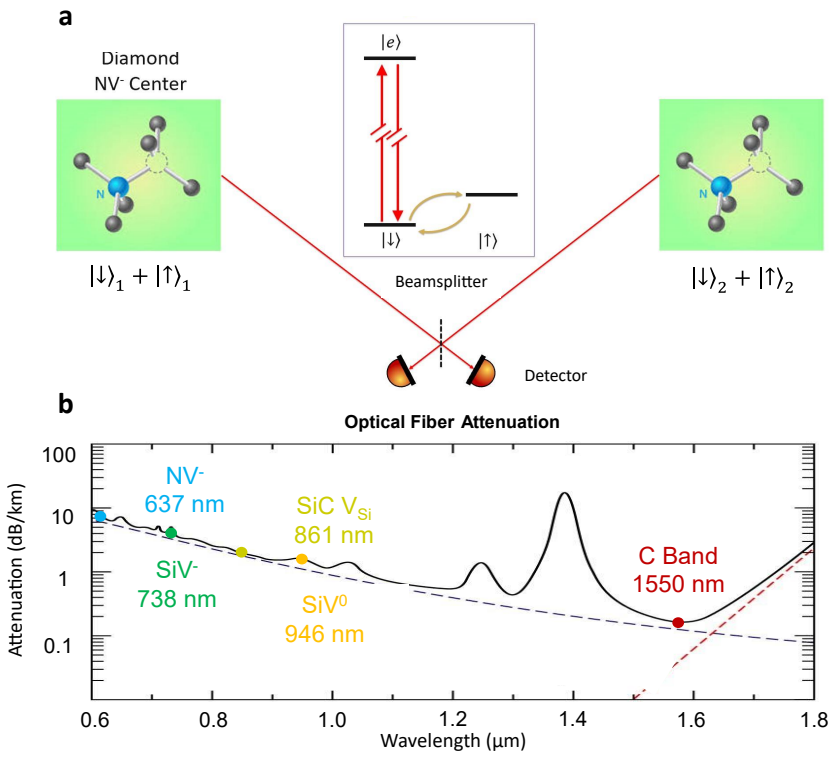

Figure 1.1: (a) Diagram of the measurement used for long-distance heralded entanglement of diamond NV centers and similar quantum emitters, with the required features of the NV center's energy levels. The spin-dependent optical transition produces spin-entangled photons from each emitter. The spin-entangled photons must be indistinguishable at the beamsplitter for the mutual measurement to project the emitter spins into an entangled state. Entanglement generation rate scales quadratically with transmission and detection efficiency [7], or linearly with some loss of fidelity [30]. (b) Zero-photon emission wavelengths of the diamond NV center and other solid state qubit candidates, with the attenuation in silica optical fiber of each emission wavelength compared to the minimum-loss telecommunication C band. Fiber attenuation plot reproduced from Ref. [62].

the third design generation, triple-resonant, quasi-phase matched sum-frequency generation (SFG) from the telecom C-band to visible red is realized with an on-chip small-signal photon conversion efficiency of 2100-4000%/W, which means that attaining a 1% photon conversion with this device requires only 250-475 μW of pump power. However, increasing the pump power causes the conversion efficiency to saturate well before it reaches 100%. Based on the measured performance of fabricated devices, small-signal conversion efficiencies as high

as 45,000%/W are projected to be attainable in GaP ring resonators. This efficiency would be sufficient for practical applications in long-distance entanglement distribution and is at least competitive with other reported frequency conversion platforms.

1.1 Background

1.1.1 Ring Resonators

Ring resonators are a type of photonic resonator that confine light using a bent (curved) waveguide to guide it in a complete loop. The high refractive index core of the waveguide confines light of free-space wavelength λ_0 by total internal reflection in the radial ($\hat{r}$) and vertical ($\hat{z}$) directions while allowing it to propagate in the azimuthal ($\hat{\theta}$) direction with an effective wavelength $\lambda_{eff} = \lambda_0/n_{eff}$, where n_{eff} is the effective index of a propagating mode. The bent waveguide cross-section can often support multiple transverse modes with different field distributions and n_{eff} for a given free-space wavelengths. First, modes can be transverse-electric (TE), with the electric field primarily polarized in the plane of the ring, or transverse-magnetic (TM) with a vertically-polarized electric field. TE and TM polarized modes with similar n_{eff} can hybridize to form diagonally polarized modes. For each polarization, the fundamental mode with the highest value of n_{eff} has a single field intensity peak in the cross-section of the mode. As the height and width of the ring increase, higher-order modes with additional field intensity peaks may be supported. For this thesis, ring modes will be described with the format $TE_{a,b}$, where TE (or TM) is the mode polarization, and a and b are the vertical and radial mode numbers indicating how many times the mode is split on each axis. For example, the fundamental TE mode would be indicated with $TE_{0,0}$, while a TM mode with four intensity peaks arranged horizontally would be $TM_{0,3}$. Examples of both of these modes can be found in Fig. 2.1a. In general, increasing the height, width, or material refractive index of the bent waveguide increases n_{eff} for all modes, with varying sensitivity.

A propagating mode in the bent waveguide will form a resonant mode in the ring resonator if the ring circumference is an integer multiple of the effective wavelength for that mode, so that the phase does not change after propagating around the ring:

$$2\pi r = m\lambda_{eff} \tag{1.1}$$

where integer m is the azimuthal mode number and r is the radius of the ring. The ring radius can be measured to any part of the ring, such as the inner edge or center of the waveguide, so long as a consistent definition is used throughout the analysis. Each transverse mode supported by the bent waveguide forms a family of similar ring resonances at different wavelengths, with azimuthal mode number increasing for shorter wavelengths. The wavelength difference between a resonance at free-space wavelength λ_0 and a consecutive resonance in the same family, or free spectral range (FSR), is determined by the roundtrip time t_R required for light to propagate around the ring in the mode:

$$\Delta\lambda_{FSR} = \frac{\lambda_0^2}{c\,t_R} T_R = \frac{2\pi r n_g}{c} n_g = n_{eff} - \lambda_0 \frac{dn_{eff}}{d\lambda_0} \tag{1.2}$$

where c is the speed of light in vacuum and n_g is the group index of the ring mode. Shown in Fig. 1.2b, The free spectral range is particular to each family of resonances, so it can be used for mode identification.

The quality factor Q of a resonance is the inverse of the fraction of energy lost from the mode during each optical cycle. A resonator with high Q retains light longer, allowing higher resonant field intensities to accumulate while exaggerating the effect of destructive interference on off-resonant wavelengths. Consequently, the resonance full-width half-max (FWHM) linewidth $\Delta\lambda$ decreases with higher Q:

$$\Delta\lambda = \frac{\lambda_0}{Q}. \tag{1.3}$$

The total quality factor Q is composed of the intrinsic quality factor Q_i and coupling quality factor Q_c:

$$\frac{1}{Q} = \frac{1}{Q_i} + \frac{1}{Q_c} \tag{1.4}$$

The intrinsic quality factor Q_i results from losses arising in the ring resonator itself. All modes in even an ideal ring structure would lose energy to radiation or absorption in the resonator material, though these loss mechanisms are often dominated by scattering from

surface roughness and other fabrication-related imperfections. The coupling quality factor Q_c is from energy transferring between the resonant mode and a specific input/output mode, which is usually deliberately added to provide access to the resonator as shown in Fig. 1.2a.

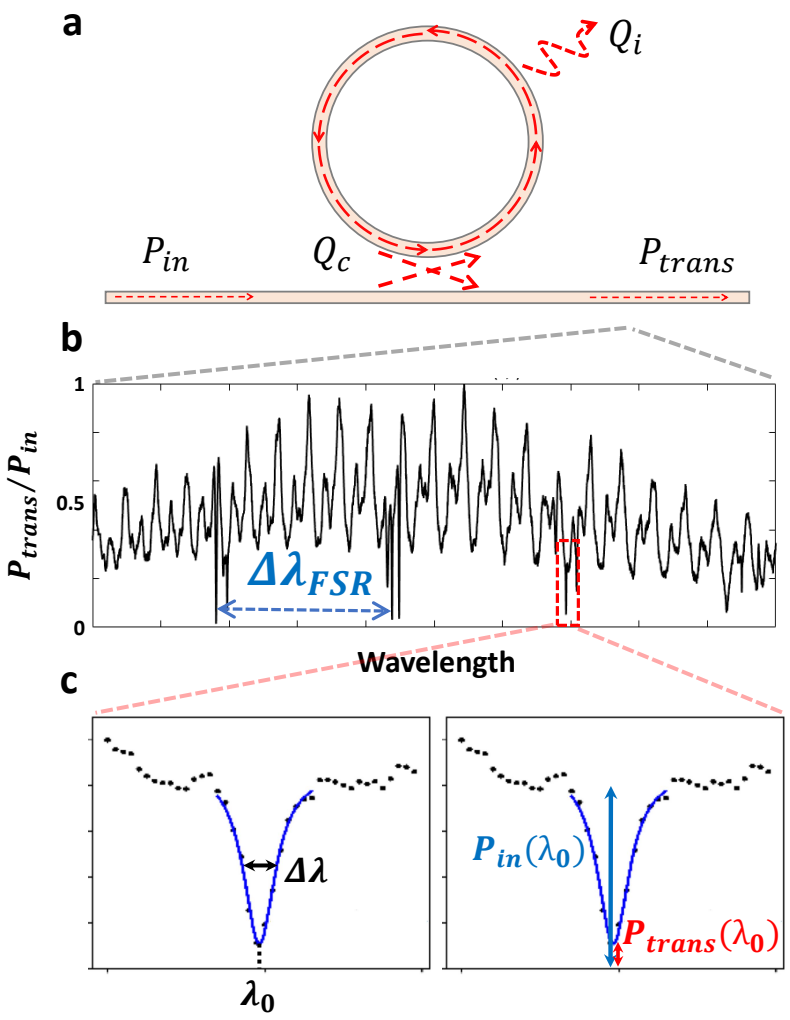

Figure 1.2: (a) Diagram of a ring resonator coupled to waveguide, with the intrinsic and coupling loss mechanisms labeled. (b) Example of a measured transmission spectrum of the coupled waveguide. Multiple families of ring resonances with slightly different free spectral ranges can be seen as sharp transmission dips superimposed on the background interference pattern. (c) Detail of a the transmission dip of a single coupled resonance, with a Lorentzian fitted curve (blue). On the left, the center wavelenth λ_0 and full-width half-max linewidth $\Delta\lambda$ of the Lorentzian are used to calculate total quality factor Q of the resonance. On the right, the measured values used to calculate residual transmission T are shown. This resonance is close to critically coupled, so T is near zero.

Energy stored in the resonator is split between the intended output mode and the intrinsic loss mechanisms, with a fraction equal to the coupling ratio Γ going to the output

mode:

$$\Gamma = \frac{Q}{Q_c} = \frac{Q_i}{Q_c + Q_i}. \tag{1.5}$$

The ring resonators used in this project have the ring modes evanescently coupled to waveguide modes, with a field coupling coefficient k between the two modes. A pulse of light in the ring mode loses a fraction of its energy $|k|^2$ each time it passes the waveguide coupling region, once per round trip, resulting in a coupling quality factor of

$$Q_c = \frac{t_R\, c}{\lambda_0} \frac{1}{|k|^2} = \frac{2\pi r n_g}{\lambda_0} \frac{1}{|k|^2}. \tag{1.6}$$

Similarly, a portion of incident light in the waveguide couples into the resonator, and the transmitted light interferes with light coupling out of the resonator. This results in a Lorentzian dip in transmission that matches the linewidth of the resonance, with a residual transmission T that depends on the coupling ratio Γ:

$$T = \frac{P_{trans}(\lambda_0)}{P_{in}(\lambda_0)} = |1 - 2\Gamma|^2 = \left| \frac{Q_i - Q_c}{Q_i + Q_c} \right|^2 \tag{1.7}$$

If the resonator is critically coupled ($\Gamma = 0.5$), transmission past the resonator goes to zero. Some residual transmission remains if the resonator is either undercoupled ($\Gamma < 0.5$) or overcoupled ($\Gamma > 0.5$), though power transmission measurements do not distinguish between the two cases. A resonance that is close to critical coupling is shown in Fig. 1.2c.

1.1.2 $\chi^{(2)}$ Frequency Conversion

Three-wave mixing is a coherent frequency conversion process that uses the second-order nonlinear susceptibility $\chi^{(2)}$ of a material to provide coupling between three modes at different frequencies. When light interacts with a medium, the electric field $\vec{E}$ deforms electron shells, inducing a polarization $\vec{P}$ based on the susceptibility χ of the medium:

$$\vec{P} = \chi^{(1)}\vec{E} + \chi^{(2)}\vec{E}\vec{E} + \chi^{(3)}\vec{E}\vec{E}\vec{E} + \ldots \tag{1.8}$$

In most circumstances, most of the polarization in the medium is due to the linear susceptibility $\chi^{(1)}$. As illustrated in Fig. 1.3a, the linear interaction between light and matter does not result in any interactions between photons. Consequently, if light is input at multiple frequencies, the output will consist of the same frequencies, with no new frequencies produced or energy transferred between input frequencies. In a material with nonzero $\chi^{(2)}$, there is a component of electron shell polarization $\vec{P}$ that is proportional to the square of an applied electric field $\vec{E}$ in addition to the usual linear response:

$$\vec{P}_k^{(2)} = \chi_{ijk}^{(2)} \vec{E}_i \cdot \vec{E}_j, \tag{1.9}$$

where i, j, and k are crystallographic directions. The quadratic dependence adds frequency components to the material polarization at the sum and difference of every pair of frequencies contained in the electric field, shown in Fig. 1.3b. The oscillating electron shells act as light

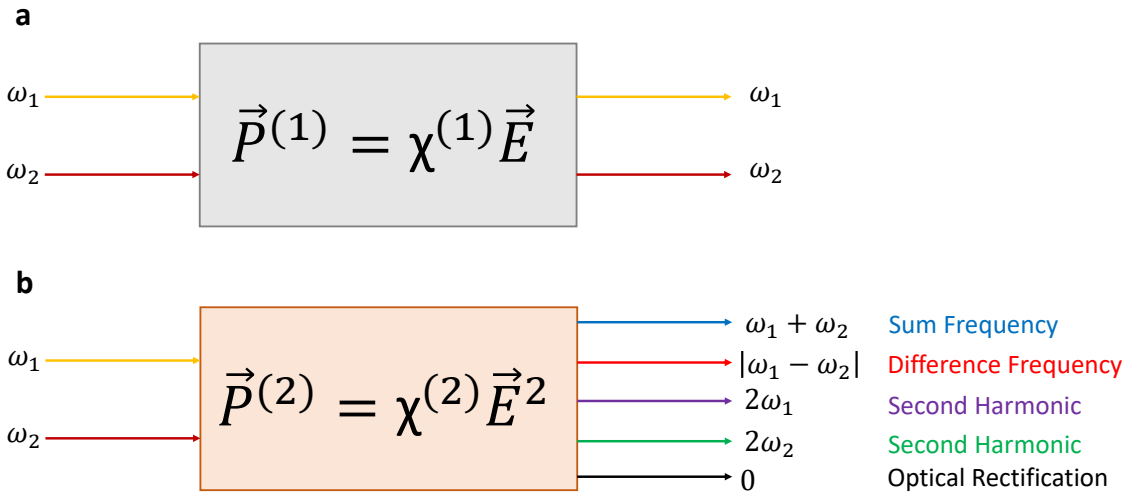

Figure 1.3: (a) Interactions between light at two input frequencies and the linear susceptibility of a material. Each frequency passes through the material unmodified. (b) Interactions between the same two input frequencies with the second-order susceptibility $\chi^{(2)}$. The electron shell polarization now depends quadratically on the electric field, so the input frequencies interact to produce components of polarization at every sum and difference of input frequencies. Output light is produced at these new frequencies.

sources at these new frequencies, enabling light at two input frequencies to interact and produce light at different frequencies via the nonlinear medium.

Like any material property, the $\chi^{(2)}$ of a given material is at least as symmetrical as that material. Consequently, a particular crystal symmetry may require some components of the second-order susceptibility $\chi^{(2)}_{ijk}$ to be zero. Notably, second-order nonlinear susceptibility inherently violates centrosymmetry, so every component vanishes entirely in the bulk of centrosymmetric crystals such as silicon and diamond. If a combination of crystallographic directions i, j and k is indistinguishable to another combination due to crystal symmetry, the corresponding $\chi^{(2)}_{ijk}$ components will be equal. Families of $\chi^{(2)}_{ijk}$ components that always share the same value (zero or nonzero) are often grouped into single tensor components d_{ij}. For example, $d_{36} = \chi^{(2)}_{ijk}/2$ for $i \neq j \neq k$ [13]. The optical properties of some common $\chi^{(2)}$ materials, including GaP, are shown in Table 1.1.

Three-wave mixing processes involve three photons with frequencies ω_1, ω_2, and ω_3, with ω_3 as the highest. The primary types are sum-frequency generation (SFG), which merges photons from two input modes to form a single photon in a higher frequency mode, and difference-frequency generation (DFG), which splits a photon into two lower energy photons. Energy is conserved in either case; the sum of frequencies of the initial photon(s) is equal to the sum of frequencies of the final photon(s): $\omega_1 + \omega_2 = \omega_3$. Degenerate conversion processes using two identical lower-frequency photons ($\omega_1 = \omega_2$) are possible. In particular, degenerate SFG is called second harmonic generation (SFG) or frequency doubling, in which $\omega + \omega \rightarrow 2\omega$.

The direction of energy transfer in a three-wave mixing process depends on the phase of field in the high-energy mode relative to the product of the fields in the two lower-energy modes. In order to maintain the same relative phase and avoid back-conversion, the propagation constants $k_i = \lambda_{0,i}/n_{eff,i}$ for the three modes must satisfy

$$k_1 + k_2 = k_3. \tag{1.10}$$

This condition is called phase matching, which also guarantees conservation of momentum. In bulk materials, phase matching can be achieved using carefully controlled mode polariza-

tions in birefringent crystals. In waveguides and photonic resonators, the mode distribution and propagation properties can be controlled using structure dimensions, instead. Alternatively, back-conversion can be averted by alternating the sign of $\chi^{(2)}$, which is determined by crystal orientation. This approach is called quasi-phase matching (QPM) and is frequently implemented by periodic poling or orientation patterning in both bulk crystals and waveguides.

The focus of this work is to use frequency conversion as an interface between an input and an output mode at different wavelengths, so the power conversion efficiency will be defined as $\eta = P_{out}/P_{in}$. The third mode, which is required to satisfy conservation of energy, is designated as the pump mode with power P_{pump}. Because the amplitude of the polarization oscillation from second-order susceptibility is quadratically dependent on the electric field, the strength of the nonlinear interaction between modes increases with field intensity. In general, $\eta = P_{out}/P_{in}$ increases with pump power P_{pump} until the input approaches complete conversion or the high power starts affecting the photonic structure, such as by heating or electro-optic effects. For a relatively weak input and pump that does not significantly affect the power in either mode, the conversion efficiency increases linearly with pump power. In this case, a small-signal conversion efficiency $\eta_{ss} = P_{out}/P_{in}P_{pump}$ with units of W^{-1} is used to describe the efficiency of the frequency conversion device. Concentrating light in a waveguide or photonic resonator enhances the field intensity, which increases η_{ss} and can reduce the power required to reach a target absolute conversion efficiency.

Material	Crystal	Refractive Index		Bandgap	Nonlinearity
		$\lambda_0 = 637\,nm$	$1550\,nm$	(pm/V)	(eV)
GaP	Zincblende	3.31	3.05	2.24	$d_{36} \approx 50 - 80$
GaAs	Zincblende	—	3.38	1.44	$d_{36} \approx 100 - 170$
$LiNbO_3$	Trigonal	2.28	2.21	4	$d_{31} \approx 6$ $d_{33} \approx 33$
AlN	Wurtzite	2.15	2.12	6.01	$d_{33} \approx 4.3$

Table 1.1: Material properties critical to the performance of nonlinear photonic devices for GaP and other $\chi^{(2)}$ materials. For comparison, the diamond NV center zero-phonon emission line is 637 nm $\approx$ 1.946 eV.

Frequency conversion in a multi-resonant nonlinear resonator can be described using coupled mode theory (CMT) with leaky modes [16]. For a triple-resonant SFG process from ω_1 to ω_3 with a pump at frequency $\omega_2 = \omega_3 - \omega_1$, the resonator has resonant modes with field intensities a_1, a_2, and a_3 for each frequency. Each resonator mode k has a total quality factor Q_k, composed of intrinsic quality factor $Q_{k,i}$ and coupling quality $Q_{k,c}$ from coupling to an incident mode s_k^+ and outgoing mode s_k^-. The incident modes carry light for the input modes 1 and 2, while there is no excitation at the converted frequency ($s_k^+ = 0$). Defining a decay rate $\gamma_k = \omega_k/2Q_k$ and coupling ratio $\Gamma_k = Q_k/Q_{k,c}$ for each mode, the coupled mode equations for this system are [16]:

$$\frac{da_1}{dt} = -\gamma_1 a_1 - i\omega_1 \beta a_2 a_3 + \sqrt{2\gamma_1 \Gamma_1} s_1^+ \tag{1.11}$$

$$\frac{da_2}{dt} = -\gamma_2 a_2 - i\omega_2 \beta a_1 a_3 + \sqrt{2\gamma_2 \Gamma_2} s_2^+ \tag{1.12}$$

$$\frac{da_3}{dt} = -\gamma_3 a_2 - i\omega_3 \beta^* a_1 a_2 \tag{1.13}$$

$$s_k^- = \sqrt{2\gamma_k \Gamma_k} a_k - s_k^+. \tag{1.14}$$

This model assumes that the three resonant modes exactly match the three process frequencies. Detuning reduces field enhancement and can introduce a small deviation from phase matching, weakening the nonlinear interaction. The nonlinear overlap β is calculated from the field overlap of the three modes, with field polarizations interacting through the $\chi^{(2)}$ of the material [16]:

$$\beta = \frac{1}{4\sqrt{\varepsilon_0}} \frac{\int \left[\sum_{i,j,k} \chi^{(2)}_{ijk} E^*_{3,i} \left(E_{1,j} E_{2,k} + E_{1,k} E_{2,j}\right)\right] d^3\vec{x}}{\sqrt{\int \epsilon_{r,1} |\vec{E}_1|^2 \, d^3\vec{x}} \sqrt{\int \epsilon_{r,2} |\vec{E}_2|^2 \, d^3\vec{x}} \sqrt{\int \epsilon_{r,3} |\vec{E}_2|^2 \, d^3\vec{x}}}, \tag{1.15}$$

where ε_0 is the permittivity of free space and ϵ_r is the relative linear permittivity of the material at each the wavelength of each mode. Smaller mode volumes and more similar mode field distributions increase β. The nonlinear overlap also includes the effects of phase matching and mode polarization. For degenerate frequency conversion processes such as SHG, β is reduced by a factor of two for the up-conversion term in mode 3 (Eq. 1.13).

The primary concern in this work is frequency conversion efficiency in a nonlinear res-

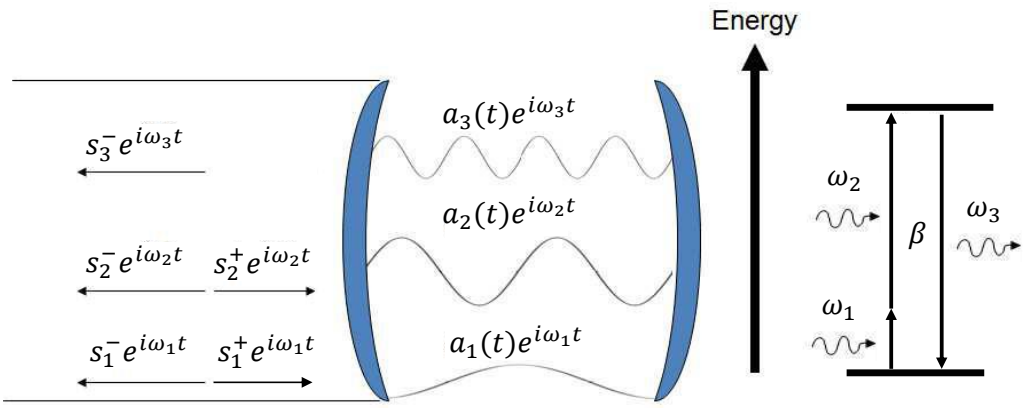

Figure 1.4: Diagram of a triple-resonant cavity-enhanced sum frequency generation process. Figure reproduced from Ref. [16] with minor modifications for notation.

onator under continuous-wave (CW) or quasi-CW excitation with an undepleted pump. Quasi-CW excitation assumes that the time scale for variations in the incident modes are substantially longer than the bandwidth-limited times of the resonant modes, so that the system mostly operates in steady state. The undepleted pump approximation requires that the frequency conversion process does not significantly affect the field intensity in the resonator pump mode, so the nonlinear term for a_2 in Eq. 1.12 can be neglected. Satisfying this condition ensures a consistent coupling rate between the input and output modes that is independent of input power, so conversion efficiency is defined only by pump power. For SHG, the input mode acts as it own pump, so converting input light with significant efficiency necessarily changes the power in the 'pump' mode. Nondegenerate SFG and DFG can reach near-unity conversion efficiency with an undepleted pump so long as the photon coupling rate between the resonator and waveguide pump modes is much greater than the photon conversion rate between the input and output. This ensures that the power in the pump resonator mode is not significantly affected by the pump photons that are created or destroyed by the frequency conversion.

Under these conditions, the external power conversion efficiency measured from incident input mode to outgoing converted mode can be derived from numerical steady-state solutions of the system of equations in Eq. 1.11-1.14:

$$\eta = \frac{P_{3,out}}{P_{1,in}} = \frac{\left|s_3^-\right|^2}{\left|s_1^+\right|^4} \approx \frac{\eta_{ss} P_{2,in}}{\left(1 + \frac{\eta_{ss} P_{2,in}}{4\eta_{max}}\right)^2}, \tag{1.16}$$

where η_{ss} and η_{max} are the small-signal and maximum conversion efficiencies, respectively. The conversion efficiency initially increases linearly with pump power $P_{2,in}$ with a slope of η_{ss}. The maximum conversion efficiency is reached at total internal conversion, when all input light that couples into the resonator is either converted or lost to intrinsic mechanisms. Increasing pump power beyond this point results in back conversion, reducing the external conversion efficiency [26]. A high small-signal conversion efficiency indicates that the power requirements for the frequency conversion process are relatively low, but does not guarantee that high absolute conversion efficiencies are attainable. Conversely, a system that can achieve near-unity photon conversion efficiency may require extreme pump powers to approach its maximum efficiency.

The small-signal conversion efficiency can be found by assuming that the frequency conversion process does not significantly affect the field intensity in the input resonant mode in addition to the pump mode, so the β terms in Eq. 1.11 and Eq. 1.12 can be neglected. In this case, a steady state solution of Eq. 1.11-1.14 can be found analytically, which yields:

$$\eta_{ss} = \frac{\eta}{P_{2,in}} = \frac{\left|s_3^-\right|^2}{\left|s_1^+\right|^2 \left|s_2^+\right|^2} = 64\,|\beta|^2 \frac{\omega_3}{\omega_1 \omega_2} \prod_{k=1}^{3} \Gamma_k (1 - \Gamma_k) Q_{k,i}. \tag{1.17}$$

The small-signal conversion efficiency unambiguously increases with β and the intrinsic quality factors $Q_{k,i}$ of each resonator mode k. For set values of Q_i, η_{ss} is maximized with critical coupling ($Q_c = Q_i$, or $\Gamma = 0.5$). If the resonator is restricted to a particular linewidth, and therefore total quality factor Q, then overcoupling is preferred to maximize η_{ss}. The upper limit of power conversion efficiency for processes that are not limited by material properties or pump depletion, η_{max} is determined by the coupling fractions and

photon energies of the input and output modes:

$$\eta_{\max} = \frac{\omega_3}{\omega_1}\Gamma_1\Gamma_3 = \frac{\omega_3}{\omega_1}\frac{Q_1 Q_2}{Q_{1,c}Q_{2,c}} = \frac{\omega_3}{\omega_1}\frac{Q_{1,i}}{Q_{1,i}+Q_{1,c}}\frac{Q_{3,i}}{Q_{3,i}+Q_{3,c}}. \tag{1.18}$$

The photon conversion η_γ can be found by scaling the power conversion efficiency by the ratio of photon energies:

$$\eta_\gamma = \frac{\omega_1}{\omega_3}\eta \leq \Gamma_1\Gamma_3 = \frac{Q_{1,i}}{Q_{1,i}+Q_{1,c}}\frac{Q_{3,i}}{Q_{3,i}+Q_{3,c}}. \tag{1.19}$$

A resonator that is critically coupled for all three modes has the highest possible small-signal conversion efficiency. However, it is limited to a photon conversion efficiency of 25%. A resonator with the same intrinsic quality factors Q_i and overcoupled input and output modes would require more pump power to reach 25% conversion efficiency, but it would have the potential to reach even higher efficiencies. The interactions between coupling, pump power, and conversion efficiency are illustrated in Fig. 1.5.

1.2 Comparison with Reported Devices

Single-photon SFG/DFG has been demonstrated in macroscopic optical cavities [1, 58] and integrated waveguides [25, 51, 19, 65]. This approach can reach high absolute conversion efficiencies but typcially requires pump powers in excess of 100 mW. Notably, single-photon difference frequency conversion from 606 nm red to the telecom C-band has been implemented in a periodically-poled lithium niobate (PPLN) waveguide with a small-signal external photon conversion efficiency of $\sim 21\%\mathrm{W}^{-1}\mathrm{cm}^{-2}$ [45].

In nanophotonic resonators, triply resonant frequency conversion processes have been demonstrated using two detuned inputs on a single resonance [73] or similar wavelength resonances of the same transverse mode [77, 26]. Triple resonant sum and difference frequency generation with an on-chip small-signal photon conversion efficiency of 1000%/W has been measured in a AlN ring resonator, which could accommodate enough pump power to reach strong coupling between the input and output wavelength modes [26]. Higher conversion efficiencies have been reported for double-resonant SHG, including a small-signal SHG power

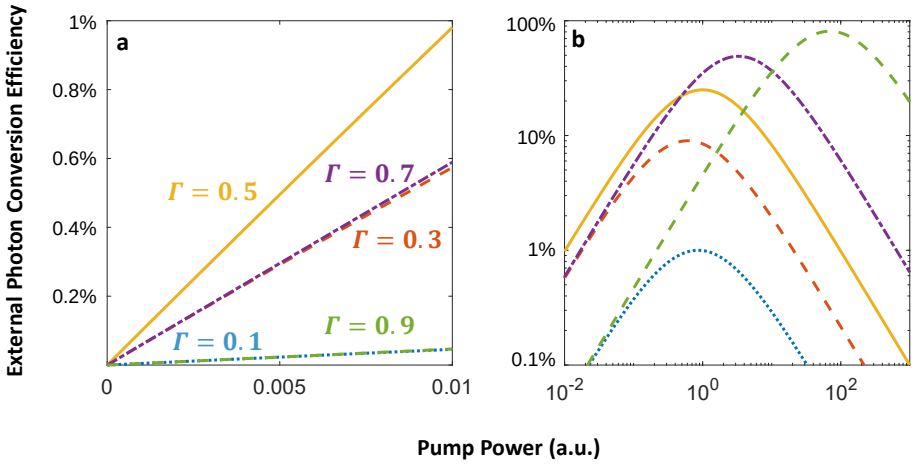

Figure 1.5: Theoretical dependence of external photon conversion efficiency on pump power for resonance-enhanced sum or difference frequency conversions with the same intrinsic quality factors Q_i but different coupling fractions: $\Gamma = 0.1$ (blue), 0.3 (orange), 0.5 (yellow), 0.7 (purple), and 0.9 (green). Each resonator has the same coupling fraction for all three of its resonant modes. The linear scale plot (a) shows the conversion efficiency increasing linearly with pump power at lower powers. The slope of the dependence, or small-signal conversion efficiency, is higher for devices that are closer to critical coupling ($\Gamma = 0.5$). The logarithmic scale plot (b) shows how conversion efficiency reaches a maximum value at some critical power and then decreases due to back conversion if pump power is increased further. Undercoupled and avercoupled exhibit similar behavior at low pump powers, but conversion efficiency in overcoupled devices continues to increase to reach higher maximum efficiencies at high pump power.

conversion efficiency of 250,000%/W in a PPLN ring resonator [43].

In the triple-resonant GaP ring resonators presented in this thesis, a small-signal photon conversion efficiency of 2100-4000%/W for sum frequency conversion from 1532 nm telecom to 647 nm visible. This is among the highest reported small-signal efficiencies for SFG or DFG, especially for frequency conversion processes involving modes at three disparate wavelengths. A small-signal conversion efficiency of 45,000%/W is projected to be attainable in GaP ring resonators, which is competitive with any currently reported material platform. While higher $\eta_s s$ may be attained in PPLN ring resonators utilizing d_{33}, these devices may struggle to reach high absolute conversion efficiencies due to the high electro-optic effect of $LiNbO_3$ as well as a reliance on high quality factors. Multi-resonant GaP photonics is a

strong contender for being the optimal platform for low-power frequency conversion in the $\sim 600 - 1000\,\mathrm{nm}$ wavelength range.

Chapter 2

EXPERIMENTAL METHODS

This chapter presents the methods used to design, fabricate, and characterize GaP nonlinear ring resonators. Simulation and design procedures are described for the multi-resonant ring resonators and coupling photonic circuits, which include waveguides, evanescent coupling regions, and grating couplers. Device fabrication includes preparation of a silicon oxide substrate and GaP membrane transfer, followed by patterning the GaP photonics layer by electron beam lithography (EBL) and etching. In the device characterization section, the instruments and microscope configurations used for device testing are described. It also includes experimental procedures for both passive (single-wavelength) and frequency conversion measurements.

2.1 Photonic Device Design

2.1.1 Material Selection

Gallium phosphide (GaP) was selected as the nonlinear material for frequency conversion and the high-index material for the photonic resonators based on its compatibility with the planned application of converting single photons from diamond NV centers to telecom wavelengths. First, GaP is a zincblende crystal with higher second-order susceptibility ($\chi^{(2)}_{ijk} = 110pm/V$ for $i \neq j \neq k$) and refractive index ($n \approx 3.31$ for $\lambda = 637\,nm$ and $n \approx 3.05$ for $\lambda = 1550\,nm$) than commonly used nonlinear materials like lithium niobate or aluminum oxide. This allows GaP structures to confine light even on a diamond substrate ($n \approx 2.4$) and potentially provide comparable frequency conversion efficiencies in lower-Q, more robust devices. Also, GaP is transparent into the visible band due to an indirect bandgap of 2.24 eV, allowing it to support low-loss modes at the diamond NV center zero-phonon emission wavelength of 637 nm (1.946 eV). A comparison of properties of nonlinear materials is shown in Table. 1.1. Based on the availability of high-quality material, the

devices were designed for GaP with a [1 0 0]-normal crystal orientation.

A silicon wafer with at least 1 µm of thermal oxide on the surface was selected as a substrate for the photonic devices. The oxide thickness was simulated to be sufficient to prevent significant interactions between the guided modes in the GaP photonic layer and the higher-index silicon substrate. While GaP was chosen in part for its compatibility with high-index substrates [23, 24], the large number of experimental devices required for the project made the readily available silicon-based substrates more practical.

The single-crystal gallium phosphide used for the photonic devices was grown to the required thickness on an aluminum-rich AlGaP substrate by molecular-beam epitaxy. Based on the available growth processes, the GaP was grown with a [1 0 0]-normal crystal orientation. The GaP layer was transferred to the SiO_2 substrate using a procedure described in Sec. 2.2.1.

2.1.2 Ring Resonators

GaP-on-oxide nonlinear ring resonators were designed for triple-resonant DFG from a 637 nm wavelength visible mode to a 1550 nm telecom mode with a 1081.4 nm pump mode, and also for double-resonant SHG from a 1550 nm fundamental to a 775 nm second harmonic mode. The primary performance metrics for a nonlinear resonator considered in this project are maximum on-chip conversion efficiency, pump power requirement, bandwidth, and footprint. Because scalability is critical for the intended application in communication networks, footprint and especially power requirements were the highest priorities for resonator design. To minimize the resonator footprint, small ring diameters were preferred. Minimizing the pump power needed to reach the maximum conversion efficiency attainable in the resonator requires a high small-signal conversion efficiency η_{ss}. From Eq. 1.17, η_{ss} depends on the coupling and quality factor of each resonant mode, as well as the nonlinear overlap β. Based on previous experiments with GaP photonics, the dominant intrinsic loss mechanism was expected to be surface scattering due to sidewall roughness from the resonator fabrication process. Sidewall scattering depends on the overlap of the resonant mode field with the etched sidewalls of the ring, which can be reduced but not eliminated by increasing the

cross-section area of the ring. Notably, because radiation does not significantly contribute to intrinsic losses, there is little reason to use larger ring diameters to reduce radiative losses. For a particular intrinsic quality factor, the small-signal conversion efficiency is maximized with critical coupling ($Q_c = Q_i$). Since the intrinsic quality factor was mostly determined by fabrication, the ring design process focused on maximizing the nonlinear overlap β, which increases with smaller mode volumes and encompasses the effects of phase matching as well as mode overlap and polarization.

The remaining performance metrics are more relevant to long-term applications than the experimental device development in this work. From Eq. 1.18, the maximum conversion efficiency η_{max} increases with overcoupled input and output modes if it is not limited by material properties. A high absolute frequency conversion efficiency is vital for most practical applications, including long-range entanglement distribution. However, to facilitate characterization of experimental devices using low-power input lasers, resonator coupling was designed to target critical coupling to maximize small-signal conversion efficiency. As the design of resonator coupling regions depends heavily on the resonator dimensions, it is addressed later in section 2.1.3. A resonator with wider mode bandwidths, as determined by the total quality factors of each resonance (Eq. 1.3), is less sensitive to minor detuning from double or triple resonance, so it is more resilient against both fabrication variations and environmental fluctuations. The bandwidth of the input and output resonances also affects how short of laser pulses or photon emitter lifetimes can be efficiently accommodated in the resonator, though this limitation is only likely to be relevant for very high-Q devices. Despite this, increasing the intrinsic quality factor of a resonator is unambiguously positive since a target bandwidth can be maintained by overcoupling.

To facilitate optimization of nonlinear ring resonator designs, the general formula for β in Eq. 1.15 was adapted for radially symmetrical structures in [1 0 0]-normal GaP. Due to the zincblende crystal symmetry of GaP, $\chi^{(2)} \neq 0$ for $i \neq j \neq k$, so nonlinear interactions require mutually perpendicular field components in each mode. Consequently, the nonlinear overlap β becomes:

$$\beta = \frac{\left|\chi^{(2)}\right|}{4\sqrt{\varepsilon_0}} \frac{\int_0^{2\pi} \left[(A_1 - iA_2)e^{i(M+2)\theta} + (A_1 + iA_2)e^{i(M-2)\theta}\right] d\theta}{\prod_i \sqrt{\int \epsilon_i |E_i|^2 \, dV}}$$

$$M = m_1 + m_2 - m_3$$

$$A_1 = \int_{NL} \left[E_{1z}(E_{2r}E_{3\theta}^* + E_{3r}^* E_{2\theta}) + E_{2z}(E_{1r}E_{3\theta}^* + E_{3r}^* E_{1\theta}) + E_{3z}^*(E_{1r}E_{2\theta} + E_{2r}E_{1\theta})\right] r \, dr dz$$

$$A_2 = \int_{NL} \left[E_{1z}(E_{2r}E_{3r}^* - E_{2\theta}E_{3\theta}^*) + E_{2z}(E_{1r}E_{3r}^* - E_{1\theta}E_{3\theta}^*) + E_{3z}^*(E_{1r}E_{2r} - E_{1\theta}E_{2\theta})\right] r \, dr dz, \tag{2.1}$$

where E_{ir}, E_{iz}, and $E_{i\theta}$ are the radial, vertical, and azimuthal field components and m_i is the azimuthal mode number of each mode. The phase matching parameter M quantifies how well the propagation constants of the three modes match, while the two cross-section overlap components A_1 and A_2 encompass the various combinations of mode field vector components that can interact through the $\chi^{(2)}$ of GaP. Note that the cross-section integrals for A_1 and A_2 are restricted to the extent of the nonlinear material (GaP) in the ring cross-section. An example of ring resonator mode fields and the resulting nonlinear overlap components is shown in Fig. 2.1.

From the perspective of a radially symmetrical structure, the effective $\chi^{(2)}$ of [1 0 0]-normal GaP changes sign for every 90° of propagation around the ring, which imposes some constraints on the design. First, every valid set of field components in A_1 and A_2 includes one vertically polarized field component ($\hat{z}$) and two in-plane field components (radial $\hat{r}$ or azimuthal $\hat{\theta}$), so one TM mode and two TE modes are required for efficient nonlinear interactions. For SHG, the fundamental mode acts as two modes, so it is restricted to TE polarization. A_1 includes the overlap terms with one radial and one azimuthal field, while the components for A_2 have either two radial or two azimuthal fields. If an angle of 0° is defined on a crystallographic direction of the GaP, then A_1 represents the mode field components with maximal nonlinear interactions at 0°, 90°, 180°, and 270° around the ring, while interactions are maximized for the A_2 field components at angles of 45°, 135°, 225°, and 315°. Second, rather than perfect phase matching with $M = 0$, a quasi-phase matching (QPM) condition $M = \pm 2$ is required for significant nonlinear

interactions in the resonator. For each QPM case, A_1 and A_2 are combined to constitute the full nonlinear overlap β, but with different relative phases. The resulting difference in interactions between radial and azimuthal field components biases the cross-section overlap integral toward the inside or outside of the ring for $M = +2$ and $M = -2$, respectively. This breaks the requirement for even mode symmetry parity that is seen for nonlinear interactions in straight waveguides. The nonlinear overlap exhibits sinc-like dependence on the phase-matching parameter M, centered at $M = \pm 2$, causing β to be severely diminished for frequency conversion processes that deviate from quasi-phase matching. The nonlinear overlap vanishes entirely for processes with integer M that do not satisfy either QPM conditions. Since all triple-resonant processes (or double-resonant SHG) necessarily have integer M, the resonator is not likely to provide significant enhancement to more than one frequency conversion process for a given set of input wavelengths.

The design parameters of the resonator were dimensions of the GaP ring (width w, radius r, and height h) and the target mode combination for QPM triple resonance. The ring height was left at the growth thickness of the GaP epitaxial layer, which was 430 nm for design generations 1 and 3 and 250 nm for generation 2. Mode selection affects intrinsic quality factor, since higher-order modes tend to be pushed toward the edges of the ring where they can interact with the rough sidewalls. Since the longer wavelengths are more difficult to confine in a given structure, the modes for the telecom (1550 nm) and pump (1081.4 nm) wavelengths were selected first. First, because vertically polarized TM modes were qualitatively observed to be more sensitive to the more constrained vertical dimension of the structure, TE polarized modes were used for telecom and pump wavelengths. The telecom mode, with the longest process wavelength at 1550 nm, was kept as the fundamental TE mode TE_{00} for all ring designs, while both TE_{00} and TE_{01} modes were used for the 1081.4 nm pump mode. The visible (637 nm) and second harmonic (775 nm) wavelengths were restricted to TM polarizations, but the specific mode selection was left flexible for design optimization along with the horizontal ring dimensions w and r.

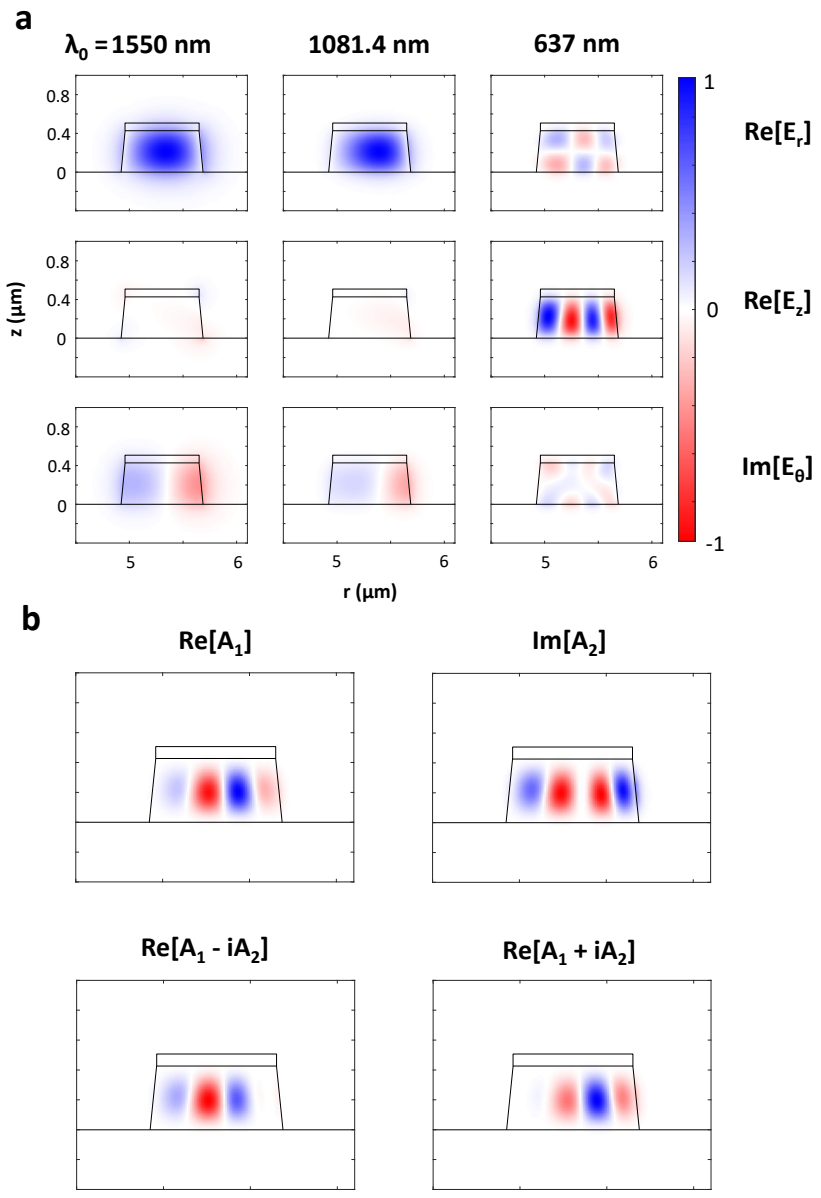

Figure 2.1: (a) Examples of radial, vertical, and azimuthal mode profiles for a $TE_{0,0}$ telecom mode, $TE_{0,0}$ pump mode, and $TM_{0,3}$ visible mode. The ring structure is outlined, with residual HSQ on the GaP ring on a flat oxide substrate. (b) Nonlinear mode overlap components A_1 and A_2 derived from the above mode fields, with their combinations for $M = +2$ (left) and $M = -2$ (right) QPM conditions.

The ring design optimization process used the Lumerical MODE bent-waveguide solver

to simulate cross-section field distributions and propagation constants for modes at the process wavelengths (637, 1081.4, and 1550 nm for DFG, or 1550 and 775 nm for SHG), which were used to calculate M, A_1, and A_2. The code used to simulate the ring resonators can be found in Appendix A.1. For the first generation devices, the simulation included only the oxide substrate and GaP ring cross-section with vertical sidewalls. In later design generations, the simulation was refined to include an 85° sidewall angle from the GaP etch as well as the HSQ resist layer that remained on the top surface of the ring after fabrication. The design search used the cross-section overlaps $|A_1 + iA_2|$ and $|A_1 - iA_2|$ from Eq. 2.1 as objective functions. These overlap values are directly proportional to β in quasi-phase matched device, but they provide a smoother design space that is more tractable to optimization algorithms than a full calculation of β. The respective QPM conditions of $M = +2$ and $M = -2$ were applied separately as requirements for valid ring designs, but these constraints were relaxed until the end of each design optimization.

For the initial exploration of the design space, the selected infrared modes were simulated at a random ring design point (r, w), and the effective indices n_{eff} required for the short-wavelength mode to satisfy each QPM condition were calculated. A set of short-wavelength modes with n_{eff} similar to these values were simulated, and $|A_1 + iA_2|$ or $|A_1 - iA_2|$ was calculated for each mode depending on the sign of M. The mode with the highest overlap was selected, and the sensitivity of M on ring dimensions was simulated for this mode to find a new design point that would be closer to satisfying a QPM condition. This hill climbing process continued until a valid design with $M \approx \pm 2$ was found; this design was recorded, and the search was restarted with a new random design point. The random design search confirmed that β increases with smaller ring diameter, until the ring is small enough that the resonant modes begin exhibiting whispering-gallery-like field distributions. With fundamental infrared modes, quasi-phase matched DFG ring designs were found for TM_{02}, TM_{03}, and TM_{04} visible modes, with the lower-order modes yielding higher values of β but requiring narrower ring widths to satisfy $M = \pm 2$. In particular, the ring designs using TM_{02} were too narrow to confine the majority of the telecom mode inside the GaP structure, so TM_{03} visible modes were used for DFG ring designs with fundamental pump modes, as well as all SHG ring designs. For similar reasons, TM_{04} visible modes were used

in conjunction with TE_{01} pump modes.

Once a mode combination and QPM condition was selected, the final design for each ring resonator was found by a more directed search. Similar to the exploratory search, an arbitrary design point (r, w) was simulated, and then ring width w was adjusted until the resonator satisfied $M = \pm 2$ for the target modes. The ring radius r was changed by a small increment to increase β, usually by decreasing the radius, and then w was adjusted to satisfy the QPM condition. This process was repeated until either a local maximum was found in the dependence of β on ring radius, or the telecom mode was no longer well confined within the GaP structure. The restriction of azimuthal mode numbers m_i to integer values for the simulated wavelengths was relaxed during the design process, including for final designs. A ring that satisfies a QPM condition with non-integer m_i is not resonant at the target wavelengths but is expected to have a set of quasi-phase matched resonances at nearby wavelengths. The final ring design was named according to its design generation and intended frequency conversion process, so design DFG2.1 would be the first ring resonator designed for difference frequency generation in the second design generation. To offset both fabrication variations and potential simulation inaccuracies, the ring width for each design was varied from its nominal value over an array of similar devices. For some early ring designs (SHG1.1, DFG1.1, and DFG2.1), a larger ring radius was used than the optimal value for maximal β in order to allow more space for the waveguide coupling regions. One of the first-generation designs, DFG1.2, used two concentric rings instead of the single ring in every other resonator design. The additional degrees of freedom from the second ring width and separation distance between the rings was intended to provide more independent control over the three resonant modes. However, due to difficulties with resonator coupling and intrinsic quality factor degradation, this approach was abandoned before a specific design optimization method could be devised.

Design	w (nm)	r (nm)	h (nm)	$\lvert\beta\rvert^2$ (J^{-1})	M
SHG1.1	843 ± 4	6740	430	3.75	+2
SHG2.1	1005 ± 10	4500	250	7.5	+2
DFG1.1	678.5 ± 6.5	6970	430	28	−2
DFG1.2	$520^* \pm 2$	4000	430	108.2	+2
DFG2.1	630 ± 10	4500	250	80.5	−2
DFG2.2	550 ± 10	3000	250	57.9	+2
DFG2.3	740 ± 20	2500	250	80.8	−2
DFG2.4	750 ± 10	3000	250	233.5	−2
DFG3.1	690 ± 15	4960	430	27.9	−2
DFG3.2	810 ± 15	3820	430	68.3	−2

Table 2.1: SHG and DFG ring resonator designs, labeled by design generation and then design variant number, with the simulated nonlinear coupling and quasi-phase matching condition for each design. Nonlinear overlap $|\beta|^2$ is calculated using second-order susceptibility $\chi^{(2)}$= 110 pm/V for GaP, and is expected to be proportional to small-signal conversion efficiency. Simulations of second and third generation devices accounted for the angled sidewall produced by the GaP etch process, resulting in lower simulated β. Designs DFG2.4 and DFG3.2 use a TE_{01} pump mode and TE_{04} visible modes. All other designs use TE_{00} and TM_{03}.
*Width includes a 75 nm gap between inner ring and 115 nm outer ring

2.1.3 Resonator Coupling

The ring resonators were evanescently coupled to on-chip waveguides to provide access to the resonant modes. To maximize small-signal conversion efficiency, the coupling regions were designed to target critical coupling for all three modes. However, due to the variability of resonator intrinsic quality factors and the sensitivity of the coupling regions to fabrication variations, critical coupling could not be implemented reliably. Most resonator designs used wrapped-waveguide coupling regions, which were designed using Lumerical MODE bent-waveguide eigenmode simulations for supermode analysis. The code used to simulate the wrapped-waveguide coupling regions can be found in Appendix A.1. For different combinations of coupling waveguide width (w_{wg}) and ring-waveguide separation distance (d), mode profiles and propagation constants were simulated for all modes in the combined ring and waveguide structure. To ensure that the coupling region could be consistently

fabricated, waveguide width was restricted to at least 40 nm, while a separation distance of at least 60 nm was reqired for 430 nm GaP membranes and 50 nm for the thinner 250 nm membranes. In the first generation of devices, two supermodes were identified as hybridizations of the ring and waveguide modes in the combined structure, and mode overlaps were calculated between each supermodes and both the ring resonator mode and the targeted waveguide mode. In later design generations, every mode in the combined structure was considered. In either case, during a single pass through the coupling region, light in the ring mode is divided between the combined-structure modes based on the mode overlaps. The relative phases of these modes evolve as the light propagates in the combined structure for some angular distance θ around the ring. The mode phases affect how much light is coupled into the waveguide mode at the end of the coupling region, and how much remains in the ring. The coupling quality factor Q_c can then be calculated based on the single-pass ring-to-waveguide coupling and the round-trip propagation time of the ring mode. Values of w_{wg}, d, and θ were selected to provide targeted values of Q_c, which were chosen in a range around experimentally observed quality factors in similar photonic devices. Larger separation distances d were preferred to minimize additional scattering losses from the coupling regions, and smaller wrap angles θ were preferred to ensure that coupling regions for all ring modes could fit in the layout. The effect of the coupling regions on the resonant wavelengths of the ring modes was expected to be small compared to structure dimension variations from fabrication processes, so it was not specifically considered during the design process.

For most device designs, separate coupling regions were designed for each ring mode. The designed dimensions of the coupling regions can be found in Appendix A.3. Due to previous observations of pump-band ring modes coupling to telecom-band output waveguides and vice versa, both infrared ring modes were coupled to a single waveguide in the third-generation triple-resonant designs. Design DFG3.1 used fundamental TE modes at both infrared wavelengths, allowing a single wrapped-waveguide coupling region to accommodate both modes. However, a wrapped waveguide design could not be found that was compatible with the dissimilar telecom and pump wavelength modes in design DFG3.2, so a straight-waveguide coupling region was used for the infrared modes for that ring design

instead. For a straight waveguide, the single-pass coupling was simulated using a Lumerical 3D FDTD simulation, and the coupling quality factor was calculated as usual.

2.1.4 Grating Coupler Circuits

The ring resonator coupling regions connect to waveguide photonic circuits leading to grating couplers, which allow the resonators to be probed from off chip by coupling light between the waveguides and free space. Diagrams of ring resonator layouts can be found in Fig. 3.1 and Fig. 4.1. Aperiodic grating couplers were designed to minimize the footprint required for the coupling circuits using the code in Appendix A.2. These grating couplers are intended to allow independent testing of large arrays of devices and would be replaced with larger, more efficient coupling methods for high-performance applications. Grating designs for each wavelength and polarization were generated using a simplified model treating the grating as series of discrete, independent scattering elements in a waveguide. Scatterer widths and spacings were optimized to maximize overlap between upward-scattered light and a target Gaussian mode shape using a sampled discrete hill climbing algorithm. The detailed coupling behavior from waveguide to free space was simulated by Lumerical 3D FDTD for each grating design candidate. Vertically-polarized (TM) waveguide modes would primarily scatter into a free-space mode polarized with the electric field parallel to the on-chip propagation axis, while TE waveguide modes would couple to free-space modes with perpendicular polarization. The grating design that provided the highest coupling into a single spot in free space over the target wavelength band was selected. If the simulated grating efficiency peak was offset from the target wavelength, all lengths in the grating design were scaled by up to $\pm 5\%$ to red- or blue-shift the efficiency curve. For grating couplers intended for multi-wavelength operation, such as for the infrared modes in the third-generation designs, two design approaches were used. First, gratings that had been designed for one wavelength were FDTD simulated at the second wavelength. If an existing design also provided reasonable performance in the second wavelength band, it would be used as a multi-wavelength coupler. Alternatively, grating designs can be co-optimized for free space coupling at both wavelengths using the hill-climbing algorithm to maximize the

product of the two single-wavelength objective functions. While this second strategy was used to generate grating design candidates for the third-generation triple-resonant devices, none of these gratings were used in the final chip layout.

Straight-waveguide grating couplers were used for the first-generation devices, with a smooth expansion region connecting the narrow waveguide to the grating, which was wide enough for a focused laser spot of the designed wavelength. However, because the grating couplers were restricted to full-thickness etches by the fabrication process, this configuration had substantial back reflection which resulted in Fabry-Perot interference in the waveguide between two grating couplers. This interference pattern was visible in the transmission spectrum of the coupling spectrum, which could obfuscate the properties of the transmission dips from coupled ring modes. To mitigate the back reflection without increasing the footprint of the coupling circuit, elliptical-profile focusing grating couplers were used for subsequent generations. The etched grates of these grating couplers were elliptical sections with one focus at the center of the waveguide and the second focus offset, so that light coming from the waveguide would not be reflected back into the waveguide. Elliptical grating designs were adapted from the previously developed aperiodic straight grating designs, with the pattern of etch widths and separations from the straight grating used for the major axis of the elliptical grating. Each edge of the linear grating was extended as an ellipse of eccentricity e, with the first edge a distance l from the waveguide to act as an expansion region. The grating coupler would include a section of the concentric ellipses of arc length ϕ, offset by an angle θ from the major axis. Design candidates with varying ellipse parameters were evaluated using 3D FDTD simulations to examine the spot shape, free-space coupling efficiency, and back reflection efficiency. More extreme eccentricities and offset angles θ tended to suppress back reflections at the cost of increasingly deformed free-space modes, which would be difficult to match with a focused laser spot. Increasing the expansion length l and arc length ϕ could also reduce back reflection, but increasing the grating area much beyond the laser spot size could result in the coupling efficiency varying with spot position. Final designs were selected to reflect less than 1% of power within the target wavelength range with as little performance alteration as possible. Most final elliptical grating designs provided similar simulation coupling efficiencies as their straight-waveguide counterparts.

The layout of the coupling circuit was designed with all of the grating couplers clustered together, allowing simultaneous excitation or measurement of every grating coupler from a single microscope objective lens. Perpendicular orientation was used for each pair of grating couplers for the same wavelength to ensure polarization contrast between coupled output light and scattered input light. The waveguide widths and Bezier bend radii for each wavelength were designed to provide minimal losses for fundamental waveguide modes with polarization (TE or TM) matching the ring resonator mode. If the low-loss waveguide also supported a higher-order mode of the same polarization, a narrower waveguide section was added to the coupling circuit as a mode filter to attenuate the higher-order mode. Chip pattern layouts were generated using the KLayout python scripts found in Appendix A.3, along with the dimensions used for grating couplers and waveguide circuits on each chip.

2.2 Fabrication

This section presents the general fabrication methods used to produce the nonlinear ring resonators. The details of fabrication for the first and third generation chips can be found in Appendix B.

2.2.1 GaP Membrane Transfer

The fabrication process started with an epiwafer consisting of [1 0 0]-normal GaP grown by gas-source molecular-beam epitaxy (MBE) on an Al-rich AlGaP sacrificial layer on a GaP wafer. A 430 nm GaP membrane on 300 nm of $Al_{0.8}Ga_{0.2}P$ was used for generations 1 and 3, and 250 nm of GaP on 300 nm of $Al_{0.88}Ga_{0.12}P$ for generation 2. All fabrication processes except for the epiwafer growth were performed in the Washington Nanofabrication Facility (WNF) at the University of Washington.

To make a GaP-on-oxide chip for the designed devices, the MBE GaP layer must be transferred to a SiO_2 substrate. First, a releasable GaP membrane was defined using photolithography. The generation 1 chip used a 3 mm square membrane pattern with etch vias defined every 250 µm. The membrane size was reduced to 2.5 mm with a 500 µm etch via spacing for generations 2 and 3. A chip large enough for 4-5 membrane patterns was cleaved

from the epiwafer, and the GaP surface was cleaned by sonicating in acetone for 4 min followed by soaking in isopropyl alcohol (IPA) for 5 minutes. The chip was blown dry with N_2 and baked for 5 min at 150 °C to remove residual moisture. A positive photoresist (AZ1512) was spun on to a thickness of $\sim 1\,\mu m$, using a 2 s ramp to an initial plateau of 500 RPM for 5 s, followed by a 3 s ramp to 5500 RPM for 40 s. The resist was baked at 110°C for 1 minute and then exposed with the membrane pattern for 4 s using a mercury i-line arc lamp and a contact mask in an ABM contact aligner. The resist was developed for 60 s in a 1:4 AZ340:H_2O solution, rinsed in deionized (DI) water, and dried. At this point, the epiwafer chip was cleaved to separate each membrane pattern. The GaP membrane patterns were etched with a Cl/N_2 (1.0/7.5 sccm) inductively-coupled plasma reactive ion etch (ICP-RIE) in an Oxford Instruments PlasmaLab 100 ICP 180 chlorine etcher, using the AlGaP as an etch stop. The plasma etch used an ICP power of 100 W, and the radiofrequency (RF) power was adjusted to approximately 40-50 W to target a DC bias voltage of 240 V during a 15-20 min etch chamber conditioning process using the etch recipe on a blank silicon dummy wafer. To avoid excessive sample heating, the plasma etch was divided into multiple stages, with each consisting of a 5 s step with a chamber pressure of 5 mTorr to facilitate plasma striking, followed by a 30 s etch at 4 mTorr. The GaP membrane of either thickness was fully etched with two or three repetitions of this etch, which was confirmed using a profilometer.

Prior to membrane transfer, a silicon substrate chip with 1 µm (generations 1 and 3) or 10 µm (generation 2) surface layer of wet thermal oxide was prepared. The oxide surface was cleaned with acetone, IPA, and O_2 plasma (150W for 5 min in an AutoGlow barrel asher) and treated with HMDS to promote membrane adhesion. The GaP membrane was released from the growth substrate by etching the AlGaP layer in a dilute 1.5 solution of hydrofluoric acid (HF) in DI water (2% for generation 2) for two to five hours. When the AlGaP was sufficiently etched to allow partial release of the GaP membrane, the GaP surface would become visibly uneven and exhibit a golden sheen instead of the transparent orange of solid GaP. At this point, the membrane chip could be lifted to near the surface of the HF solution and jerked with small, sharp movements to dislodge the membrane. This step prevented the GaP membrane from adhering to the underlying substrate, but could also cause the membrane to break into multiple fragments. To remove any residual HF,

the membrane was transferred via water droplets to two consecutive containers of fresh DI water using a perforated Teflon scoop, with the membrane suspended in the fluid or, ideally, floating on the fluid surface to avoid contact with the scoop. If the membrane sank to the bottom of the solution, gentle agitation of the fluid could raise the membrane far enough to capture with the scoop. Once the membrane was floating on or in clean DI water, it was captured on the oxide substrate and removed from the water. Once the water droplet had dried enough for the membrane to make definite contact with the oxide surface, it was blown dry using nitrogen gas and then further dehydrated using a microscope illumination lamp during optical inspection. Any remaining fluids were removed by baking overnight on a hot plate at 80°C.

To ensure consistent behavior, the membrane etch was performed within two weeks of the photolithography process and the transfer within a week afterward, with the membrane stored in the cleanroom in a dry nitrogen atmosphere. After the transfer, the GaP-on-oxide chip could be stored for up to a year, with the photoresist left on the membrane as a protective coating. Immediately prior to additional fabrication processes, the photoresist was stripped in an EKC solvent bath for 20 minutes at 80°C. The chip was then rinsed with acetone and IPA, blown dry, and dehydrated on a 80°C hot plate overnight.

2.2.2 Photonic Circuit Patterning

With the GaP-on-oxide chip prepared, the photonics chip pattern was transferred to the GaP membrane using electon beam lithography (EBL) with HSQ as a high-resolution, negative resist. First, a $\sim 5\,\mathrm{nm}$ layer of SiO_2 was deposited on the GaP membrane to improve resist adhesion. For generation 1 chips, the oxide was deposited by electron beam evaporation in a CHA SEC-600, while generations 2 and 3 used plasma-enhanced CVD in a SPTS SPM system. If more than a day had passed since the oxide deposition, the chip surface was cleaned using acetone, IPA, and O_2 plasma. A 6% solution of HSQ in MIBK (DOW Corning XR-1541-006) that had been decanted from refrigerated storage and kept at room temperature for at least one day and no more than two weeks was used as a resist. Following a 5 min prebake at 150°C, the HSQ was spun on the chip to a thickness

of $\sim 100\,\mathrm{nm}$ using a 1 s ramp to a 500 RPM plateau for 1 s, followed by a 1 s ramp to 6000 RPM for 45 s. The resist was baked at 80°C for 4 min and then exposed immediately. The chip pattern was written in the resist using a JEOL JBX-6300FS EBL system. An exposure dose of 2000-2500 $\mu C/cm^2$ was delivered with a 500 pA, 100 kV electron beam, with 1 nm shot pitch and proximity effect correction based on a numerically simulated point spread function. The exact dose was determined by a dose test performed with HSQ resist from the same container, spun onto an oxide substrate with no GaP membrane using the same recipe. Within 24 hours of spin-on, the HSQ was developed in a 25% TMAH solution for 4 minutes with light manual agitation, gently rinsed with DI water, and dried with nitrogen. Finally, the pattern was transferred to the GaP membrane by $Cl/N_2/Ar$ (1.0/3.0/6.0 sccm) ICP-RIE using 4 mTorr chamber pressure and 60 W ICP excitation, in the same machine used for the membrane etch. Following a 10 min chlorine-based chamber self-clean, the RF power of the etch recipe was adjusted to target a DC bias voltage of 240 V during a 15 min chamber conditioning process performed on a silicon dummy wafer. To avoid overetching the GaP sidewalls due to overheating, the etch was performed in multiple segments consisting of a 5 s plasma strike step at 5 mTorr followed by a 15 s etch at 4 mTorr. These etch segments were repeated until the exposed GaP membrane appeared to be completely etched based on optical examination while the chip was in the etcher loading chamber. The chip was further examined by optical microscope and SEM to confirm that the membrane had etched completely. If additional etching was required after the chip was removed from vacuum, the 15 min chamber conditioning was repeated with a silicon wafer before continuing the membrane etch. The GaP etch typically produced $\sim 85°$ sidewall angles, with sidewall roughness apparently dominated by roughness from the exposed resist. The third-generation devices and other GaP structures fabricated in a similar time period exhibited sidewalls that were closer to vertical, which is possibly related to the addition of a chamber wall heater to the ICP-RIE etcher. Because the exposed HSQ could not be selectively stripped without affecting the SiO_2 substrate, it was left on the devices as a partial surface cladding.

2.3 Device Characterization

2.3.1 Experimental Setup

The nonlinear photonic resonators were tested using various configurations of a custom-built microscope on optical breadboard, using fiber-coupled laser inputs at each wavelength range. Diagrams of the experimental setups can be found in Fig. 3.1 and Fig. 4.1, and photographs of the DFG/SFG testing setup are shown in Fig. 2.2. For testing the SHG and DFG devices in the first two design generations, a Santec TSL-510-C tunable laser was used for telecom-band (1500-1565 nm) excitation, with a filtered WhiteLase-Micro supercontinuum laser (SCL) for the second harmonic (750-800 nm) and visible (630-650 nm) wavelength bands. Only preliminary passive transmission measurements were performed on the resonators designed for DFG in these generations, so no pump-band (1070-1130 nm) light source was required or implemented in the setup. Tunable lasers in all three wavelength bands were used to test the third-generation triple-resonant devices: telecom (Agilent HP 81680A, 1470-1580 nm), pump (Newport Velocity 6700, 1070-1130 nm), and visible (Newport Velocity 6300, 633-640 nm). Additionally, a WhiteLase-Micro SCL with varying filter configurations provided broadband excitation across the entire wavelength span. Up to two inputs at different wavelength bands were combined into a single path using a dichroic mirror. Different laser options for each band were selected with flip-mounted mirrors. The excitation path was aligned through a linear polarizer and into a Nikon Plan Fluor 40x microscope objective lens to be focused on the photonic device chip. An achromatic half-wave plate (Thorlabs SAHWP05M-1700) directly above the objective lens adjusted the excitation polarization with respect to the chip.

The device chip was placed on an XY translation stage that was used to navigate to devices on chip and optimize the position of the excitation laser spot on the input grating coupler. Microscope focus was controlled by vertically translating the objective lens. During the first two design generations, manual micrometer actuators were used for both stage position and objective focus. An XYZ piezo actuated stage was added to allow finer position optimization while measuring the third-generation devices. Chip temperature was controlled by a resistive heater on the stage, with a thermoelectric cooler (TEC) added during the third

generation to access temperatures below room temperature.

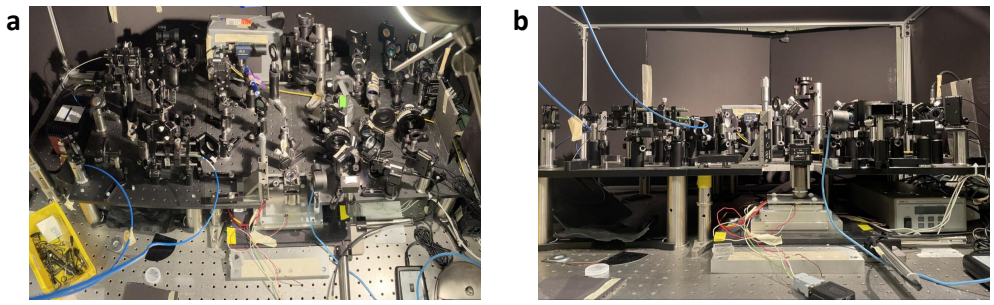

Figure 2.2: (a) Top and (b) side view of the optical setup used for passive and frequency conversion testing of third-generation DFG devices.

Light collected from the chip was split from the excitation path with a broadband 50/50 beam splitter (Thorlabs BSW29). The collection path passed through a confocal lens pair with a removable pinhole at the shared focal plane as a spatial filter to removed light scattered from sources other than a target output grating coupler. The portion of the image that passes through the pinhole was adjusted using the mirrors directly before the confocal path. Control of these mirrors was changed from manual micrometers to Newport Agilis piezo-actuated mounts during the third design generation. For the first two design generations, a single confocal path was shared by all wavelength bands. In the third generation, the visible and telecom wavelength bands were split between two separate confocal paths with a flip-mount mirror. The 1080 nm pump band was compatible with both paths. Scattered input light was further suppressed by a linear polarizer set to be orthogonal to the input polarizer, since the photonic coupling circuits were designed to have cross-polarized inputs and outputs. Photodetector and dielectric mirror efficiency spectra are different enough for the wavelength bands used for the SHG devices to inherently avoid cross-contamination in measurements. For sum or difference frequency, additional wavelength filters were required to separate the pump wavelength from the output wavelength.

After the confocal path, the collected light was directed to different measurement devices using flip-mount mirrors. Wide-field images were monitored using CCD cameras (Si for visible to pump bands, InGaAs or fluorescent-coated Si for pump to telecom band) to

allow on-chip navigation and coarse positional optimization for measurements. Amplified Si (visible to pump) and InGaAs (telecom) photodiodes were used for power measurements with narrow-band inputs, while a grating spectrometer with a Si CCD camera was used for wavelength-resolved measurements. A fiber-coupled Si avalanche photodiode single-photon counting module (SPCM) was added for high-sensitivity power measurements while testing the third-generation devices. Neutral density attenuators up to OD7 could be added to the collection path to avoid detector saturation without altering the input powers.

For high-power measurements, an erbium-doped fiber amplifier (EDFA) was used to boost the power of the telecom laser before coupling onto the optical table. In order to avoid excessive resonator heating from the increased input power, the telecom input path could be configured for pulsed operation. For the first two device generations, the telecom tunable laser was amplified using an Amonics AEDFA-30-B (1 W maximum output power), and a free-space GaP acousto-optic modulator (AOM) was added to the telecom-band input path to periodically redirect the laser to a blocker so that the device was only excited in short pulses. For the third generation, a fiber-coupled lithium niobate electro-optic modulator (EOM) was used to interrupt the telecom laser before the EDFA (Thorlabs EDFA-100P, 100 mW output). This configuration was easier to insert and remove from the measurement setup, but because the residual transmission through the EOM was amplified by the EDFA, time-resolved measurements with the SPCM and a timing board were required to accurately measure device behavior only during the pulse.

The visible-band tunable laser and the EDFA used for SHG measurements exhibited significantly time- and wavelength-dependent output power in the targeted polarization, so these inputs had to be actively monitored during measurements to ensure data accuracy. For the EDFA, an InGaAs photodiode was added to the unused port of the beam splitter separating the excitation and collection microscope paths. For the visible laser, a 10% beam sampler leading to a Si photodiode was added to the visible-band input path and removed when using other input lasers. Additionally, a wavemeter was used to monitor the output wavelength of the pump-band tunable laser during fine wavelength scans.

2.3.2 Measurement Methods

The nonlinear ring resonators were first characterized using passive transmission measurements at single wavelengths. The exciting laser spot was optimized on the input grating coupler to maximize power transmitted to the output grating. The initial rough optimization was performed qualitatively based on the intensity of the transmitted spot on the wavelength-compatible camera. The collection path alignment was then adjusted so that the pinhole was centered on output grating to allow a fine position optimization using quantitative power measurements. For narrow-band tunable laser inputs, the transmitted power was measured with a photodiode or SPCM while sweeping the input wavelength over a set range. Fast continuous wavelength sweeps were used to identify resonant wavelengths for each ring, while slower sweeps or, for the telecom lasers, discrete wavelength steps allowed higher resolution, more accurate measurements used for detailed characterization of resonance properties. The spectrometer was used to measure broadband transmission from SCL excitation. The transmission efficiency spectrum for each device and wavelength band was calculated from the measured power normalized by the input power spectrum, which was derived from measurements of the excitation laser spot reflected from the Si/SiO_2 substrate surface. Grating coupler efficiency was calculated as the square root of the total efficiency, and coupled ring resonances were identified by narrow dips in transmission. The linewidth and residual transmission of the resonant dips were extracted from least-squares Lorentzian curve fits and used to calculate resonance quality factor Q and estimate the intrinsic and coupling components Q_i and Q_c. The curve fits used a linear background term to approximate the varying grating coupler efficiency, and a second Lorenztian was simultaneously fitted for split resonances. In unusual cases where a narrow-band resonance overlapped the wavelength range of a much lower-Q resonance, the narrow resonance was fitted with a Fano curve rather than Lorentzian.

Frequency conversion performance was measured using similar methods, with one or more laser inputs optimized into input grating couplers while output power was measured in a different wavelength band. SHG measurements only require a single laser input, so they used the same input coupling optimization procedure as single-wavelength transmission

measurements. In cases where the converted light was strong enough to allow real-time measurements instead of requiring long integration times, the laser position was further adjusted to maximize the converted light intensity while the input wavelength was tuned to a resonance. For sum- and difference- frequency conversion processes requiring two input lasers, one laser was optimized to couple into the grating using stage position, and then the second laser was moved onto its input grating by adjusting the alignment of its input path. In either case, when the input wavelength(s) were significantly detuned from any ring resonance, the converted light was extremely weak or undetectable. Tuning each input wavelength onto a ring resonance usually produced a clear peak in converted output power with greatly enhanced intensity if the converted wavelength coincided with its own quasi-phase matched resonance.

Due to variations in the device fabrication process, few as-fabricated resonators were likely to satisfy the double- or triple-resonant condition under ambient conditions, so temperature control was used to correct small detunings on the order of a few resonant linewidths. Increasing the temperature of the ring resonator increases the refractive index of GaP, red-shifting all resonances at different rates and changing their relative detuning. The conversion efficiency is sensitive to the precise detuning only when the wavelength of the converted light is close enough to the resonance to have significant resonant enhancement, so near-QPM processes produce a converted output that is both particularly intense and highly sensitive to temperature. These characteristics were used to identify candidate devices for detailed testing out of the hundreds fabricated on each chip. While near-QPM devices could be identified by comparing the resonant wavelengths of coupled ring modes found with passive transmission measurements, this approach was complicated in practice by the requirement of synchronizing the absolute wavelength calibrations of the different detectors and tunable lasers required for the disparate process wavelengths. In addition, the transmission spectrum of the grating couplers, multi-mode nature of the ring resonators, and often non-ideal resonator coupling can all hinder accurate mode identification or obscure some ring modes entirely. Using direct observations of conversion efficiency and temperature sensitivity allowed the resonators to be screened quickly with measurements that did not need to be tailored to each individual device. Initial frequency conversion measurements were used first

to search for near-QPM devices and then determine their optimal operating temperatures. Similar to the passive transmission measurements, the frequency conversion measurements for these device surveys were mostly focused on relative output intensities, either compared to other resonators or the same resonator at different temperatures. In contrast, measuring the small-signal or maximum absolute conversion efficiency of a resonator depends on the precise input and output powers. For these measurements, the off-chip input power was recorded during or immediately before each data point was measured. The on-chip powers used to calculate the waveguide-to-waveguide conversion efficiency were derived using calibration measurements of the efficiencies of the grating couplers, detectors, and each optical component of the test setup.

Chapter 3

SECOND HARMONIC GENERATION

This chapter presents device designs and measurement results for second harmonic generation (SHG) from $\sim 1550\,\text{nm}$ to $\sim 775\,\text{nm}$ in double-resonant ring resonators. Two generations of SHG ring resonators were designed and fabricated. Double-resonant SHG was observed in some devices from both generations, with a maximum small-signal conversion efficiency of 400%/W in a first-generation ring.

In this chapter, we study SHG in a gallium phosphide (GaP) on oxide platform that that further improves on previous studies and illustrates the potential of this material platform for achieving high-efficiency frequency conversion in robust, compact, and wide bandwidth integrated cavities. In particular, GaP-on-oxide ring resonators were designed for quasi-phase-matched SHG from the telecommunication C band (1550 nm) to the near-infrared (775 nm). This work represents at least an order-of-magnitude improvement over prior SHG GaP devices [46, 35, 54] while also extending device functionality and applicability via coupling to on-chip waveguides. Waveguide-to-waveguide SHG efficiencies of up to 400% W^{-1} are observed in 14 µm diameter rings. The conversion efficiency is primarily limited by overcoupling to both input and output waveguides.

In addition to its significant $\chi^{(2)}$ second-order nonlinear susceptibility (∼100 pm/V [18]), gallium phosphide offers a unique combination of properties useful for frequency conversion applications. GaP has a high index of refraction (n = 3.31 at 637 nm [12]) compared to AlN (n = 2.2 [50]) or most traditional nonlinear materials like $LiNbO_3$ (n = 2.28 [79]), allowing fabrication of ultra-low mode volume resonators on a wide variety of substrates, including diamond (n = 2.4) [5, 61, 21, 54]. With a wide bandgap E_G of 2.32 eV, GaP maintains transparency into the visible spectrum, permitting efficient frequency conversion of a wider range of wavelengths than other high-index materials such as GaAs (E_g=1.42 eV, $\chi^{(2)} \sim$ 220 pm/V [63]). Notably, the emission wavelength of the diamond nitrogen-vacancy center,

a solid-state qubit candidate, falls within the transparency window of gallium phosphide [21].

Due to its degenerate long-wavelength mode, SHG is not compatible with the intended application of frequency conversion of single photons from diamond color centers. However, this degenerate mode allows the frequency conversion performance of SHG devices to be tested using a single telecom-band laser input, with a near-visible output wavelength that can be easily measured on a silicon photodetector. Both of these instruments are widely available, and the widely separated input and output wavelengths simplify both resonator coupling and measurement setup alignment compared to DFG or SFG with three wavelengths. For this project, SHG ring resonators are used as a relatively reliable platform to develop and empirically test methods for both design and measurement of multi-resonant frequency conversion devices, which were then applied to the more technically demanding problem of triple-resonant rings.

3.1 Generation 1 [1]

The first SHG resonator design was a single ring resonator in 427 nm thick GaP with a radius of 6.74 µm, measured to the inner edge of the ring. A 50-device array was fabricated, varying the nominal ring waveguide width from 839 nm to 847 nm to ensure quasi-phase matching and doubly resonant enhancement could be attained even with fabrication variations.

3.1.1 Model and design

At low input powers, the effect of down conversion on the efficiency and power requirements for achieving SHG in a doubly resonant cavity is negligible [55]. In this undepleted regime, the conversion efficiency corresponding to a cavity supporting modes at angular frequencies $\omega_{1,2}$ and coupled to waveguides, is given by [55, 9]:

$$\frac{P_{2,out}}{P_{1,in}^2} = \frac{|\chi^{(2)}|^2}{\epsilon_0 \lambda_1^3} |\bar{\beta}|^2 \frac{2}{\omega_1} \frac{Q_1^4 Q_2^2}{Q_{c1}^2 Q_{c2}} = \frac{|\chi^{(2)}|^2}{\epsilon_0 \lambda_1^3} |\bar{\beta}|^2 \frac{2}{\omega_1} Q_{i1}^2 Q_{i2} \frac{Q_{i1}^2 Q_{c1}^2}{(Q_{c1}+Q_{i1})^4} \frac{Q_{i2} Q_{c2}}{(Q_{c2}+Q_{i2})^2}. \quad (3.1)$$

Here, Q_k, Q_{ik}, and Q_{ck} denote the loaded, intrinsic, and coupling quality factors of mode $k = \{1, 2\}$, with $1/Q_k = 1/Q_{ik} + 1/Q_{ck}$. Mode 1 is the fundamental and mode 2 is the second

[1] Material in this section is reproduced from Ref. [41].

harmonic. The coefficient $\bar{\beta}$ is the dimensionless nonlinear overlap of the fundamental and second harmonic modes,

$$\bar{\beta} = \frac{\int_{\mathrm{NL}} \sum_{i\neq j\neq k}(E_{1i}E_{2j}^{*}E_{1k} + E_{1i}E_{1j}E_{2k}^{*})d\boldsymbol{r}}{\left(\int \epsilon_1 |E_1|^2 d\boldsymbol{r}\right)\sqrt{\int \epsilon_2 |E_2|^2 d\boldsymbol{r}}}\sqrt{\lambda_1^3}, \tag{3.2}$$

a generalization of the familiar phase matching figure of merit [13]. For zincblende crystals such as GaP, $\chi^{(2)}$ is nonzero only for mutually perpendicular field components [13]. Note that the integral in the numerator is only evaluated over the extent of the nonlinear medium. Notably, achieving high conversion efficiencies requires large $\chi^{(2)}$, high intrinsic quality factors, critical coupling at both the fundamental and second-harmonic modes, and high nonlinear overlap $\bar{\beta}$. Previous work with GaP photonics on diamond [23] has indicated that the intrinsic quality factor is determined by process-dependent sidewall roughness, so the device design process was focused on achieving high mode overlap and coupling rather than increasing Q.

A ring resonator topology was chosen to allow control over mode properties and independent coupling to on-chip waveguides with minimal design variables. To ensure sufficient confinement at 1550 nm, a 427 nm thick photonics layer of (100) GaP on a thermal SiO_2 substrate was used. The ring structure imposes rotational symmetry on resonator modes. However, in (100) GaP, the effective nonlinear susceptibility changes sign every 90°, so quasi-phase-matching is required to avoid back-conversion [20]. Also, because only mutually perpendicular field components contribute to $\bar{\beta}$ in GaP, the fundamental mode must be transverse-electric (TE) and the second harmonic mode must be transverse-magnetic (TM). To allow straightforward device optimization under these constraints, Eq. (3.2) was translated to cylindrical coordinates:

$$\bar{\beta} = \sqrt{\lambda_1^3}\int_0^{2\pi} \beta^{+}e^{i(2m_1-m_2+2)\theta} + \beta^{-}e^{i(2m_1-m_2-2)\theta}d\theta \tag{3.3}$$

$$\beta^{\pm} = \frac{1}{(\int \epsilon_1|E_1|^2\ r\ drdz)\sqrt{\int \epsilon_2|E_2|^2\ r\ drdz}}\int_{NL}\big(2[E_{1r}E_{1z}(E_{2r}^{*}+E_{2\theta}^{*}) + E_{1\theta}(E_{1r}E_{2z}^{*}+E_{1z}E_{2r}^{*})]$$

$$\pm i[(E_{1r}^2 - E_{1\theta}^2)E_{2z}^{*} + E_{1z}(E_{1r}E_{2r}^{*} - E_{1\theta}E_{2\theta}^{*})]\big)\ r\ drdz$$

where m_k is the azimuthal mode number of mode k. In this coordinate system, it can be seen that $\bar{\beta}$ is maximized when the quasi-phase-matching condition $2m_1 = m_2 \pm 2$ is satisfied, with contributions from $\beta^{\pm}$ scaled by $\mathrm{sinc}(\pi[2m_1 - m_2 \pm 2])$ for off-resonant or single-resonant conversion. For the mode polarizations required for SHG, both β^+ and β^- depend primarily on the in-plane field components of the fundamental (E_{1r} and $E_{1\theta}$) and the vertical component of the second harmonic mode (E_{2z}). Terms that depend on the vertical component of the fundamental mode are expected to have a negligible effect on conversion efficiency.

The resonator design process was based on two-dimensional eigenmode simulations of a ring cross-section performed using Lumerical MODE Solutions software. First, the fundamental TE_{00} at $\lambda_1 = 1550$ nm was simulated for a ring of radius on the order of ten microns. Higher-order TM modes with similar effective index were simulated for $\lambda_2 = 775$ nm, and the mode with the highest $|\beta^{+/-}|$ was selected. The ring width and radius was then modified via a gradient algorithm to minimize the phase-mismatch parameter $(|2m_1 - m_2| - 2)$ for the selected modes. Through this process, high-efficiency resonator design candidates could be found with minimal computational resources and without bias toward higher-order harmonic modes. A final ring design of width $w = 840$ nm and radius $r = 7.14$ µm (measured from the center of the waveguide) was found, corresponding to an antisymmetric TM_{03} second harmonic mode shown in Fig. 3.2 (inset), which yields $2m_1 - m_2 = +2$ and $\bar{\beta} = 1.43 \times 10^{-4}$.

To allow testing of large device arrays on a single chip, the ring resonator was evanescently coupled to waveguides terminating in nearby grating couplers, as shown in Fig. 3.1(a). Critical coupling of both modes is vital for maximizing conversion efficiency, so independent wraparound coupling regions were designed for each ring mode via supermode analysis. Shared coupling regions, such as tapered fibers, often result in reduced performance due to at least one severely undercoupled or overcoupled mode [35, 27]. Waveguide widths, ring-to-waveguide separations, and coupling region lengths were co-optimized to theoretically provide coupling quality factors of $Q_{1c} \approx 2 \times 10^5$ for the 1550 nm mode and $Q_{2c} \approx 2 \times 10^4$ for the 775 nm mode.

3.1.2 Fabrication and testing

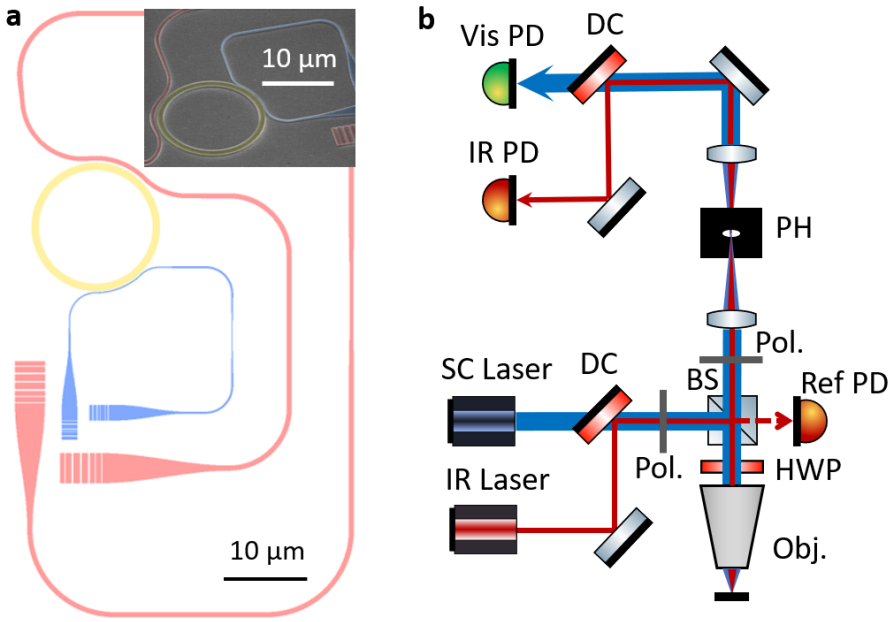

Figure 3.1: (a) On-chip layout of the nonlinear ring resonator (yellow) coupled to two independent input/output waveguides for 775 nm (blue) and 1550 nm (pink) light. The proximity of the grating couplers allow any combination of inputs and outputs to be focused or collected simultaneously by a single microscope objective. *Inset:* SEM image of a fabricated GaP SHG device. (b) Free-space measurement setup for the device. Cross-polarization and the pinhole (PH) are used to eliminate reflected input light. PD: photodiode, Obj: objective, BS: beamsplitter, DC: dichroic mirror, HWP: half-wave plate.

A 427 nm-thick GaP layer on a 300 nm $Al_{0.8}Ga_{0.2}P$ sacrificial layer was grown by molecular beam epitaxy on a GaP substrate. A $(2.5\ \text{mm})^2$ area GaP membrane was released from the substrate and transferred to a 10 µm thermal SiO_2-on-Si substrate. Before transfer, the oxide surface was cleaned and treated with hexamethyldisilazane vapor. The GaP membrane was released from the sacrificial AlGaP layer in 3:100 HF:H_2O and transferred to DI water. The membrane was then captured on a water droplet on the oxide substrate. A drying step at 80 °C completed the membrane transfer. The described transfer process was used due to its compatibility with transfer to mm-scale diamond chips for quantum information applications [68, 24, 60]. Recently, wafer-scale GaP membrane transfer to silicon

oxide has been realized by other groups via direct wafer bonding followed by substrate removal [61, 75]. The ability to fabricate devices after transferring from the growth substrate is vital to realizing the potential flexibility and portability of GaP nonlinear photonics.

In our devices, the resulting GaP-on-oxide chip was patterned with electron beam lithography, using ∼100-nm-thick HSQ as a resist. A final $Cl/Ar/N_2$ (1.0/6.0/3.0 sccm) reactive ion etch step was used to transfer the mask into the GaP-on-oxide substrate [23]. A device schematic and SEM image are shown in Fig. 3.1(a). Two grating-coupled input/output waveguides, one for the fundamental and one for the second harmonic, are used to couple to the device. A 50-device array was fabricated varying the ring waveguide width from 839 nm to 847 nm to ensure quasi-phase matching and doubly resonant enhancement can be attained even in the presence of fabrication tolerances. The measured ring waveguide widths of the two devices (SHG01, SHG02) exhibiting doubly resonantly enhanced SHG are listed in Table 1.

Table 3.1: SHG device characteristics. w is the resonantor waveguide width. T is the transmission on-resonance. Uncertainty in w denotes the range of measured values. Q and T are determined by a Lorentzian fit with uncertainty representing the 95% confidence interval.

Device	w	Q_1	Q_2	T_1	T_2
SHG01	847 ± 23 nm	$26,500 \pm 1500$	$13,600 \pm 5400$	0.44 ± 0.10	0.50 ± 0.05
SHG02	847 ± 17 nm	$40,700 \pm 10700$	$16,800 \pm 3200$	0.81 ± 0.05	0.52 ± 0.02

The devices were tested using the setup shown in Fig. 3.1(b). A scanning 1550 nm laser (Santec TSL-510) was used to excite the fundamental mode. Figure 3.2(a) shows the telecom transmission measurement curve for SHG01. The Lorentzian fit to the the resonance dip corresponds to $Q_1 = 2.65 \times 10^4$, with Q_1 denoting the total quality factor, $1/Q_1 = 1/Q_{c1} + 1/Q_{i1}$. The transmission coefficient on resonance is $T_1 = 0.44$

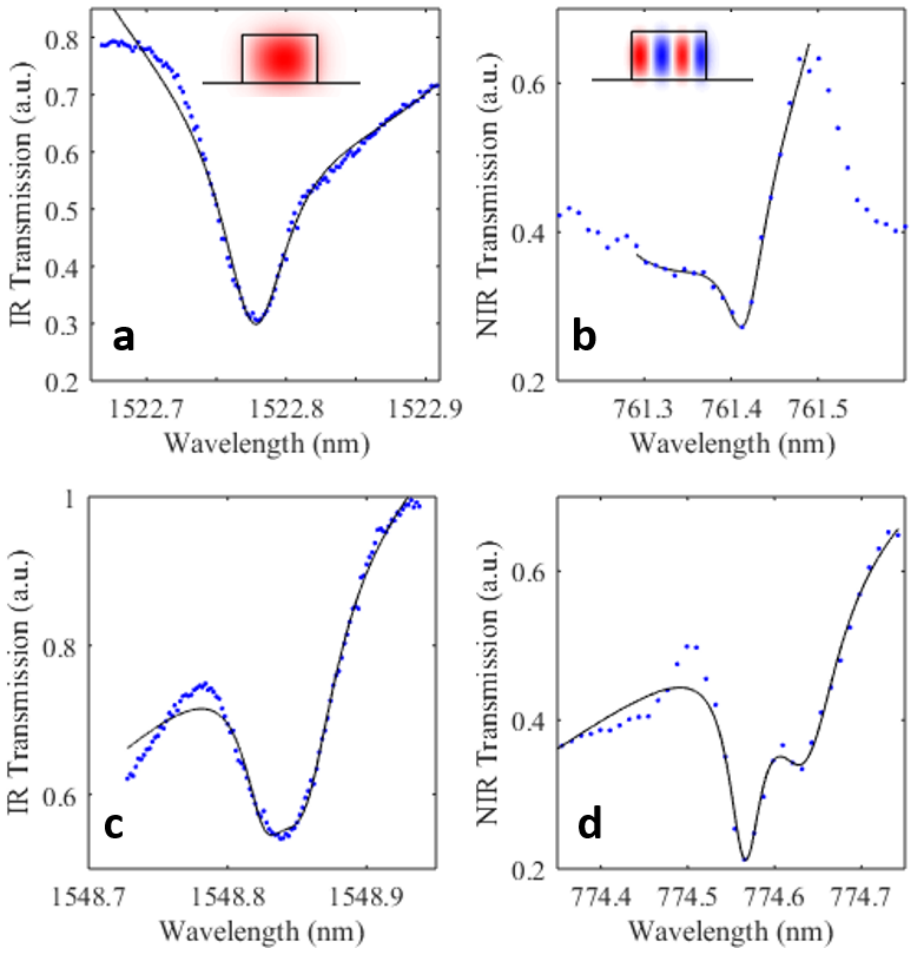

Figure 3.2: The transmission dip from telecom TE_{00} (a,c) and near-infrared TM_{03} (b,d) resonances in devices SHG01 (a,b) and SHG02 (c,d), along with fitted Lorentzian curves. Background is approximated with linear or quadratic functions. A cross-section of the mode profile is inset. The telecom resonance was measured on an infrared power meter with a tunable laser input, and the near-infrared resonance was measured using a supercontinuum laser and spectrometer.

Transmission spectra of a broadband 775 nm source (supercontinuum laser or LED), shown in Fig. 3.2(b), were used to determine the second-harmonic mode quality factor Q_2 and transmission T_2. Quality factors and transmission coefficients for both modes and both devices are given in Table 3.1. Additionally, a cross-sectional mode profile for both modes are included as insets in Figs. 3.2(a) and 3.2(b).

Single wavelength transmission measurements at 1550 nm (775 nm) were used to measure the grating coupler efficiency as well as bulk transmission through the microscope set-up at each wavelength. A description of the grating coupler and microscope loss characteristics can be found in Section 3.1.4. The telecom (SHG) grating couplers were designed for 33% (24%) efficiency at 1550 nm (775 nm). The measured efficiencies at the experimental resonances were 22% at 1523 nm (3.2% at 761 nm) in SHG01 and 19% at 1549 nm (7.5% at 774 nm) in SHG02. All measured values are derived by assuming identical efficiencies for the input and output gratings.

For SHG measurements, the telecom input grating is used to excite the fundamental mode. Input power is continually monitored by a reference photodiode. Simultaneously, the SHG signal is collected from one of the SHG grating ports (both are tested). Any detuning between the fundamental and SHG excitation wavelengths and their respective resonant modes reduces conversion efficiency. To realize mutual resonance, the device is tested on a temperature-controlled stage. Heating the device causes both resonances to redshift at different rates, allowing relative tuning. SHG conversion efficiency is measured as a function of input wavelength at multiple temperatures to find the maximum conversion efficiency.

3.1.3 Results and discussion

Quasi-phase matched resonances were found in device SHG01 at a fundamental wavelength of 1523.1 nm and in SHG02 at 1549.1 nm. The quasi-phase matching condition was identified by the strong and highly temperature-dependent second harmonic conversion of light at the fundamental resonance, as shown in Fig. 3.3. In devices in which only single-resonance enhancement is observed, both the conversion efficiency and the effect of temperature are far weaker. A maximum waveguide-to-waveguide conversion efficiency η of 175% W^{-1} was observed in SHG01. η includes SHG signals propagating in both directions of the SHG waveguide. The maximum conversion efficiency as a function of temperature followed a Lorentzian profile with a full-width-at-half-maximum of ~ 4 °C. (Fig. 3.4(a)), with the peak efficiency wavelength redshifting linearly to follow the fundamental resonance (Fig. 3.4(a)).

The assymmetrical shape of the SHG efficiency curves (inset Fig. 3.3(a)) is attributed to a redshift of the resonance as it is heated by the laser.

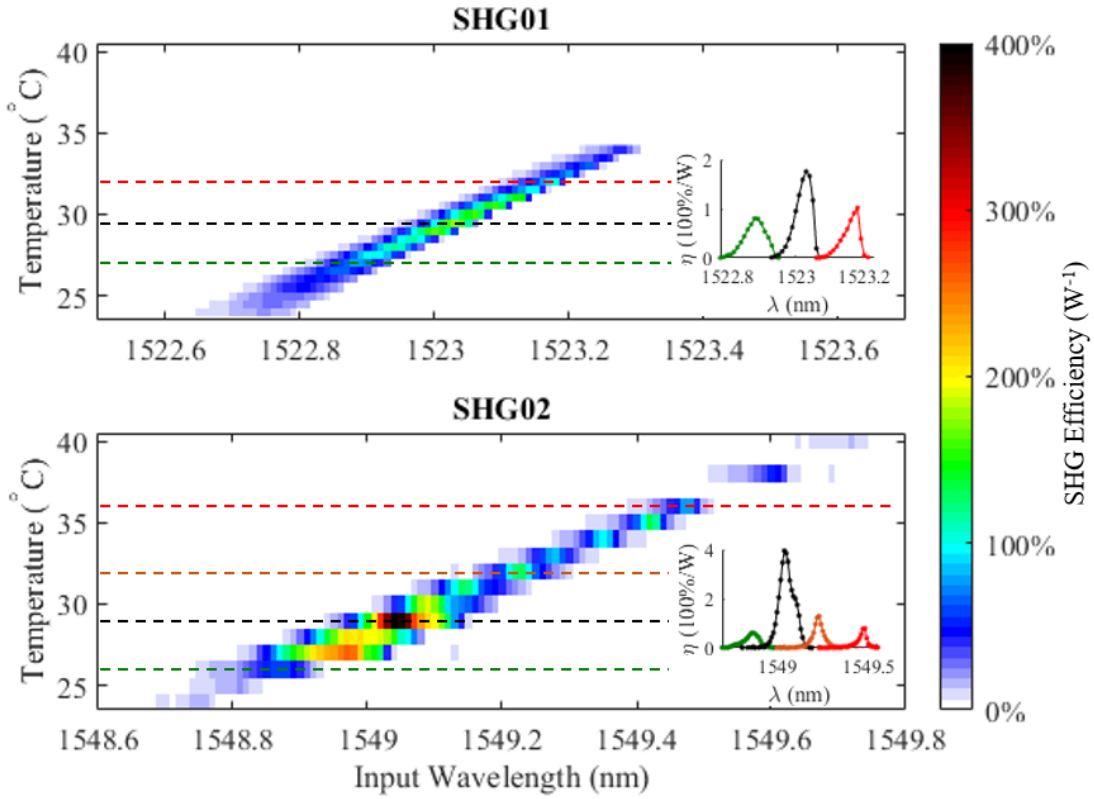

Figure 3.3: (a) SHG conversion efficiency of device SHG01 as a function of both temperature and input wavelength. Conversion efficiency profiles at 27 (green), 29.5 (black), and 32 °C (red) are inset. (b) Conversion efficiency of SHG02, with profiles at 26 (green), 29 (black), 32 (orange), and 36 °C (red). Asymmetry from thermal bistability is visible in the conversion efficiency profiles of both devices and becomes more pronounced with stage temperature and input laser power. Due to resonance splittings, SHG02 exhibits additional asymmetry as well as efficiency peaks at multiple temperatures.

Device SHG02 exhibited both a higher maximum efficiency of 400% W^{-1} as well as a more complex dependence on the temperature and fundamental wavelength (Fig. 3.3(b)). Due to a splitting of both the fundamental and second harmonic resonances [40], SHG02 exhibited efficiency peaks at multiple temperatures instead of the single peak seen in SHG01. The double-humped structure in the peak efficiency curve (black curve, inset of Fig. 3.3(b))

is attributed to these split resonances.

Figure 3.4(c) shows the SHG efficiency, measured from only one SHG grating, as a function of the fundamental input power on double resonance for SHG02. As expected, the SHG power increases quadratically with the fundamental power, with no sign of depletion at waveguide input powers of up to 3 mW. The peak waveguide-to-waveguide conversion efficiency is 0.84% in device SHG02. Increasing the waveguide input power beyond 3 mW resulted in thermal optical bistability [3], causing a discrete hop of the resonance when tuning the fundamental on resonance. This relatively low absolute conversion efficiency points to the practical need to increase the per input power efficiency for quantum conversion applications as well as a limit on the total SHG power that may be produced for classical applications.

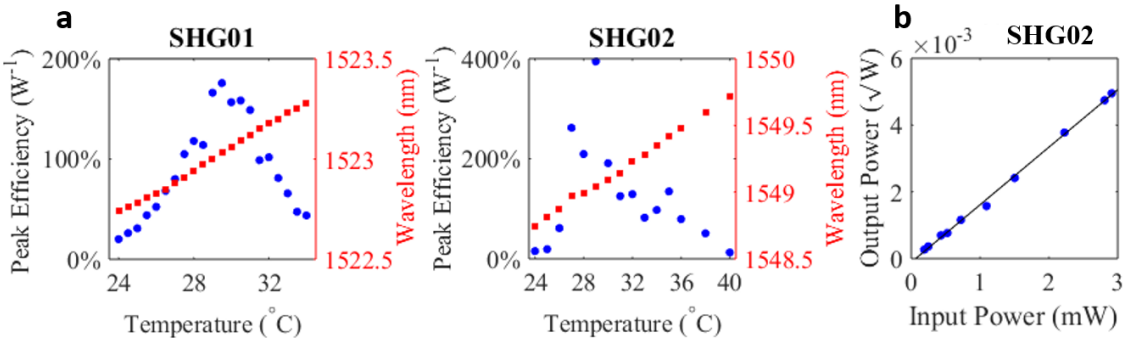

Figure 3.4: (a) Maximum SHG efficiency as a function of temperature for both devices. The red squares are the corresponding fundamental wavelength as a function of temperature. (b) Square root of the SHG output power as a function of fundamental input power, showing the expected linear dependence. Both input and output powers are calculated in-waveguide powers.

To compare the experimental device performance to the simulations (Eq. (3.1)), it is necessary to know the coupling Q_c and intrinsic Q_i of both modes. Based on transmission measurements, the fundamental and second harmonic resonances of both devices are not critically coupled, a condition that is met when $Q_c = Q_i$, and $T = 0$. The measured finite T

gives us only the magnitude of the difference between Q_c and Q_i, $T = |Q_i - Q_c|^2/(Q_i + Q_c)^2$. Rewriting Eq. (3.1) in terms of the T_1 and T_2, we obtain

$$\eta_{\text{theory}} = \frac{P_{2,out}}{P_{1,in}^2} = \frac{|\chi^{(2)}|^2}{\epsilon_0 \lambda_1^3} |\bar{\beta}|^2 \frac{2}{\omega_1} Q_1^2 Q_2 \left(\frac{1 \pm \sqrt{T_1}}{2} \right)^2 \frac{1 \pm \sqrt{T_2}}{2}, \tag{3.4}$$

in which the + signs correspond to the case where both modes are overcoupled, $Q_c > Q_i$, and the − signs to the case where both modes are undercoupled $Q_c < Q_i$. Using the measured Q's and T's in Table 3.1 and the calculated $\bar{\beta}$ from Sec. 3.1.1, we are only able to obtain reasonable agreement between experiment and theory in the case where both modes are overcoupled. The SHG efficiency in this case is $\eta_{\text{theory,oc}}^{\text{SHG01}} = 230\%\ \text{W}^{-1}$ and $\eta_{\text{theory,oc}}^{\text{SHG02}} = 425\%\ \text{W}^{-1}$ and corresponds to the highest theoretical efficiency. For SHG02, $\bar{\beta}$ (Eq. (3.2)) is calculated for a standing wave instead of a traveling wave due to the observed resonance splitting.

To further investigate the coupling regime, the coupling regions of both devices were imaged and measured by scanning electron microscopy and simulated by finite-difference-time-domain and supermode analysis (Section 3.1.5). Within the measurement uncertainty, the coupling quality factor for the 775 nm mode could be as low as 1.2×10^3 and as high as 1×10^6, so overcoupling of this mode is plausible. The lowest reasonably attainable coupling Q_{1c} for the 1550 nm mode was 1.5×10^5, significantly higher than the measured loaded quality factors. This analysis indicates the fundamental mode is most likely undercoupled, in which case theoretical calculations predict much lower conversion efficiencies than observed. Due to this uncertainty in the coupling factors, we are unable to reconcile the experimentally measured efficiencies with these simulations at this time. However, theoretical calculations do not include the effect of surface roughness or sidewall angles so other coupling mechanisms may be a factor.

3.1.4 Measurement calibration

All reported SHG conversion efficiencies are on-chip efficiencies, i.e. based on input and output power in the on-chip waveguides. On-chip powers were derived from off-chip efficiency measurements. Grating coupler efficiency was measured by comparing the transmission

spectrum from each coupling photonic circuit to a reflection spectrum from the thermal oxide substrate. In Fig. 4.1(a), the telecom coupling circuit is pink and the SHG/near-infrared coupling circuit is blue. Near-infrared spectra were measured using a supercontinuum laser for excitation and detected by a grating spectrometer with a CCD detector. Telecom spectra were measured using a scanning laser for excitation and a power meter for detection.

Excitation polarization was adjusted using a $\lambda/2$ plate directly before the objective to excite TE (1550 nm) or TM (775 nm) modes. Reflected excitation light was filtered from the collection path using both a cross-polarizer and a spatial filter (a pinhole) to select the output grating coupler. The efficiency of a single grating was calculated from the power transmission spectrum assuming identical input/output grating couplers and negligible on-chip losses. This assumption of identical couplers is reasonable for SHG01 in which the SHG efficiency is similar when exciting either telecom grating coupler. There is a temperature-dependent discrepancy for SHG02 which is attributed to the splitting of the resonances due to backscattering [40]. Near the resonances of interest, the efficiency of the telecom grating coupler for device SHG01 (SHG02) was measured as 22% (19%). Efficiency of the near-infrared grating was 3.2% (7.5%). Transmission measurements through all off-chip optical components were conducted (depicted in Fig. 3.1(b)). The total telecom power delivered to grating coupler input is $0.31 \times P_{\mathrm{RefPD}}$ in which P_{RefPD} is the power measured on the reference photodiode. Including the grating coupling efficiency, the total telecom power inside the waveguide is $0.068 \times P_{\mathrm{RefPD}}$ ($0.059 \times P_{\mathrm{RefPD}}$) for SHG01 (SHG02).

For SHG experiments, the SHG power is measured at the visible photodiode (VisPD). In these measurements there is no pinhole in the collection path. Transmisson measurements through the bulk optics for both H and V polarized light (corresponding to the two grating orientations) were measured. Including the grating efficiency, for SHG01 we find the SHG power inside the waveguide corresponds to $114 \times P_{\mathrm{VisPD}}$ ($71 \times P_{\mathrm{VisPD}}$) for H (V) polarized light, while for SHG2 the power inside the waveguide is $48 \times P_{\mathrm{VisPD}}$ ($30 \times P_{\mathrm{VisPD}}$) for H (V) polarized light.

3.1.5 Coupling region simulations

Simulations of these devices are based on as-fabricated device dimensions measured using scanning electron microscopy (SEM). Measured features are illustrated in Fig. 3.6. We measured both the top and bottom dimensions for each feature. Figure 3.6 shows the top dimensions (green brackets) and bottom dimensions (white brackets). Averages of the two measurements are given in Fig. 3.5. Assuming a trapezoidal line profile, the measured sidewall angle is ~ 85 degrees. Due to this angled sidewall, the top dimensions of the ring and waveguide are smaller than the bottom dimensions and the top dimension of the gap is larger than its bottom dimension. This trapezoidal profile reduces simulated nonlinear overlap $|\bar{\beta}|$ to 1.27×10^{-4}, reducing theoretical conversion efficiency by up to 20%. For our coupling simulations, we used vertical sidewalls at the mean width.

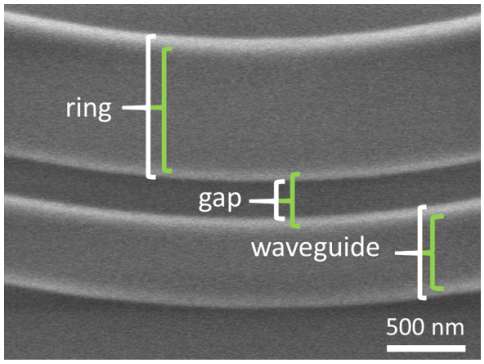

	SHG01		SHG02	
	Min	Max	Min	Max
Telecom waveguide	476	542	510	537
Telecom ring	769	861	834	870
Telecom gap	278	312	261	290
SHG waveguide	140	160	134	168
SHG ring	824	870	830	864
SHG gap	121	152	130	148

Figure 3.5: (Left) Device dimensions in the coupling region, shown for the telecom coupling region of device SHG01. White (green) brackets indicate the bottom (top) of the feature.(Right) The measured average dimensions (nm) for each feature for each coupling region for the two devices.

The coupling efficiency of each wrapped waveguide region was simulated by supermode analysis. As shown in Fig. 3.6(a), if the azimuthal mode number of the curved waveguide mode $|w\rangle$ is similar to the ring resonator mode $|r\rangle$, the two modes combine to form in-phase ($|+\rangle$) and out-of-phase ($|-\rangle$) supermodes when the structures are brought together in the coupling region. Light from the two original modes couples into the supermodes when the waveguide approaches the ring and then couples back into the original modes

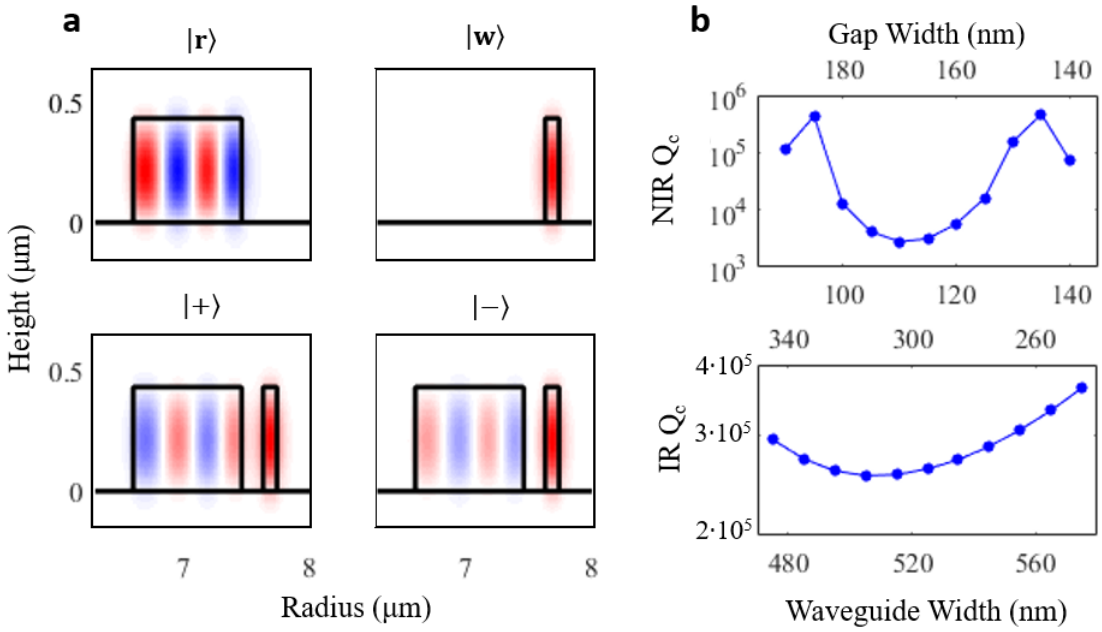

Figure 3.6: (a) Separate mode profile cross-sections (λ = 775 nm) for the ring resonator ($|r\rangle$) and waveguide ($|w\rangle$) that compose the coupling region. When the two structures are combined, these modes split into two supermodes $|+\rangle$ and $|-\rangle$. (b) Coupling quality factors (logarithmic scale) for IR and NIR modes of a 860 nm wide ring, with gap width (top axis) decreasing as waveguide width (bottom axis) increases. Within measurement uncertainty, wider ring resonators reach slightly lower minimum coupling Q with narrower gaps.

when the waveguide diverges. The relative phase of the supermodes determines how light is distributed between the original modes. Because the supermodes propagate with distinct azimuthal mode numbers m^+ and m^-, the relative phase changes along the coupling region, allowing energy to be transferred from ring to waveguide or vice versa. The field coupling strength κ of a single pass through the coupling region is

$$\kappa = \langle r|+\rangle\, e^{im^+\theta}\, \langle +|w\rangle + \langle r|-\rangle\, e^{im^-\theta}\, \langle -|w\rangle\,, \tag{3.5}$$

where θ is the angular length of the waveguide wrap. In our devices, the telecom (SHG) coupling waveguide wraps around 51° (44°) of the ring. The resulting coupling quality

factor of the ring is

$$Q_c = \frac{4\pi^2 R n_g}{\lambda_0 \kappa^2}, \tag{3.6}$$

where R is the ring radius, λ_0 is the free-space wavelength of the resonance, and n_g is the group index of the ring resonator mode. Coupling strengths and quality factors were simulated over the range of measured device dimensions summarized in Fig. 3.5. As shown in Fig. 3.6(b), coupling to the second-harmonic mode is very sensitive to variations in device dimensions. Within the range of device measurements, Q_c can vary from 1.2×10^3 to 1×10^6, indicating that this mode may be either overcoupled or undercoupled in each device. The telecom coupling region is less sensitive. Most configurations within the range of measurement variations yielded Q_c between 1.5×10^5 and 5×10^5. Since this entire range is significantly larger than the measured loaded quality factors, the telecom mode is likely undercoupled in both devices. For selected devices, the power coupling of a light pulse passing through the coupling region once was simulated using Lumerical FDTD Solutions. Coupling quality factor was calculated from this single-pass coupling and the round trip time of a light pulse in the ring. This method gave similar results for the plausible range of quality factors.

3.1.6 Conclusion and outlook

In summary, we observe near 400%/W SHG conversion efficiency in waveguide-integrated GaP resonators. The high conversion efficiency is achieved with resonant enhancement of both the fundamental and second harmonic modes, meeting the quasi-phase matching requirement, and achieving high mode-overlap in small mode-volume structures. These experimental results indicate two areas in which device performance can be immediately and significantly improved. Independent coupling for each mode was vital to exceeding the efficiency of earlier GaP devices, but achieving critical coupling could further improve performance. Assuming intrinsic quality factors Q_i of 10^5 (consistent with our current measurements), the expected SHG efficiency exceeds 8000%/W. Reducing the diameter of these simple rings to 5 µm should increase $|\bar{\beta}|^2$ by at least a factor of 3. Under such a regime of operation, pump depletion would occur at modest powers $<<$ 1 mW, avoiding heating-

induced optical bi-stability. Critical coupling to such small rings may prove challenging, but recent theoretical results utilizing inverse design methods have demonstrated single waveguide couplers capable of achieving critical coupling at multiple frequencies [32]. Finally, the ability to achieve higher nonlinear coupling factors $\bar{\beta}$ in ring resonators is largely hampered by their diminishing capacity to confine light with decreasing sizes. While photonic crystals and associated structures can overcome such a tradeoff [14], they typically can only do so over narrow bandwidths. Recently proposed inverse design strategies [39, 64] point a way toward new kinds of multi-mode cavities capable of confining light at disparate wavelengths in ultra-small volumes, and exhibiting orders of magnitude larger $\bar{\beta}$ factors, the subject of ongoing experimental efforts.

3.2 Generation 2

A second generation of ring resonators was designed for a 250 thick GaP membrane. In addition to reducing mode volume and therefore increasing β, the thinner material was intended to eliminate vertically-split higher-order modes at the shorter process wavelengths. This would facilitate mode identification by reducing the overall number of ring modes. Because the first generation of triple-resonant DFG rings could not be fully tested (see Sec. 4.2), a more reliable double-resonant SHG ring was designed for this generation as well.

The second generation SHG resonator design (SHG2.1) was a single ring resonator in 250 nm thick GaP with an interior radius of 4.5 µm. The waveguide width was varied from 995 nm to 1015 nm over an array of 40 devices. As in the first generation design, the ring was designed for QPM with a $TE_{0,0}$ fundamental mode near 1550 nm and a $TM_{0,3}$ second harmonic mode near 775 nm, with each mode coupled to a separate wrapped waveguide. Multiple resonator arrays were fabricated with different coupling specs, with target coupling quality factors for both modes ranging from 10^4 to 10^6 to offset fabrication variations. The coupling region design for this and subsequent device generations was modified to include the angled sidewalls of the ring resonator and waveguide. Also, elliptical focusing grating couplers were introduced in this design generation to suppress back reflections in the input/output circuits and reduce the resulting Fabry-Perot interference patterns in the

transmission spectra. These grating couplers provided a much smoother grating efficiency spectrum with minimal reduction in maximum efficiency, so they were used in all subsequent device chips.

The thinner GaP and smaller radius increased $|\beta|^2$ to $7.5\,\mathrm{J}^{-1}$ compared to $3.75\,\mathrm{J}^{-1}$ in the first generation design, but the intrinsic quality factor of the fundamental mode was substantially degraded. Because the target coupling for each mode was not varied independently, none of the fabricated devices exhibited near-critical coupling to both modes. Consequently, the conversion efficiency was lower than the first generation ring resonators, both experimentally measured and theoretically calculated for optimally coupled devices. The highest conversion efficiency observed in second generation devices was $\sim 160\%/\mathrm{W}$, in two different resonators.

While testing the second-generation SHG resonators, a more methodical and efficient method was developed for searching large arrays of devices for resonators that can be tuned to QPM double resonance. For each device, the telecom input laser was coupled into the corresponding grating coupler, and the laser wavelength was scanned over a range of 1500-1565 nm at a rate of 10 nm/s. Even with moderate input power, a flash of converted light could be observed on a silicon CCD camera as the laser scanned over any telecom-band ring mode, as shown in Fig. 3.7. If the telecom resonance was close to QPM double resonance with a NIR-band resonance, the converted light would be far brighter. Repeating this measurement at multiple temperatures would confirm double resonance in bright devices through their temperature sensitivity while also providing estimates of optimal operating temperatures. The second-generation resonators were also tested using pulsed excitation, allowing characterization of frequency conversion performance at higher input powers while avoiding the thermal bistability observed in the first design generation.

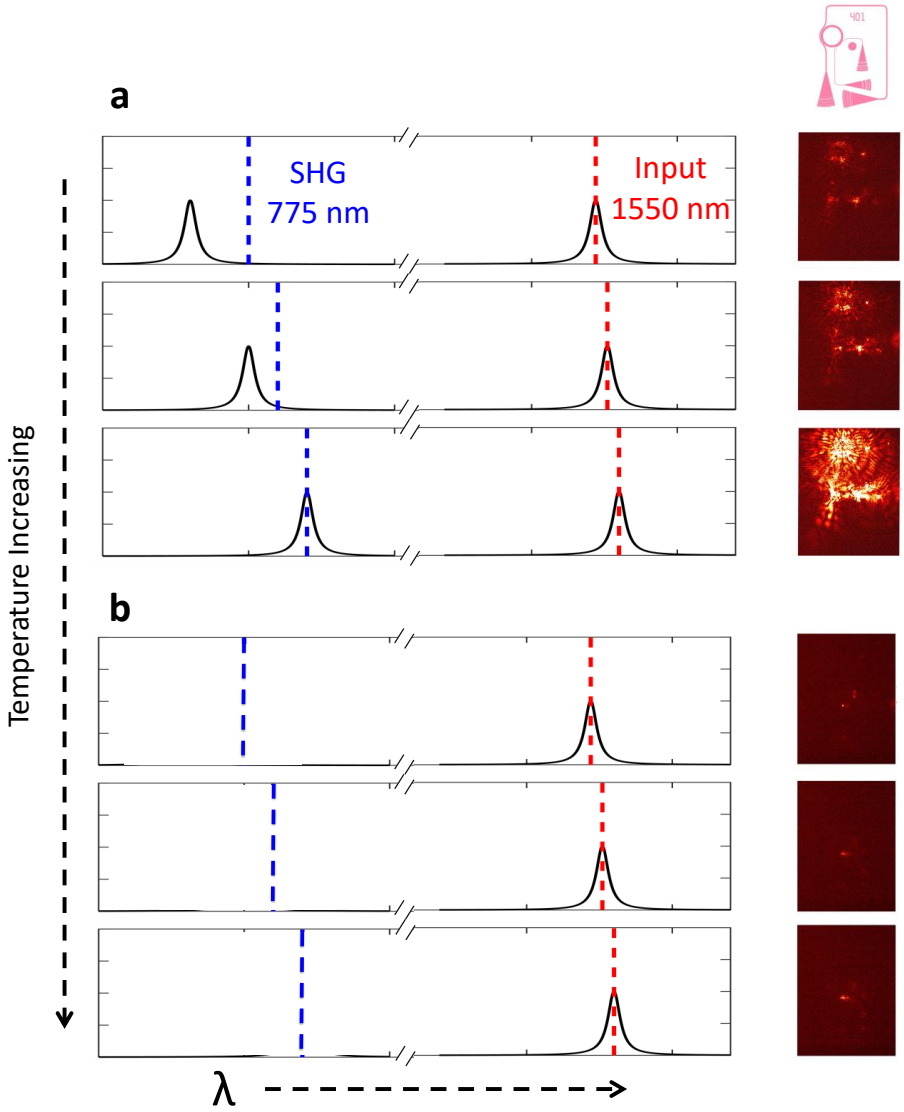

Figure 3.7: Illustration of the SHG measurement used to identify double resonant devices. (a) shows a device that begins somewhat detuned from double resonance. Excitation of the telecom fundamental mode produces second harmonic light at half the wavelength, but the conversion process is only slightly enhanced due to the detuning. Increasing temperature redshifts both resonance into double resonance. The additional resonant enhancement produces much brighter SHG, shown in the camera images to the right. (b) shows a device that is far from double resonance. Changing temperature has no effect on resonant enhancement, so the SHG remains dim.

Chapter 4

DIFFERENCE AND SUM FREQUENCY GENERATION

This chapter presents device designs and measurement results for triple-resonant GaP ring resonators intended for difference frequency generation (DFG) from visible (637 nm) to telecom (1550 nm) wavelengths with a 1081.4 nm pump. A total of eight resonator designs were developed and fabricated over three design generation. Triple-resonant frequency conversion was observed only in the two third-generation ring designs. Due to the availability of telecom-band lasers and visible-band photodectors from the earlier SHG experiments, described in Chapter 3, the frequency conversion performance of these devices was tested via telecom-to-visible sum frequency generation (SFG) measurements instead of the planned DFG process. The resonators provide the same enhancement to both of the complementary processes, so the DFG conversion efficiency can be derived from the observed SFG performance. The maximum measured small-signal SFG power conversion efficiency was $\sim 8000\%/\mathrm{W}$, which corresponds to a visible-to-telecom DFG photon conversion efficiency of $\sim 3300\%/\mathrm{W}$.

Difference and sum frequency conversion in $\chi^{(2)}$ materials provide an efficient and general means to access new wavelengths with established sources. Conversion efficiency in these processes scales with field intensity, motivating resonant geometries to both increase per-unit power conversion efficiency and decrease the interaction volume and thus footprint. Resonant geometries are of particular interest for applications where scalability is critical, for both footprint and power consumption. One such application of particular interest is fiber-based quantum repeater networks, which additionally require devices to operate at the single photon level. Single photon frequency conversion processes, also called quantum frequency conversion (QFC), will enable a wider range of qubits to access telecommunication wavelengths, enabling long-distance entanglement [33, 11, 69, 78, 66, 70, 19]. Further, fine control of the converted photon wavelength could be used to erase inhomogeneities

in emission wavelength, permitting high-fidelity remote entanglement of inhomogeneous qubits by two-photon interference. [4, 74, 36]. SFG may also be useful as an upconversion mechanism for efficient room-temperature photon detection [1, 57] and could provide a bridge between disparate qubit platforms [2].

QFC based on a material's second order nonlinear susceptibility $\chi^{(2)}$ utilizes a strong coherent pump to enable interactions between two single-photon modes, so it is restricted to sum- and difference-frequency generation (SFG and DFG) processes with three distinct wavelengths. Single-photon SFG/DFG has been demonstrated in macroscopic optical cavities [1, 58] and PPLN waveguides [25, 51, 19, 65], with internal maximum photon conversion efficiencies as high as 86% for pump powers of hundreds of mW. In nanophotonic resonators, triply resonant frequency conversion processes have been demonstrated using two detuned inputs on a single resonance [73] or similar wavelength resonances of the same transverse mode [77, 26]. In both cases, two of the three wavelengths involved in the conversion process are restricted to a range of picometers to several nanometers. However, implementing frequency conversion interfaces for specific quantum emitters, e.g. the nitrogen-vacancy [19, 31] or silicon-vacancy [29, 8] in diamond, will typically require long jump frequency changes with three resonances at widely disparate wavelengths.

Because the third design generation produced the most notable measurement results, it will be presented first. The first two DFG generations are described later in the chapter.

4.1 Generation 3[1]

For the third generation of DFG devices, two ring resonators were designed for a 430 nm thick GaP membrane. The thicker material from the first design generation was used again due to the reduced telecom-band intrinsic quality factor and conversion efficiency observed in second-generation ring resonators. The first ring resonator in this generation (DFG3.1) was designed with the standard mode combination of TE_{00}, TE_{00}, and TM_{03}, respectively, for the telecom, pump, and visible modes. With a ring width of 675-710 nm and radius of 5300 nm, this mode combination was simulated to satisfy the QPM condition $M = -2$, with

[1] Material in this section is reproduced from Ref. [42], which has been accepted and is pending publication in *Optics Express*.

a nonlinear overlap of $|\beta|^2 = 27.9\,\mathrm{J}^{-1}$. A second ring design (DFG3.2), was developed using a $\mathrm{TE}_{00}/\mathrm{TE}_{01}/\mathrm{TM}_{04}$ telecom/pump/visible mode combination, which produced a higher nonlinear overlap $|\beta|^2 = 68\,\mathrm{J}^{-1}$ with a ring width of 795-825 nm and radius of 4425 nm. To avoid the anomalous coupling issues from the second-generation DFG resonators, combined coupling regions were designed for each resonator type so that both infrared ring modes were deliberately coupled to a single waveguide. Similarly, the grating couplers for these shared coupling circuits were optimized to operate at both the telecom and pump wavelength bands. The infrared coupling region for DFG3.1 used the same wrapped-waveguide configuration as previous designs, but a straight-waveguide coupling region was required for DFG3.2 due to the larger difference in effective index between the telecom and pump ring modes. Three infrared coupling regions and three visible coupling regions were designed for each resonator type. Resonators of both designs were fabricated in 9 arrays of 30 devices with varying ring width, with each array using a different combination of visible and infrared coupling.

4.1.1 Model and design

The GaP ring resonators were designed to maximize waveguide-to-waveguide on-chip conversion efficiency. For a process that converts visible photons in the ω_3 input mode to telecom photons in the ω_1 output mode using a pump at $\omega_2 = |\omega_3 - \omega_1|$, the theoretical power conversion efficiency η in the low-power limit is [16]:

$$\frac{\eta}{P_{2,in}} = \frac{P_{1,out}}{P_{2,in}P_{3,in}} = 64\,|\beta|^2\,\frac{\omega_1}{\omega_2\omega_3}\,\frac{Q_1^2Q_2^2Q_3^2}{Q_{c1}Q_{c2}Q_{c3}}, \tag{4.1}$$

where Q_n and Q_{cn} are the total and coupling quality factors of mode n, and P_n is the input/output power for each mode. Small-signal or normalized conversion efficiency is defined as $\eta_{ss} = P_{1,out}/P_{2,in}P_{3,in}$. Because the quality factors are primarily limited by material properties and fabrication, we focus on maximizing the nonlinear mode overlap β, which encompasses the effects of mode field distribution and polarization, phase matching, and mode volume:

$$\beta = \frac{1}{4\sqrt{\varepsilon_0}} \frac{\int \sum_{i,j,k} \chi^{(2)}_{ijk} E^*_{3i} \left(E_{1j} E_{2k} + E_{2j} E_{1k}\right)\, dV}{\sqrt{\int \epsilon_1 |E_1|^2\, dV} \sqrt{\int \epsilon_2 |E_2|^2\, dV} \sqrt{\int \epsilon_3 |E_3|^2\, dV}}. \tag{4.2}$$

E_n and ϵ_n are the electric field distribution and relative permittivity for mode n, and i, j, and k are crystallographic directions of the nonlinear medium. The ring resonators were designed for 430 nm thick GaP on silicon oxide. Due to the zincblende crystal symmetry of GaP, $\chi^{(2)} \neq 0$ for $i \neq j \neq k$, so nonlinear interactions require mutually perpendicular field components in each mode. For a radially symmetrical structure in [1 0 0]-normal GaP, the nonlinear overlap β becomes:

$$\begin{aligned}
\beta &= \frac{\left|\chi^{(2)}\right|}{4\sqrt{\varepsilon_0}} \frac{\int_{NL} \left[(A_1 - iA_2) e^{i(M+2)\theta} + (A_1 + iA_2) e^{i(M-2)\theta}\right]\, dV}{\sqrt{\int \epsilon_1 |E_1|^2\, dV} \sqrt{\int \epsilon_2 |E_2|^2\, dV} \sqrt{\int \epsilon_3 |E_3|^2\, dV}} \\
M &= m_1 + m_2 - m_3 \\
A_1 &= E_{1z}(E_{2r} E^*_{3\theta} + E^*_{3r} E_{2\theta}) + E_{2z}(E_{1r} E^*_{3\theta} + E^*_{3r} E_{1\theta}) + E^*_{3z}(E_{1r} E_{2\theta} + E_{2r} E_{1\theta}) \\
A_2 &= E_{1z}(E_{2r} E^*_{3r} - E_{2\theta} E^*_{3\theta}) + E_{2z}(E_{1r} E^*_{3r} - E_{1\theta} E^*_{3\theta}) + E^*_{3z}(E_{1r} E_{2r} - E_{1\theta} E_{2\theta}),
\end{aligned} \tag{4.3}$$

where E_{ir}, E_{iz}, and $E_{i\theta}$ are the radial, vertical, and azimuthal field components and m_i is the azimuthal mode number of each mode.

The nonlinear overlap exhibits a sinc-like dependence on the quasi-phase matching (QPM) condition $M = \pm 2$. The overlap is greatly diminished for single- or double-resonant processes, and vanishes entirely for unmatched triple resonance ($M \neq \pm 2$). Consequently, when the designed set of modes are tuned to triple resonance, it is unlikely that any other frequency conversion process with the same input wavelengths, such as second harmonic generation, will be significantly enhanced by the resonator. Each term in the overlap is a product of one vertical and two in-plane field components, which in practice restricts mode selection to one TM and two TE modes. The difference in interactions between radial and azimuthal field components in the $M = +2$ and $M = -2$ cases biases the overlap integral toward the inside and outside edge of the ring, respectively, which allows significant interactions between modes with even and odd symmetry [67].

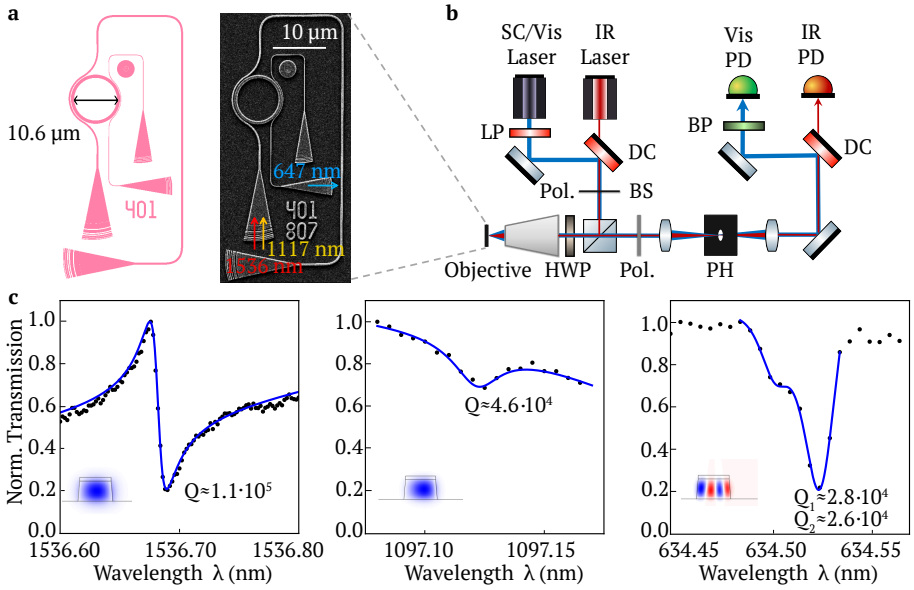

Figure 4.1: (a) Device layout and SEM image of a GaP nonlinear ring resonator coupled to input/output waveguide circuits, one for 637-647 nm visible light (blue) and one combining 1530-1565 nm telecom (red) and 1080-1120 nm NIR (yellow) light. Each coupling circuit includes two grating couplers to allow single-wavelength transmission measurements in addition to the SFG measurement marked on the SEM. (b) Free-space coupled microscope setup for device characterizations and SFG measurements. Cross-polarization and the pinhole (PH) are used to eliminate reflected/scattered input light. IR: infrared, SC: supercontinuum, PD: photodiode, BS: beamsplitter, DC: dichroic, HWP: half-wave plate, BP: band-pass filter, LP: long-pass filter. Input and output filter wavelengths were adjusted for different measurement wavelengths. (c) The transmission measurements from telecom, near-infrared and visible resonances in device SFG01, along with fitted Fano/Lorentzian curves. Background is approximated with linear functions. The Fano shape of the telecom resonance results from the narrow-band fundamental resonance overlapping the wavelength band of a low-Q higher order resonance. Ring cross-sections with vertical (visible) or radial (telecom and NIR) electric field distributions are inset for each mode. Transmission at each wavelength was measured using a tunable laser input and wavelength-appropriate photodiode. Due to difficulties with measuring and fitting the specific resonances used for triply-resonant SFG testing, the fits shown here use different instances of the same family of resonances.

The ring resonator was designed using the Lumerical MODE bent-waveguide solver to simulate propagation constants and nonlinear overlap for telecom, NIR, and visible modes. Two designs were explored. In the first design, the ring width and radius were optimized to maximize β while satisfying the $M = -2$ quasi-phase matching condition for TE_{00}, TE_{00},

and TM_{03} modes at 1550 nm, 1081.4 nm, and 637 nm, respectively (Section 4.1.6). The final ring dimensions for this design are a radius of 5.3 µm, measured to the center of the ring, with ring width varied from 675-704 nm in 1 nm increments to compensate for fabrication variations. The second design utilized TE_{00}, TE_{01}, and TM_{04} modes at 1550 nm, 1081.4 nm, and 637 nm. This mode combination allowed more than a two-fold increase in simulated $|\beta^2|$ compared to the first design in exchange for potentially reduced quality factors. The fabricated devices exhibited lower SFG efficiency compared to the first design, shown in Fig. 4.5, and will not be discussed further here.

From Eq. 4.1, the small-signal conversion efficiency is maximized when all three modes are critically coupled ($Q_c = 2Q$), while the quantum limit of the photon conversion efficiency can be increased to approach unity by overcoupling the input and output modes [16]. With a simulated nonlinear overlap of $|\beta|^2 = 27.8\,\mathrm{J}^{-1}$ for the first ring design, a critically coupled device with a combined total quality factor of ($Q_1Q_2Q_3 = 10^{15}$) is simulated to provide a waveguide-to-waveguide photon conversion efficiency of $\sim 13.5\%/\mathrm{mW}$ between visible and telecom wavelengths. Wrapped-waveguide coupling regions were designed to provide a range of target coupling quality factors for each mode, summarized in Fig. 4.5. As shown in Fig. 4.1a, both infrared modes were coupled to a single waveguide, while the visible mode was coupled to a separate waveguide.

4.1.2 Fabrication

The photonic devices were fabricated in a 427 nm-thick [1 0 0]-normal GaP membrane on 1 µm SiO_2 on silicon. The GaP membrane was grown by gas-source molecular-beam epitaxy on an intermediate 300 nm $Al_{0.8}Ga_{0.2}P$ sacrificial layer on a bulk GaP substrate. The sacrificial layer was etched in 3:100 HF:H_2O to release the 2 mm square GaP membrane. The membrane was wet transferred to the oxide substrate [41], which was cleaned with solvents, O_2 plasma, and treated with HMDS adhesion-promoter. The photonic circuit pattern was written by 100 keV electron beam lithography in a ~ 100 nm HSQ resist layer, which was developed with 25% TMAH in water. The resist pattern was transferred to the GaP layer by an inductively-coupled plasma reactive ion etch (ICP-RIE) using a $Cl/Ar/N_2$

(1.0/6.0/3.0 sccm) plasma, which selectively stops at the oxide layer. After fabrication, the HSQ resist could not be removed without potentially damaging the GaP or the oxide substrate, so it was left as partial cladding.

4.1.3 Passive device characterization

The setup shown in Fig. 4.1b was used for both passive and frequency-conversion device testing. Passive device testing consisted of transmission measurements at each wavelength band, which were used to determine the quality factors of the three modes and the grating coupler efficiencies near the resonant wavelengths. The telecom resonances were characterized by scanning an input laser from 1530 nm to 1565 nm and recording the device transmission on an infrared photodiode. Resonance quality factors were calculated based on least-squares curve fits of a Lorenztian or Fano profile on a linear background to account for the grating coupler efficiency curve. For split resonances, the fitting model was expanded with a second Lorentzian. The measured total quality factors of the telecom TE_{00} mode ranged from $\sim 0.9 - 2.9 \times 10^5$. Visible and near-infrared resonances were characterized via transmission spectroscopy with a broadband supercontinuum laser input and grating spectrometer collection. Devices with promising SFG performance were selected for further characterization using scanning narrowband sources (632-640 nm for visible, 1070-1130 nm for NIR). In this subset of devices, visible and NIR quality factors of $\sim 2.5 - 3 \times 10^4$ and $\sim 4.5 - 6 \times 10^4$ were measured, respectively. The transmission measurements for the most efficient SFG device (SFG01) are shown in Fig. 4.1c, with telecom, NIR, and visible quality factors of $1.1 \pm 0.04 \times 10^5$, $4.6 \pm 0.9 \times 10^4$, and $2.8 \pm 0.39 \times 10^4$, respectively.

4.1.4 Triply-resonant device identification

Finding devices that could be tuned to quasi-phase matched triple resonance based on the passive transmission measurements proved difficult due to shallow transmission dips from non-critically coupled resonances in many devices, along with the highly multi-mode nature of the ring resonators in the visible band. Instead, we identified triply-resonant devices using rapid measurements of frequency conversion performance. As illustrated in Fig. 4.2,

frequency conversion processes that are close to triple resonance have greatly enhanced efficiency which depends strongly on the detuning between the converted light and the output resonance wavelength. Consequently, a near triply-resonant device under resonant excitation of two input modes will produce converted light that is both particularly bright and highly sensitive to detuning determined by the device temperature.

Due to the availability of high-quality lasers in the telecom band and detectors in the visible band, we used telecom-to-visible SFG measurements to characterize frequency conversion performance. The designed complementary DFG process is expected to have similar photon conversion efficiency. In order to efficiently explore SFG performance in a three-dimensional parameter space (two input wavelengths and device temperature), we use a broadband supercontinuum laser (SCL) as the pump-band input (filtered to 1000-1200 nm), and combine it with a tunable laser in the telecom band (1530-1565 nm) with approximately 300 µW of power in the waveguide. Converted visible light is collected using a 775 nm short pass filter, 637/22 nm bandpass filter, and a spatial filter to remove both scattered supercontinuum light and second harmonic converted light from the telecom laser. Some portion of the supercontinuum pump provides resonant excitation to every NIR-band mode. Now, when the telecom laser scans over a resonance, visible light is produced by SFG processes within the ring, enhanced by the telecom and a NIR-band mode. The observed intensity of the converted visible light is a function of the detuning of the constituent resonances. A phase-matched visible resonance will not contribute much additional enhancement if the SFG wavelength is substantially detuned. The detuning can be modified by changing device temperature, but the SFG efficiency is not significantly affected until the SFG wavelength approaches the resonance.

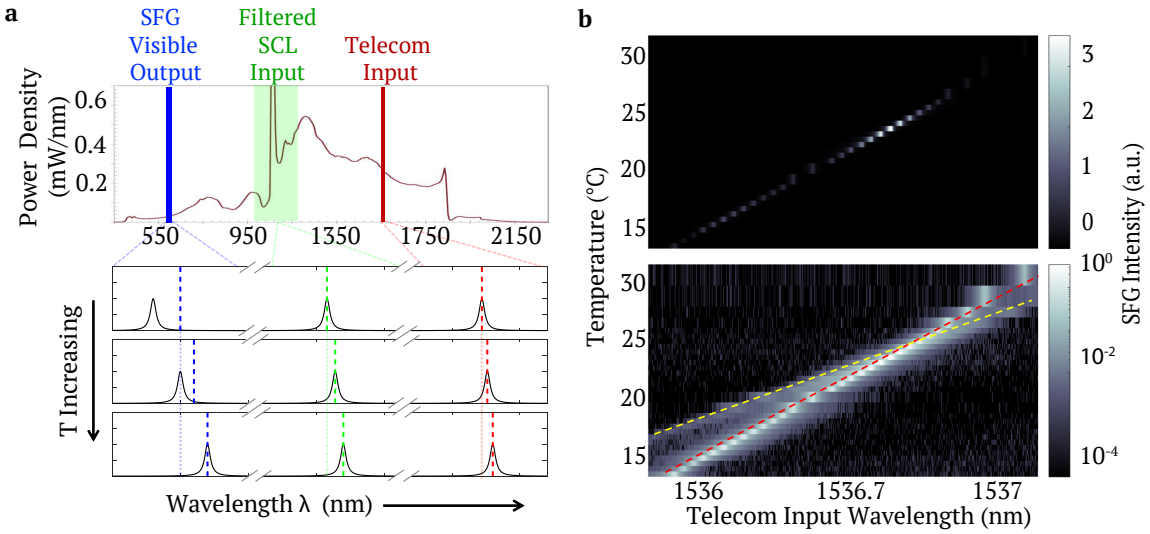

Figure 4.2: (a) The power density of the Whitelase Micro supercontinuum (SCL) laser, with the filtered wavelength band used as an input for SFG marked in green. The wavelength bands for the telecom tunable input laser (red) and visible output collection filter (blue) are also marked. Below is an illustration of the temperature-dependent SFG measurement used to identify triple-resonant SFG processes as described in the text. (b) Supercontinuum-pumped SFG measurements for device SFG01, showing dependence on device temperature and telecom-band input wavelength. Top is a linear-scale colormap and bottom is a logarithmic-scale colormap. The red line marks the telecom-band resonance, and the yellow line marks the input wavelengths that produce SFG light on resonance with the visible-band mode. Conversion efficiency is maximized when both conditions can be satisfied simultaneously (triple resonance).

At this point, SFG efficiency becomes highly sensitive to temperature and peaks when the converted light is on resonance. Consequently, a strong temperature dependence in the intensity of the SCL-pumped SFG in a device indicates a phase-matched triple-resonant SFG process.

We performed supercontinuum-pumped SFG measurements on 123 ring resonators at temperatures from $16 - 40$ °C in 4 °C increments. Most of the tested devices produced some measurable SFG light within this temperature range. Eight resonators with bright, strongly temperature-dependent SFG were selected for further characterization and designated SFG01-SFG08. Supercontinuum-pumped SFG measurements were repeated with a finer temperature sweep to find the optimal operating temperature for each device. As

shown for device SFG01 in Fig. 4.2b, the SFG intensity peak red-shifts with increasing temperature to follow the high-Q telecom resonance. The peak intensity is maximized at a device temperature of $\sim 25°C$ at which the condition of triple resonance met. This condition is apparent on a logarithmic scale in which two SFG peaks can be observed at each temperature: the telecom-band resonance, and a second peak at the input wavelengths that produce SFG light on resonance with the visible-band mode. Similar measurements for the other seven devices are presented in Section 4.1.7.

Spectra of the SFG output were taken to determine the visible SFG wavelength. The visible SFG wavelength combined with the measured telecom input resonance uniquely determines the pump frequency. As shown in Table 4.1, the narrower ring resonators exhibited triple resonance with modes at ~ 1550, ~ 1107, and ~ 647 nm, and wider rings at ~ 1536, ~ 1117, and ~ 647 nm. The discrepancy between the designed and measured process wavelengths may be due to fabrication variations, particularly in the ring coupling regions and sidewall angles.

4.1.5 Frequency conversion efficiency

While the broadband SCL pump allows efficient identification of triple-resonant devices, continuous and narrow-band pulsed inputs allow more precise control of the power used to excite a targeted frequency conversion process. We measure the SFG small signal conversion efficiency of the brightest devices (SFG01 and SFG02) with a 1080-1120 nm tunable CW laser as a pump in place of the SCL. At the optimal temperature found with the SCL measurements, a 2D scan of both excitation lasers over their respective resonances was performed while monitoring the input power from each laser as shown in Fig. 4.3a,b. Similar to the temperature tuning data in Fig. 4.2b, we again observe SFG enhancement from the visible (blue line) and telecom resonances (red line).

Device	Width (nm)	Opt. T (°C)	Est. η_γ (%/mW)	Telecom λ (nm)	SFG λ (nm)	Pump λ (nm)
SFG01	698	25	8.00	1536.7	646.82	1117.0
SFG02	682	18	5.75*	1552.5	646.51	1107.2
SFG03	684	25	~ 5.7	1552.8	646.59	1107.9
SFG04	682	22.5	4.38	1552.4	646.4	1107.6
SFG05	699	22	1.77	1536.3	646.66	1116.7
SFG06	701	25	1.36	1537	647.66	1119.4
SFG07	679	18.5	0.91	1550.9	645.9	1106.9
SFG08	696	31	0.38	1536.5	646.66	1116.6

Table 4.1: Ring width, operating temperature, efficiency and estimated SFG process wavelengths for SFG processes in eight triply-resonant ring resonators, based on supercontinuum-pumped SFG measurements. The visible wavelength of the dominant SFG process was measured with a spectrometer, and the pump-band wavelength was calculated from the telecom input and SFG output wavelengths. Conversion efficiency was measured directly for device SFG01, and estimated for other devices based on a comparison to this value. The efficiency estimate for device SFG03 is less precise due to a damaged visible-band output grating coupler.
* Narrow-band SFG measurements of device SFG02 found a significantly lower conversion efficiency (Section 4.1.7).

SFG measurements with the pump laser near its resonance required additional attenuation to avoid saturating the detector with the peak intensity. Rescaling the signal to compensate for the attention resulted in a heightened noise floor, hiding the enhancement from the pump-band resonance alone. Waveguide-to-waveguide small signal conversion efficiency was calculated from measured input and output powers, grating efficiency, and microscope efficiency (Section 4.1.7).

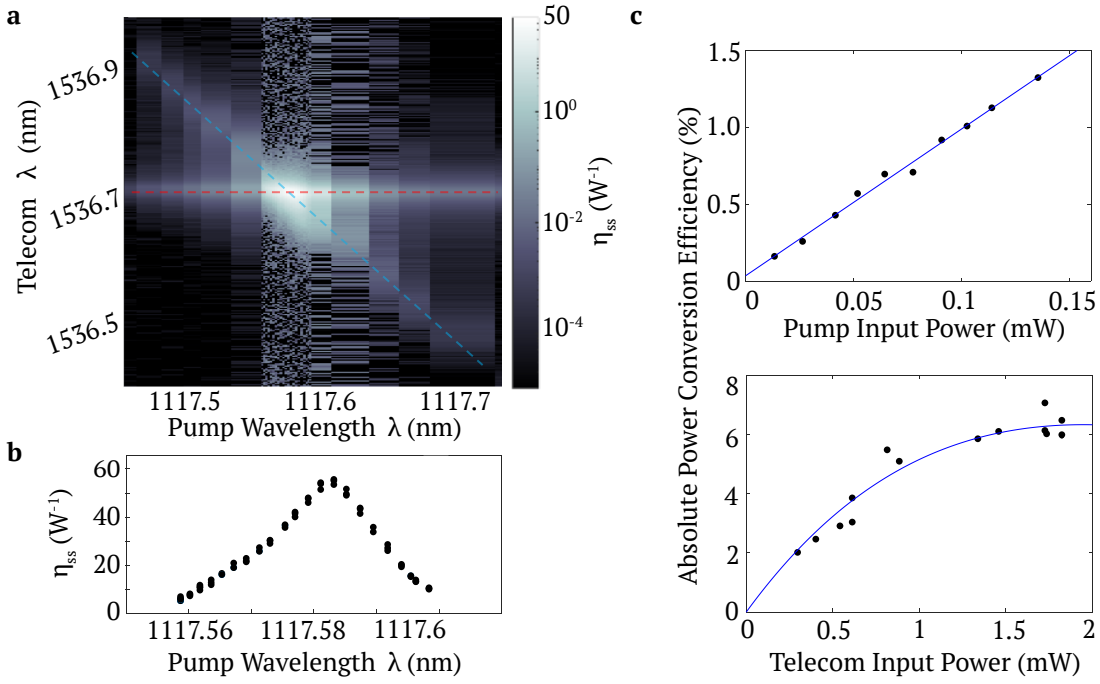

Figure 4.3: (a) Input wavelength dependence of small-signal SFG power conversion efficiency for device SFG01 at its optimal temperature (25°C), using CW telecom and pump inputs with average powers of 100 µW and 82 µW in the waveguide. The red line marks the SFG enhancement from resonant excitation of the telecom mode, and the blue line shows enhancement from to the visible mode applied to combinations of input wavelengths that produce an on-resonance SFG wavelength. The collected SFG signal was attenuated to avoid detector saturation when the NIR wavelength approached resonance, resulting in exaggerated background noise from $\sim 1117.55 - 1117.65$ nm. (b) Detail of the small-signal conversion efficiency peak for device SFG01 around the NIR resonance. The linewidth of the efficiency peak corresponds to a pump mode quality factor of $5.7 \pm 0.2 \times 10^4$, with a maximum conversion efficiency of $4.9 \pm 0.67\%$/mW. (c) Power dependence of absolute conversion efficiency for device SFG01. The top plot shows conversion using low-power CW inputs, varying the NIR-band input power. The bottom plot shows conversion using a constant, low-power CW NIR input with a variable-power pulsed telecom input, which allows higher instantaneous excitation powers while avoiding the effects of resonator heating.

The uncertainty of these conversion efficiency measurements is dominated by uncertainty in grating coupler efficiency, which is transferred to the calculation of on-chip powers from off-chip measurements. For SFG01, grating efficiencies at the telecom, pump, and visible resonant wavelengths were measured as $11 \pm 1\%$, $6.4 \pm 0.1\%$, and $1.1 \pm 0.05\%$. For device

SFG01, the peak small-signal efficiency found with this measurement was $4.9 \pm 0.67\%/\text{mW}$.

Fig. 4.3c (top) gives the absolute power conversion efficiency for SFG01 in the small signal regime. A linear dependence on pump power is observed as expected. To obtain the maximum power conversion, the roles of the telecom and NIR laser were swapped due to the need for higher pump power which can be achieved with an erbium doped fiber amplifier added to the telecom input. Additionally, to minimize resonator heating and optical bistability, a telecom electro-optic modulator was used to pulse the telecom laser. The weaker NIR laser remained in CW mode. We note that the pulse lengths (100 ns) and duty cycle (1%) used are comparable to what would be utilized in single diamond defect applications. As shown in Fig.4.3c (bottom), an absolute power conversion efficiency of $6.3 \pm 0.6\%$ was measured for a peak telecom input power in the waveguide of $1.8 \pm 0.16\,\text{mW}$. In devices targeting single photon conversion, pump depletion is not a factor and over coupling of the single photon modes will minimize back-conversion, allowing much higher maximum conversion efficiency. Fitted curves for the CW and pulsed power dependence measurements yielded small-signal conversion efficiencies of $9.5 \pm 1.3\%/\text{mW}$ and $8 \pm 1.1\%/\text{mW}$, respectively. The variation in measured conversion efficiency may be due to slight variations in input laser alignment or gradual changes in the HSQ cladding [67] altering the optimal temperature of the device.

The small-signal conversion efficiency found for device SFG02 with similar measurements was $\sim 0.37 - 0.59\%\text{mW}$, shown in Fig. 4.7. Estimates of the efficiency for devices SFG03-SFG08 were found by comparing the supercontinuum-pumped SFG intensities to device SFG01, and are given in Table 4.1.

4.1.6 Photonic integrated circuit design considerations

Aperiodic grating couplers were designed to provide off-chip coupling at each wavelength with minimal footprint. These grating couplers are intended to allow independent testing of large arrays of devices and would be replaced with larger, more efficient coupling methods for high-performance applications. Grating designs for each wavelength were generated using a simplified model treating the grating as series of discrete, independent scattering

elements in a waveguide. Scatterer widths and spacings were optimized to maximize overlap between upward-scattered light and a target Gaussian mode shape using a sampled discrete hill climbing algorithm. The detailed coupling behavior from waveguide to free space was simulated by Lumerical 3D FDTD for each grating design candidate. The grating design that provided the highest coupling into a single spot in free space over the target wavelength band was selected. If the simulated grating efficiency peak was offset from the target wavelength, all lengths in the grating design were scaled by up to 5% to red- or blue-shift the efficiency curve. For grating couplers intended for multi-wavelength operation, two design approaches were used. First, gratings that had been designed for one wavelength were FDTD simulated at the second wavelength. If an existing design also provided reasonable performance in the second wavelength band, it would be used as a multi-wavelength coupler. Alternatively, grating designs can be co-optimized for free space coupling at both wavelengths using the hill-climbing algorithm to maximize the product of the two single-wavelength objective functions. However, this second strategy was not employed in this work. The measured grating coupler efficiencies at the telecom, NIR, and visible resonant wavelengths ranged between 11-20%, 5.5-8.5% and 1-2% in these devices. At the design wavelengths of 1550, 1080, and 637 nm, the respective grating efficiencies were simulated as 20%, 17%, and 40%, but the NIR and visible gratings were operated at non-optimal wavelengths.

Wrapped-waveguide ring resonator coupling regions were designed using Lumerical MODE bent-waveguide eigenmode simulations for an extended supermode analysis. For different combinations of coupling waveguide width (w_{wg}) and ring-waveguide separation distance (d), mode profiles and propagation constants were simulated for all modes in the combined ring and waveguide structure. For each combined-structure mode, mode overlaps were calculated for both the ring resonator mode and the targeted waveguide mode. During a single pass through the coupling region, light in the ring mode is divided between the combined-structure modes based on the mode overlaps. The relative phases of these modes evolve as the light propagates in the combined structure for some angular distance θ around the ring. The mode phases affect how much light is coupled into the waveguide mode at the end of the coupling region, and how much remains in the ring. The coupling quality factor Q_c can

then be calculated based on the single-pass ring-to-waveguide coupling and the round-trip propagation time of the ring mode. Values of w_{wg}, d, and θ were selected to provide targeted values of Q_c, which were chosen in a range around experimentally observed quality factors in similar photonic devices [41].

Due to previous observations of pump-band ring modes coupling to telecom-band output waveguides and vice versa, both infrared ring modes were coupled to a single waveguide in these devices. Wrapped-waveguide coupling regions were designed for the first ring design, which used fundamental radially-polarized (TE) modes at both wavelengths. However, a wrapped waveguide design could not be found that could accommodate both the telecom mode and higher-order pump mode in the second ring design. Instead, a straight-waveguide coupling region was used for the infrared modes for that ring design. For straight waveguides, single-pass coupling was simulated using 3D FDTD, and coupling quality factor was calculated as normal. The visible and infrared Q_c targets used for each ring design can be found in Fig. 4.5. For ring design 1, the infrared coupling region used a 320 nm wide waveguide wrapped around a 120 degree section of the ring, with separation distances of 200, 220, and 240 nm for increasing Q_c target values. For coupling to the visible mode, a 50 nm waveguide was wrapped around a 90 degree arc at distances of 200, 215, and 225 nm. The second ring design used a 300 nm straight waveguide to couple to the IR modes, at distances of 140, 160, and 180 nm. The visible coupler for design 2 used a 40 nm with a 45 degree wrap at distances of 160, 175, and 185 nm.

The primary design variables for the ring resonators are ring width w and radius r, since the GaP layer thickness is constant across the MBE chip. The ring dimensions are optimized to maximize nonlinear overlap β while satisfying the quasi-phase matching condition $M = \pm 2$ (Eqn. 3) for a selected set of telecom (1550 nm), visible (637 nm), and pump (1081.4 nm) modes. At each design point, propagation constants and mode profiles for each mode are simulated using Lumerical MODE bent-waveguide eigenmode solver. The propagation constants are used to calculate azimuthal mode numbers m_n, which may be fractional if the precise design wavelengths are not resonant, and $M = m_1 + m_2 - m_3$. Nonlinear overlap β is calculated from the mode profiles. To find valid ring designs, first an arbitrary combination of r and w is evaluated. If quasi-phase matching (QPM) is not satisfied, the ring width is

iteratively modified until a valid design is found ($M \approx \pm 2$). Ring dimensions and β for this design are recorded. Then, ring radius is adjusted, and ring width is again tuned until the same QPM condition is satisfied. This process is repeated while following increasing trends in β (usually, toward smaller radius) until either β is maximized or the ring width or radius becomes too small to confine the highest-wavelength mode without severe degradation of quality factor.

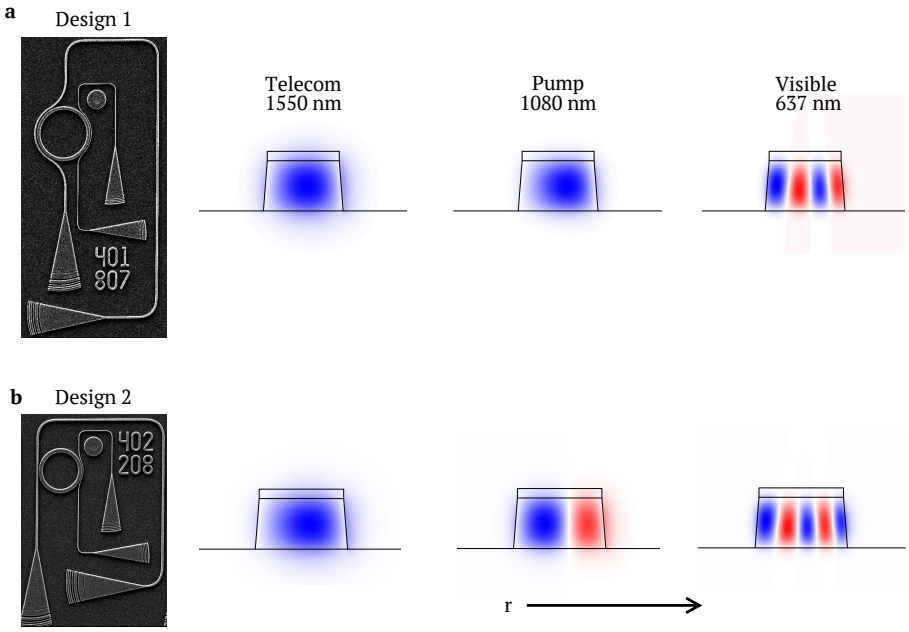

Figure 4.4: SEM images and mode profiles for the primary (a) and alternative (b) ring designs fabricated for this work.

The first ring design in this work was designed with the mode combination of TE_{00}, TE_{00}, and TM_{03}, respectively, for the telecom, pump, and visible modes. With a ring width of 690 nm and radius of 5300 nm, this mode combination was simulated to satisfy the QPM condition $M = -2$, with a nonlinear overlap of $|\beta|^2 = 27.8\,\mathrm{J}^{-1}$. As described in Eqn. 3, a ring resonator in a [1 0 0]-normal zincblende crystal requires two TE modes and one vertically-polarized (TM) mode to provide significant nonlinear overlap β. The shortest wavelength mode was selected to be the TM mode due to previous observations

and simulations that TM mode quality factor is more sensitive to material thickness than TE modes. Satisfying the QPM condition purely by mode engineering requires a higher-order visible mode, with the trade-off that β is usually higher for modes that are closer to the fundamental. The $TE_{00}/TE_{00}/TM_{03}$ combination was selected because it allows phase matching with a ring width that is wide enough to easily accommodate the fundamental telecom mode. Ring designs with $TE_{00}/TE_{00}/TM_{02}$ modes could provide higher values of β, but achieving quasi-phase matching with these modes requires substantially narrower rings with poor confinement of the telecom mode. Conversely, $TE_{00}/TE_{00}/TM_{04}$ allows for wider ring resonators at the cost of severe degradation of the nonlinear overlap. A second ring design, shown in Fig. 4.4, was developed using a $TE_{00}/TE_{01}/TM_{04}$ telecom/pump/visible mode combination, which produced a higher nonlinear overlap $|\beta|^2 = 68\,\mathrm{J}^{-1}$ with a ring width of 810 nm and radius of 4425 nm. However, due to poor coupling and reduced quality factor of the pump mode, devices fabricated with the second design exhibited substantially lower conversion efficiency, as shown in Fig. 4.5.

4.1.7 Supercontinuum pump survey of all devices

In order to compensate for variations in the fabrication process, arrays of devices of both ring designs were fabricated with varying ring widths and coupling region parameters. The supercontinuum-pumped SFG method described in the main paper was used to identify candidate devices for more detailed frequency conversion testing. First, a survey of peak SFG intensity at room temperature was performed on all operational ring resonators of both designs, shown in Fig. 4.5. Because the brightest observed devices of the second design produced roughly 10% of the SFG intensity of the first design rings, subsequent testing was focused on the first design. The supercontinuum-pumped SFG survey was repeated for the design 1 devices at temperatures from $16 - 40°\mathrm{C}$ to identify devices with the strong temperature dependence indicating a triply-resonant conversion process. Eight devices with bright, temperature-sensitive SFG were selected for additional testing. Supercontinuum-pumped SFG was measured at 0.5°C intervals to find the optimal temperature and corresponding peak SFG intensity for each of these devices, as shown in Fig. 4.6.

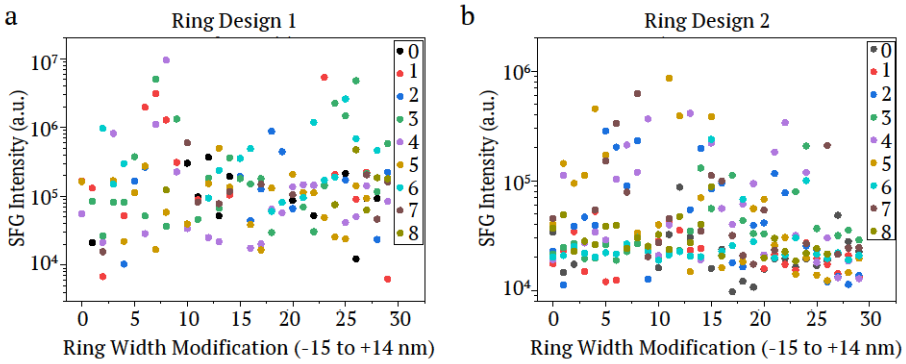

Ring 1	Tele.	9.0×10⁴	1.2×10⁵	1.7×10⁵
Visible	NIR	1.0×10⁵	2.0×10⁵	6.5×10⁵
2.0×10⁴		0	3	6
5.6×10⁴		1	4	7
1.1×10⁵		2	5	8

Ring 2	Tele.	1.2×10⁵	2.2×10⁵	3.5×10⁵
Visible	NIR	2.2×10⁵	4.0×10⁵	7.3×10⁵
2.2×10⁴		0	3	6
5.2×10⁴		1	4	7
9.2×10⁴		2	5	8

Figure 4.5: Supercontinuum-pumped SFG performance survey showing peak SFG intensity at 24°C for all devices of ring designs 1 (a) and 2 (b). All devices were excited with similar input powers, so the measured SFG intensities approximately correspond to conversion efficiencies relative to other devices. While most of the devices are not at their optimal temperatures for SFG, particularly bright devices are likely to be within temperature tuning range ($14 - 40$°C) of triple resonance. Data points are colored according to the simulated coupling quality factors for each device, which are summarized for each ring design in the tables below.

The two devices that exhibited the highest peak SFG intensity, designated SFG01 and SFG02, were selected for calibrated conversion efficiency testing. The SFG testing methods and performance for SFG01 are described in the main text. As shown in Fig. 4.7, device SHG02 was characterized using similar procedures, which found a small-signal power conversion efficiency of $370 - 580\%$/W. Similar to device SFG01, the uncertainty in each measurement is dominated by grating coupler efficiencies, which were measured as $19 \pm 0.5\%$, $7.2 \pm 0.08\%$, and $1.9 \pm 0.15\%$ for telecom, pump, and visible wavelengths. Consequently, the each measured conversion efficiency for SFG02 may be between 10.7% less to 12.7% greater than the nominal value. Due to mode splitting in this device, converted light was observed coupling out of both visible-band grating couplers. The conversion efficiency was calculated from the output power of a single grating coupler.

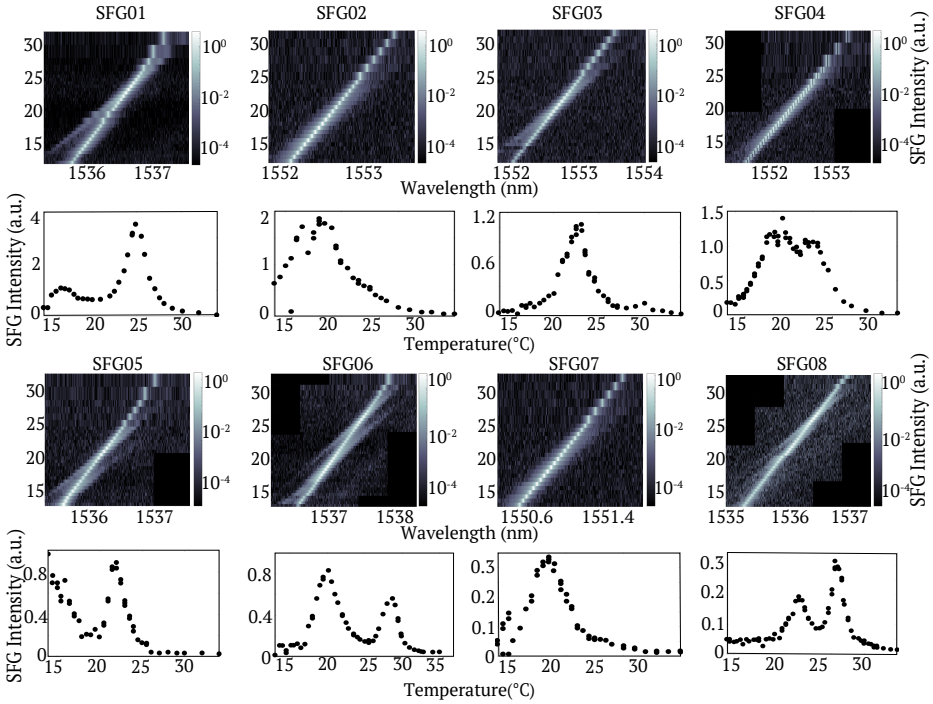

Figure 4.6: Temperature dependence of supercontinuum-pump SFG intensity for devices SFG01-SFG08 (a-h). For each device, a logarithmic-scale color plot shows the SFG dependence on both temperature and telecom-band input wavelength. Every pump-band mode is always resonantly excited by some part of the filtered supercontinuum laser input (1000-1200 nm). The primary intensity line follows the telecom-band resonance, while dimmer lines associated with visible-band resonances tune across the telecom resonance to produce peaks in the SFG conversion efficiency. A linear-scale plot of the peak SFG intensity at each temperature is also shown for each device.

For both devices, power conversion efficiency is calculated as $\eta = P_{\text{out}}/P_{\text{in}}$, where P_{out} is the visible SFG power in the output waveguide and P_{in} is either the telecom or NIR power in the input waveguide, depending which wavelength is designated as the pump in each measurement. In either case, the small-signal conversion efficiency $\eta_{\text{ss}} = P_{\text{vis}}/P_{\text{telecom}}P_{\text{NIR}}$ is the slope of the power dependence of η at low input powers. Photon conversion efficiency is power conversion efficiency scaled by the ratio of input and output photon energies. For each wavelength, power in the waveguide is calculated from off-chip power measurements combined with the grating coupler efficiencies for the device under test. For the telecom and NIR band inputs, the input transmission efficiencies from the point of measurement to

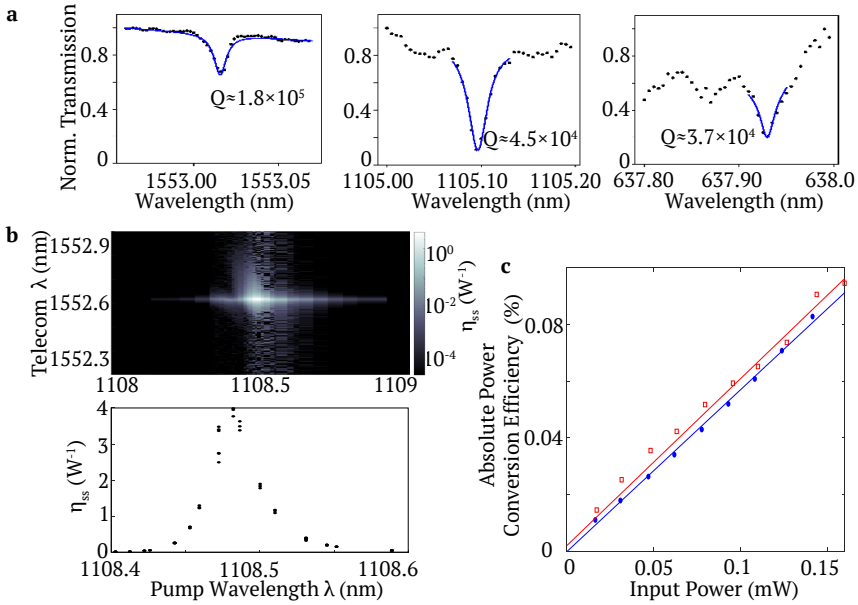

Figure 4.7: (a) Transmission measurements of the telecom, near-infrared, and visible resonances in device SFG02, along with fitted Lorentzian curves and quality factors. Background is approximated with linear function. (b) Supercontinuum-pumped SFG intensity as a function of temperature. (c) Power conversion efficiency of device SFG02 as a function of telecom (blue) and NIR (red) input power. For each data series, the other wavelength input is constant and weak relative to the variable input power.

the grating coupler were 56.5% and 77.2%, respectively. The total collection and detection efficiency of the visible-band output at 647 nm was 2.4%.

4.1.8 Highest quality factors measured in GaP-on-insulator devices

The GaP-on-insulator platform has the potential for significantly higher performance if higher Q-factors can be obtained. The Q-factors in the highest performing SFG devices in this study are lower that what has been obtained in other devices. We have observed telecom Q's as high as 290, 000 on the SFG chip (Fig. SI.5a). We have measured visible Q's ranging from 200,000-490,000 in 290-nm thick GaP disk resonators on nitride (Fig. SI.5b,c). These quality factors are all measured in the undercoupled regime. At critical coupling, Q's may reduce by up to a factor of two. For the visible transmission measurements, an add-drop port geometry is utilized with the drop port monitored.

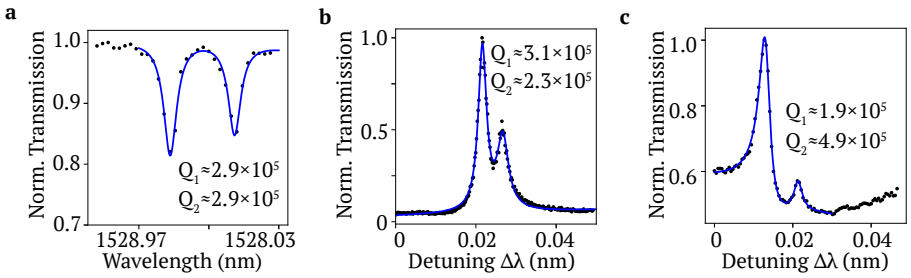

Figure 4.8: (a) Transmission measurements of the telecom resonances in a SFG device, along with fitted Lorentzian curves and quality factors. Background is approximated with linear function. (b–c) Drop port transmission measurements of TM-mode visible resonances in a 5-µm diameter GaP disk resonator on silicon nitride, obtained by scanning a tunable laser. The positions of each resonance are determined to be (b) 768.38 ± 0.16 nm and (c) 635.05 ± 0.11 nm respectively, with Lorentzian fits giving quality factors as large as half million. Here both resonances are in the undercoupled regime demonstrating the large intrinsic quality factor in the visible band. The PL lineshape is fitted using a Fano and a Lorentzian function.

4.2 Generation 1

The first generation of DFG ring resonators were designed for 427 nm thick GaP and fabricated on the same chip as the generation 1 SHG devices. Two ring designs were included in this generation, both intended for quasi-phase matched DFG from a visible input at the NV center zero-phonon line (ZPL) at 637 nm to an output in the telecom C band at 1550 nm, with a ~ 1081.4 nm pump. The first design (DFG1.1) used a single ring with a radius of 6.9 µm measured to the inner edge of the ring. The waveguide width was varied from 839-847 nm over an array of 50 devices to achieve QPM with $\mathrm{TE}_{0,0}$ telecom and pump modes and a TM0, 3 visible mode with a simulated nonlinear overlap of $|\beta|^2 = 28\,J^{-1}$. Separate wrapped-waveguide coupling regions with grating couplers were designed for each mode, with target coupling quality factors of $Q_c = 2 \times 10^5$ for the telecom and pump modes and 2×10^4 for the visible mode.

The second design (DFG1.2) was a concentric double ring resonator, which was intended to improve β by allowing more independent control over the mode profile at each wavelength. The inner ring had a radius of 4 µm to the inner edge and a waveguide width that varied

from 328-332 nm over an array of 90 devices. The 115 nm wide outer ring was separated from the inner ring by a 75 nm gap. The double ring structure allowed the TE00 telecom and pump modes to be quasi-phase matched with a TM02 visible mode, resulting in a much higher mode overlap of $|\beta|^2 = 108.2\,J^{-1}$. Similar coupling regions were designed for the double ring, but because the pump mode was mostly confined to the inner ring, the simulated coupling Q for this mode could not be reduced below 4×10^5.

Testing for both generation 1 DFG ring designs was suspended because no coupled resonances could be identified by transmission measurements in the telecom band. The single design had similar dimensions to other functional ring resonators, including the SHG rings fabricated on the same chip, so lack of measurable resonances is likely due to severe over- or undercoupling. The resulting shallow transmission dips could be obfuscated by the strong Fabry-Perot interference pattern in the transmission spectrum, which is caused by grating coupler back reflections. The same mechanism could apply to the double ring design, compounded by the possibility of extreme degradation of the intrinsic quality factor due to the telecom mode's concentration in the gap between the rings.

4.3 Generation 2

A second generation of ring resonators was designed for a 250 thick GaP membrane. In addition to reducing mode volume and therefore increasing β, the thinner material was intended to eliminate vertically-split higher-order modes at the shorter process wavelengths. This would facilitate mode identification by reducing the overall number of ring modes.

The second DFG generation was designed for a 250 nm thick GaP membrane, with a total of four single-ring resonator designs fabricated on a single chip. Similar to the generation 1 devices, all of the rings had each mode evanescently coupled to a separate wrapped waveguide. To increase the chances of finding near-critically coupled rings and hedge against fabrication variations, each ring design was fabricated with multiple coupling region specifications. Target coupling quality factors of 5×10^4, 1×10^5, and 2×10^5 were used for fundamental modes with high expected intrinsic quality factors (all telecom and most pump modes), with higher-order modes (all visible and one pump mode) were designed for coupling quality factors of 2×10^4, 5×10^4, or 1×10^5. For each ring and coupling specification,

an array of 40 devices with varying ring waveguide width was fabricated. Similar to SHG generation 2, elliptical focusing grating couplers were used to suppress the back reflections that caused the Fabry-Perot interference pattern in the transmission spectra.

The first ring (DFG2.1) was designed with an inner radius of 4.5 µm and width of 630 nm, similar to the generation 2 SHG design that had already been successfully tested. Due to the thinner GaP and somewhat smaller radius, this design had a nonlinear overlap $|\beta|^2$ of $80.5\,\mathrm{J}^{-1}$, close to three times higher than the first-generation single ring design. Ring radius was minimized in the second and third ring designs (DFG2.2 and DFG2.3) with the positive and negative quasi phase matching conditions, respectively. This produced a ring with an inner radius of 3 µm and width of 550 nm for the positive condition, and r = 2.5 µm and w = 740 nm for the negative. The further reduction in ring radius did not significantly increase the nonlinear mode overlap compared to design DFG2.1, however.

The final ring design (DFG2.4) was designed to be quasi-phase matched with a $\mathrm{TE}_{0,0}$ telecom mode, $\mathrm{TE}_{0,1}$ pump mode, and $\mathrm{TM}_{0,4}$ visible mode, instead of the (TE00, TE00, TM03) combination used in all previous single-ring designs. The higher-order modes nearly tripled $|\beta|^2$ compared to the other designs in this generation, though any efficiency gains may be offset by a reduction in pump mode intrinsic quality factor. Also, using different modes for all three wavelengths could allow better independent tuning, which would be vital for quantum information applications.

Testing of the generation 2 devices was suspended due to unexpectedly strong coupling between the telecom modes and the pump coupling circuits, which greatly degraded the quality factors of observed modes. This coupling was not predicted by eigenmode or FDTD simulations of the coupled rings, so it may have been influenced by fabrication variations. To avoid these unintended coupling paths, future devices were designed with a single coupling region for both the telecom and pump modes.

Chapter 5

OUTLOOK

In this project, gallium phosphide ring resonators on the order of 10 µm in diameter were designed for quasi-phase matched triple-resonant difference frequency conversion from visible red (637 nm) to telecom C-band (1550 nm) wavelengths, as well as double-resonant second harmonic generation from telecom (1550 nm) to near-visible (775 nm). The resonators were fabricated in epitaxial GaP membranes that had been wet-transferred to silicon oxide substrates, using parameter sweep arrays to offset fabrication variations. Devices that could be temperature tuned to QPM multiple resonance were identified out of hundreds of devices on each chip using rapid testing methods based on direct measurements of frequency conversion processes. In a ring resonator with total quality factors in the range of $2.6 - 11 \times 10^4$, triple resonant sum frequency generation was measured with an on-chip, waveguide-to-waveguide small signal power conversion efficiency of 4900-9500%/W and absolute power conversion efficiency of up to 6.3%. This up-conversion power conversion efficiency is equivalent to a photon conversion efficiency of 2100-4000%/W for both the tested SFG and its converse DFG process, which is sufficient for initial testing of single-photon frequency conversion even when limited by low off-chip coupling efficiency. A resonator with similar intrinsic quality factors and critical coupling for all three ring modes could increase the photon conversion efficiency to $\sim 7200\%/\mathrm{W}$, while improving the intrinsic quality factors to the highest observed values of $\sim 3 \times 10^5$ for infrared modes and $\sim 2 \times 10^5$ for visible could provide up to $\sim 45,000\%/\mathrm{W}$. Based on the measured and projected performance, multi-resonant GaP structures are a promising platform for low-power, scalable frequency conversion for applications such as entanglement distribution for large-scale quantum networks using diamond NV centers or other solid-state quantum emitters.

Additional testing is required to fully evaluate the potential of GaP nonlinear resonators, especially for single-photon frequency conversion applications. For example, because 637 nm

to telecom conversion requires a pump at a shorter wavelength than the output, telecom noise photons can potentially be generated by spontaneous down conversion. While this is a known issue in PPLN waveguides [49], resonant devices may help suppress undesired frequency conversion processes by a combination of phase matching and resonance. Other performance tests would include Hong-Ou-Mandel interference measurements to confirm the indistinguishability of converted photons, as well as explorations of the specific mechanisms that limit conversion efficiency in GaP resonators. Practical applications of these resonators will require further development of designs and processes, as well. Optimal waveguide-resonator coupling, efficient off-chip coupling, and full integration with device heaters, photodetectors, and control electronics, while theoretically straightforward, pose substantial engineering challenges that must be addressed for scalable quantum communication network applications. Perhaps the most critical challenge, however, will be achieving triple resonance from a precise defect optical transition frequency to a precise target telecom frequency despite fabrication variations and post-fabrication drift. This will require advancement and consistent implementation of multiple independent resonator tuning mechanisms, such as precisely controlled etching, modifiable cladding layers, or coupled auxiliary resonators with independent heating [67, 44]. Once achieved, the impact of triply-resonant devices would extend to wavelength multiplexing for quantum networks and the elimination of emitter wavelength inhomogeneity.

Appendix A

CODE

A.1 Nonlinear Ring Resonator Design

https://github.com/adlogan56/nonlinear-ring-resonator

A.2 Aperiodic Grating Coupler Optimization

https://github.com/adlogan56/grating-coupler-opt

A.3 Photonics Chip Layout

https://github.com/adlogan56/photonics-klayout

Appendix B

FABRICATION DETAILS

B.1 Generation 1

B.1.1 Membrane Etch

—Process start with 427 nm GaP (HU1-2101)

—Sonicate in acetone for 4 minutes, and soak for 1 more

—Soak in IPA for 5 minutes

—Water rinse and N2 blow dry

—Bake for 5 minutes above 50C.

—Spin AZ1512:

-—2s ramp to 500 for 5s

-—3s ramp to 5500 for 40s

—Softbake 1 minute 110C

—Expose membrane pattern with ABM aligner:

-—Full piece, 3 mm membrane with 250 µm etch via spacing

-—Exposed 4s

—Develop 60 seconds in 1:4 AZ340:H2O

—DI Rinse

—N2 Blow dry

—Examine with Nikon optical microscope:

— 17 full 3-mm membranes, 2 partial (more than 50

—BarrelEtch O2 plasma asher, 75 W, 120s

—Cleave off single membrane for etching

—AlphaStep profilometer:

— Resist etch vias show >1.1 µm

—ICP-RIE:

—Use recipe MAG GaP Membrane Etch

——— 4 mTorr (3 initially), 1.0 sccm Cl, 7.5 sccm N2, 100W ICP power, 50W RF power (70 initially)

—12:00 on dummy (307 V)

—Turn RF power from 70 down to 60

—2:00 on dummy (282 V)

—Turn RF power to 50, and increase pressure to 4.0 mTorr

—2:00 on dummy (268 V)

—2 x 40s on membrane (272 V/ 265 V)

—AlphaStep: membrane etch vias show 2.2µm

B.1.2 Membrane Transfer

—Thermal oxide wafer in piranha bath for 15 minutes:

—Full cascade rinse (5 minutes in each pocket)

—Barrel etch thermal oxide wafer:

—190 W, 5 minutes

—HMDS thermal oxide wafer

—Membrane into 3:100 HF:H20:

—Raised to surface after 30 min, not ready...

—Try again at 1 hr, had completely rolled up, but got it to surface more or less intact

—Tranferred membrane onto thermal oxide chip:

—Complete membrane transferred by catching membrane in water droplet and dehydrating on hotplate (80C)

—Membrane is definitely folded up, may be inherent to water droplet method

— Chip onto hotplate at 80C at overnight

B.1.3 Electron Beam Lithography

—Nikon optical microscope examination of membrane

—Clearly compressed during transfer (droplet drying not ideal)

—Large areas of apparently usable material

—Removed photoresist:

—15 minutes in EKC at 80C, agitating once every 5 minutes

—5 minutes in acetone

—Dunk in IPA

—N2 blow dry

—Nikon examination of membrane

—Chip looks clean

—Evaporation deposition of 3 nm SiO2 on chip (EVAP 1)

—N2 blow to remove any dust

—Barrel etch (50 W, 2 minutes)

—5 minutes on hotplate at 150C.

—Spin HSQ 6%:
—Try to center membrane on spindle
—1s ramp to 500 rpm for 1s dwell
—1s ramp to 6000 rpm for 45s dwell

—Softbake 80 C, 4 minutes

—Nikon optical microscope examination
—Coat slightly uneven due to uneven membranes
—Good enough to proceed

—Overnight e-beam write with chip pattern file

—Develop:
—4 minutes in 25% TMAH
—1 minute in DI rinse, with a bit of agitation (move the chip around)
—N2 blow dry

—Exmaination with Nikon and SEM
—So-so yield but many promising devices

—N2 GaP Etch: 4.0 mTorr, 2.0 Torr He press., 1.0/6.0/3.0 sccm Cl/Ar/N2; ICP power 60; RF power 40; Table temp 21 (chiller at 20):

—20 minutes on dummy (238 V; 2.6 sccm He)

—Mount GaP-on-oxide Chip with Fomblin oil

—60s (240 V; 2.7 sccm He)

—Membrane still clearly visible in load lock

—30s (240 V; 2.7 sccm He)

—20s (240 V; 2.7 sccm He)

—Etch examined with Nikon and SEM

B.2 Generation 3

B.2.1 Membrane Etch

—Process start with 427 nm GaP (HU1-2101)

—Sonicate in acetone for 4 minutes, and soak for 1 more

—Soak in IPA for 5 minutes

—Water rinse and N2 blow dry

—Bake for 5 minutes above 50C.

—Spin AZ1512:

-—2s ramp to 500 for 5s

-—3s ramp to 5500 for 40s

—Softbake 1 minute 110C

—Expose membrane pattern with ABM aligner:

-—Full piece, 3 mm membrane with 250 µm etch via spacing

-—Exposed 4s

—Develop 60 seconds in 1:4 AZ340:H2O

—DI Rinse

—N2 Blow dry

—Cleave off single membrane for etching

—AlphaStep profilometer:

— Resist etch vias show >1.1µm

—ICP-RIE:

—Use recipe: 4 mTorr with 5s strike step at 5 mTorr, 1.0 sccm Cl, 7.5 sccm N2, 100W ICP power, 40W RF power

—15:00 on dummy (248 V)

—Turn RF power from 40W to 38W

—2:00 on dummy (282 V)

—3 x 40s on membrane (238 V)

—AlphaStep: membrane etch vias show 2.5µm

B.2.2 Membrane Transfer

—Oxide chip cleaved, then rinsed with acetone, then IPA, and N2 dried

—Oxide chip in BarrelEtch O2 asher, 150W, 5 min

— Membrane in 6:100 49% HF : DI water

— Oxide chip HMDS treatment started

— After 120 min, membrane appears uneven. Lifted near fluid surface with tweezers, but failed to lift off

— Lifted off at 150 min. Membrane rolled into a taco shape and sank to bottom of solution.

— Membrane lifted into middle of HF solution by agitating nearby solution with tweezers. Membrane captured with teflon scoop and transferred to DI water.

— Membrane still rolled up, but near surface of DI water. Transferred by teflon scoop to second container of DI water.

— Membrane guided onto oxide membrane with aluminum bucket/funnel. Membrane unrolled on contact with oxide surface and lays flat.

— Water allowed to drain by capillary channels. Once the membrane is flat on the oxide surface, excess fluid is absorbed with lab wipes.

— GaP/oxide chip blown dry with N2 and dehydrated using microscope illumination.

— Chip on hotplate at 80C overnight, protected by an upside-down beaker

B.2.3 Electron Beam Lithography

—Removed photoresist:

—15 minutes in EKC at 80C, agitating once every 5 minutes

—5 minutes in acetone

—Rinse with IPA

—N2 blow dry

— BarrelEtch O2 plasma asher: 100W for 4 min

— Chip on hotplate at 80C overnight

— PECVD oxide deposition: 6 nm, low deposition rate (1.2 nm/s) at 125C

— HSQ Spin-on:

—5 minutes on hotplate at 150C.

—Spin HSQ 6%:

—Try to center membrane on spindle

—1s ramp to 500 rpm for 1s dwell

—1s ramp to 6000 rpm for 45s dwell

—3s ramp to 0 rpm, hold for 1s

—Softbake on hotplate at 80 C, 4 minutes

— Ebeam write with chip pattern file

—Develop:

—4 minutes in 25% TMAH

—1 minute rinse with flowing DI water

—N2 blow dry

— ICP-RIE:

— 10 minute Cl2 chamber clean

—N2 GaP Etch: 4.0 mTorr after 5s strike at 5.0 mTorr, 1.0/6.0/3.0 sccm Cl/Ar/N2; ICP power 60W; RF power 40W

—20 minutes on silicon dummy (240 V)

—Mount GaP-on-oxide Chip with Fomblin oil

—2x30s on Chip (238 V)

—Membrane still visible in load lock, but color (thickness) is changing

—3x30s on Chip (240 V)

—Full membrane no longer visible in load lock. Pattern clearly discernable

—30s on Chip (240 V), to ensure complete membrane etch

— Confirm full membrane etch with optical microscope and SEM

BIBLIOGRAPHY

[1] Marius A Albota and Franco NC Wong. Efficient single-photon counting at 1.55 μm by means of frequency upconversion. *Optics Letters*, 29(13):1449–1451, 2004.

[2] Markus Allgaier, Vahid Ansari, Linda Sansoni, Christof Eigner, Viktor Quiring, Raimund Ricken, Georg Harder, Benjamin Brecht, and Christine Silberhorn. Highly efficient frequency conversion with bandwidth compression of quantum light. *Nature Communications*, 8(1):14288, Jan 2017.

[3] Vilson R. Almeida and Michal Lipson. Optical bistability on a silicon chip. *Opt. Lett.*, 29(20):2387–2389, Oct 2004.

[4] Serkan Ates, Imad Agha, Angelo Gulinatti, Ivan Rech, Matthew T Rakher, Antonio Badolato, and Kartik Srinivasan. Two-photon interference using background-free quantum frequency conversion of single photons emitted by an inas quantum dot. *Physical Review Letters*, 109(14):147405, 2012.

[5] Paul E. Barclay, Kai-Mei Fu, Charles Santori, and Raymond G. Beausoleil. Hybrid photonic crystal cavity and waveguide for coupling to diamond nv-centers. *Opt. Express*, 17(12):9588–9601, Jun 2009.

[6] S.C. Benjamin, B.W. Lovett, and J.M. Smith. Prospects for measurement-based quantum computing with solid state spins. *Laser & Photonics Reviews*, 3(6):556–574, 2009.

[7] H. Bernien, B. Hensen, W. Pfaff, G. Koolstra, M. S. Blok, L. Robledo, T. H. Taminiau, M. Markham, D. J. Twitchen, L. Childress, and R. Hanson. Heralded entanglement between solid-state qubits separated by three metres. *Nature*, 497(7447):86–90, May 2013.

[8] Eric Bersin, Noel Wan, Mihir Bhaskar, David Levonian, Ralf Riedinger, Carsten Langrock, M. M. Fejer, Mikhail Lukin, P. Ben Dixon, Scott Hamilton, and Dirk Englund. A low-noise telecom interface for silicon-vacancy quantum network nodes. In *2021 Conference on Lasers and Electro-Optics (CLEO)*, pages 1–2, 2021.

[9] Zhuan-Fang Bi, Alejandro W Rodriguez, Hila Hashemi, David Duchesne, Marko Loncar, Ke-Ming Wang, and Steven G Johnson. High-efficiency second-harmonic generation in doubly-resonant χ (2) microring resonators. *Optics express*, 20(7):7526–7543, 2012.

[10] Alberto Boaron, Gianluca Boso, Davide Rusca, Cédric Vulliez, Claire Autebert, Misael Caloz, Matthieu Perrenoud, Gaëtan Gras, Félix Bussières, Ming-Jun Li, Daniel Nolan, Anthony Martin, and Hugo Zbinden. Secure quantum key distribution over 421 km of optical fiber. *Phys. Rev. Lett.*, 121:190502, Nov 2018.

[11] Matthias Bock, Pascal Eich, Stephan Kucera, Matthias Kreis, Andreas Lenhard, Christoph Becher, and Jürgen Eschner. High-fidelity entanglement between a trapped ion and a telecom photon via quantum frequency conversion. *Nature Communications*, 9(1):1–7, 2018.

[12] W. L. Bond. Measurement of the refractive indices of several crystals. *Journal of Applied Physics*, 36(5):1674–1677, 1965.

[13] Robert Boyd. *Nonlinear Optics*. Academic Press, 2008.

[14] Jorge Bravo-Abad, Alejandro Rodriguez, Peter Bermel, John D. Johnson, Steven G. a nd Joannopoulos, and Marin Soljacic. Enhanced nonlinear optics in photonic-crystal microcavities. *Optics Express*, 15(24):16161–16176, 2007.

[15] Sonia Buckley, Marina Radulaski, Jan Petykiewicz, Konstantinos G. Lagoudakis, Ju-Hyung Kang, Mark Brongersma, Klaus Biermann, and Jelena Vućković. Second-harmonic generation in gaas photonic crystal cavities in (111)b and (001) crystal orientations. *ACS Photonics*, 1(6):516–523, 2014.

[16] Ian B Burgess, Alejandro W Rodriguez, Murray W McCutcheon, Jorge Bravo-Abad, Yinan Zhang, Steven G Johnson, and Marko Lončar. Difference-frequency generation with quantum-limited efficiency in triply-resonant nonlinear cavities. *Optics Express*, 17(11):9241–9251, 2009.

[17] Jia-Yang Chen, Yong Meng Sua, Heng Fan, and Yu-Ping Huang. Modal phase matched lithium niobate nanocircuits for integrated nonlinear photonics. *OSA Continuum*, 1(1):229–242, 2018.

[18] Andrea Dal Corso, Francesco Mauri, and Angel Rubio. Density-functional theory of the nonlinear optical susceptibility: Application to cubic semiconductors. *Phys. Rev. B*, 53:15638–15642, Jun 1996.

[19] Anaïs Dréau, Anna Tchebotareva, Aboubakr El Mahdaoui, Cristian Bonato, and Ronald Hanson. Quantum frequency conversion of single photons from a nitrogen-vacancy center in diamond to telecommunication wavelengths. *Physical Review Applied*, 9(6):064031, 2018.

[20] Y. Dumeige and P. Féron. Whispering-gallery-mode analysis of phase-matched doubly resonant second-harmonic generation. *Phys. Rev. A*, 74:063804, Dec 2006.

[21] Dirk Englund, Brendan Shields, Kelley Rivoire, Fariba Hatami, Jelena Vućković, Hongkun Park, and Mikhail D. Lukin. Deterministic coupling of a single nitrogen vacancy center to a photonic crystal cavity. *Nano Letters*, 10(10):3922–3926, 2010.

[22] J. U. Furst, D. V. Strekalov, D. Elser, M. Lassen, U. L. Andersen, C. Marquadt, and G. Leuchs. Naturally phase-matched second-harmonic generation in a whispering-gallery-mode resonator. *Physical Review Letters*, 104:153901, 2010.

[23] Michael Gould, Srivatsa Chakravarthi, Ian R. Christen, Nicole Thomas, Shabnam Dadgostar, Yuncheng Song, Minjoo Larry Lee, Fariba Hatami, and Kai-Mei C. Fu. Large-scale gap-on-diamond integrated photonics platform for nv center-based quantum information. *J. Opt. Soc. Am. B*, 33(3):B35–B42, Mar 2016.

[24] Michael Gould, Emma R. Schmidgall, Shabnam Dadgostar, Fariba Hatami, and Kai-Mei C. Fu. Efficient extraction of zero-phonon-line photons from single nitrogen-vacancy centers in an integrated gap-on-diamond platform. *Phys. Rev. Applied*, 6:011001, Jul 2016.

[25] Thiago Guerreiro, Enrico Pomarico, Bruno Sanguinetti, Nicolas Sangouard, JS Pelc, C Langrock, MM Fejer, Hugo Zbinden, Robert T Thew, and Nicolas Gisin. Interaction of independent single photons based on integrated nonlinear optics. *Nature Communications*, 4(1):1–5, 2013.

[26] Xiang Guo, Chang-Ling Zou, Hojoong Jung, and Hong X. Tang. On-chip strong coupling and efficient frequency conversion between telecom and visible optical modes. *Phys. Rev. Lett.*, 117:123902, Sep 2016.

[27] Xiang Guo, Chang-Ling Zou, and Hong X. Tang. Second-harmonic generation in aluminum nitride microrings with 2500%/W conversion efficiency. *Optica*, 3(10):1126–1131, Oct 2016.

[28] S. M. Hendrickson, A. C. Foster, R. M. Camacho, and B. D. Clader. Integrated nonlinear photonics: emerging applications and ongoing challenges. *J. Opt. Soc. Am. B*, 31(12):3193–3203, Dec 2014.

[29] Ding Huang, Alex Abulnaga, Sacha Welinski, Mouktik Raha, Jeff D. Thompson, and Nathalie P. de Leon. Hybrid III-V diamond photonic platform for quantum nodes based on neutral silicon vacancy centers in diamond. *Opt. Express*, 29(6):9174–9189, Mar 2021.

[30] Peter C. Humphreys, Norbert Kalb, Jaco P. J. Morits, Raymond N. Schouten, Raymond F. L. Vermeulen, Daniel J. Twitchen, Matthew Markham, and Ronald Hanson. Deterministic delivery of remote entanglement on a quantum network. *Nature*, 558(7709):268–273, Jun 2018.

[31] Rikizo Ikuta, Toshiki Kobayashi, Shuto Yasui, Shigehito Miki, Taro Yamashita, Hirotaka Terai, Mikio Fujiwara, Takashi Yamamoto, Masato Koashi, Masahide Sasaki, Zhen Wang, and Nobuyuki Imoto. Frequency down-conversion of 637 nm light to the telecommunication band for non-classical light emitted from nv centers in diamond. *Optics Express*, 22(9):11205–11214, 2014.

[32] Weiliang Jin, Sean Molesky, Zin Lin, Kai-Mei C. Fu, and Alejandro W. Rodriguez. Inverse design of compact multimode cavity couplers. *Opt. Express*, 26(20):26713–26721, Oct 2018.

[33] Prem Kumar. Quantum frequency conversion. *Opt. Lett.*, 15(24):1476–1478, Dec 1990.

[34] Paulina S. Kuo, Jorge Bravo-Abad, and Glenn S. Solomon. Second-harmonic generation using -quasi-phasematching in a GaAs whispering-gallery-mode microcavity. *Nature Communications*, 5:3109 EP –, 01 2014.

[35] David P. Lake, Matthew Mitchell, Harishankar Jayakumar, LaÃs Fujii dos Santos, Davor Curic, and Paul E. Barclay. Efficient telecom to visible wavelength conversion in doubly resonant gallium phosphide microdisks. *Applied Physics Letters*, 108(3):031109, 2016.

[36] D. S. Levonian, R. Riedinger, B. Machielse, E. N. Knall, M. K. Bhaskar, C. M. Knaut, R. Bekenstein, H. Park, M. Lončar, and M. D. Lukin. Optical entanglement of distinguishable quantum emitters. *Phys. Rev. Lett.*, 128:213602, May 2022.

[37] Sheng-Kai Liao, Wen-Qi Cai, Wei-Yue Liu, Liang Zhang, Yang Li, Ji-Gang Ren, Juan Yin, Qi Shen, Yuan Cao, Zheng-Ping Li, Feng-Zhi Li, Xia-Wei Chen, Li-Hua Sun, Jian-Jun Jia, Jin-Cai Wu, Xiao-Jun Jiang, Jian-Feng Wang, Yong-Mei Huang, Qiang Wang, Yi-Lin Zhou, Lei Deng, Tao Xi, Lu Ma, Tai Hu, Qiang Zhang, Yu-Ao Chen, Nai-Le Liu, Xiang-Bin Wang, Zhen-Cai Zhu, Chao-Yang Lu, Rong Shu, Cheng-Zhi Peng, Jian-Yu Wang, and Jian-Wei Pan. Satellite-to-ground quantum key distribution. *Nature*, 549(7670):43–47, Sep 2017.

[38] Guoping Lin, Aurélien Coillet, and Yanne K Chembo. Nonlinear photonics with high-Q whispering-gallery-mode resonators. *Advances in Optics and Photonics*, 9(4):828–890, 2017.

[39] Zin Lin, Xiangdong Liang, Marko Lončar, Steven G. Johnson, and Alejandro W. Rodriguez. Cavity-enhanced second-harmonic generation via nonlinear-overlap optimization. *Optica*, 3(3):233–238, Mar 2016.

[40] Brent E. Little, Juha-Pekka Laine, and Sai T. Chu. Surface-roughness-induced contradirectional coupling in ring and disk resonators. *Opt. Lett.*, 22(1):4–6, Jan 1997.

[41] Alan D. Logan, Michael Gould, Emma R. Schmidgall, Karine Hestroffer, Zin Lin, Weiliang Jin, Arka Majumdar, Fariba Hatami, Alejandro W. Rodriguez, and Kai-Mei C. Fu. 400%/W second harmonic conversion efficiency in 14 µm-diameter gallium phosphide-on-oxide resonators. *Opt. Express*, 26(26):33687–33699, Dec 2018.

[42] Alan D. Logan, Shivangi Shree, Srivatsa Chakravarthi, Nicholas Yama, Christian Pederson, Karine Hestroffer, Fariba Hatami, and Kai-Mei C. Fu. Triply-resonant sum frequency conversion with gallium phosphide ring resonators, 2022.

[43] Juanjuan Lu, Joshua B. Surya, Xianwen Liu, Alexander W. Bruch, Zheng Gong, Yuntao Xu, and Hong X. Tang. Periodically poled thin-film lithium niobate microring resonators with a second-harmonic generation efficiency of 250,000%/w. *Optica*, 6(12):1455–1460, Dec 2019.

[44] Xiyuan Lu, Ashutosh Rao, Gregory Moille, Daron A. Westly, and Kartik Srinivasan. Universal frequency engineering tool for microcavity nonlinear optics: multiple selective mode splitting of whispering-gallery resonances. *Photon. Res.*, 8(11):1676–1686, Nov 2020.

[45] Nicolas Maring, Dario Lago-Rivera, Andreas Lenhard, Georg Heinze, and Hugues de Riedmatten. Quantum frequency conversion of memory-compatible single photons from 606 nm to the telecom c-band. *Optica*, 5(5):507–513, May 2018.

[46] A. Martin, S. Combrié, A. de Rossi, G. Beaudoin, I. Sagnes, and F. Raineri. Nonlinear gallium phosphide nanoscale photonics. *Photon. Res.*, 6(5):B43–B49, May 2018.

[47] Mohamed Sabry Mohamed, Angelica Simbula, Jean-François Carlin, Momchil Minkov, Dario Gerace, Vincenzo Savona, Nicolas Grandjean, Matteo Galli, and Romuald Houdré. Efficient continuous-wave nonlinear frequency conversion in high-Q gallium nitride photonic crystal cavities on silicon. *APL Photonics*, 2(3):031301, 2017.

[48] Gregory Moille, Sylvain Combrié, Laurence Morgenroth, Gaëlle Lehoucq, Sébastien Sauvage, Moustafa El Kurdi, Philippe Boucaud, Alfredo de Rossi, and Xavier Checoury. Nonlinearities in gaas cavities with high cw input powers enabled by photo-oxidation quenching through ald encapsulation. *Opt. Express*, 26(5):6400–6406, Mar 2018.

[49] Christopher L. Morrison, Markus Rambach, Zhe Xian Koong, Francesco Graffitti, Fiona Thorburn, Ajoy K. Kar, Yong Ma, Suk-In Park, Jin Dong Song, Nick G. Stoltz, Dirk Bouwmeester, Alessandro Fedrizzi, and Brian D. Gerardot. A bright source of telecom single photons based on quantum frequency conversion. *Applied Physics Letters*, 118(17):174003, 2021.

[50] J. Pastrňák and L. Roskovcová. Refraction index measurements on AlN single crystals. *physica status solidi (b)*, 14(1):K5–K8.

[51] J. S. Pelc, L. Ma, C. R. Phillips, Q. Zhang, C. Langrock, O. Slattery, X. Tang, and M. M. Fejer. Long-wavelength-pumped upconversion single-photon detector at 1550 nm: performance and noise analysis. *Opt. Express*, 19(22):21445–21456, Oct 2011.

[52] M. Pompili, S. L. N. Hermans, S. Baier, H. K. C. Beukers, P. C. Humphreys, R. N. Schouten, R. F. L. Vermeulen, M. J. Tiggelman, L. dos Santos Martins, B. Dirkse, S. Wehner, and R. Hanson. Realization of a multinode quantum network of remote solid-state qubits. *Science*, 372(6539):259–264, 2021.

[53] Ashutosh Rao and Sasan Fathpour. Second-harmonic generation in integrated photonics on silicon. *physica status solidi (a)*, 215(4):1700684, 2017.

[54] Kelley Rivoire, Sonia Buckley, Fariba Hatami, and Jelena Vućković. Second harmonic generation in gap photonic crystal waveguides. *Applied Physics Letters*, 98(26):263113, 2011.

[55] Alejandro Rodriguez, Marin Soljačić, John D Joannopoulos, and Stev en G Johnson. $\chi^{(2)}$ and $\chi^{(3)}$ harmonic generation at a critical power in inhomogeneous doubly resonant cavities. *Optics Express*, 15(12):7303–7318, 2007.

[56] I. Roland, M. Gromovyi, Y. Zeng, M. El Kurdi, S. Sauvage, C. Brimont, T. Guillet, B. Gayral, F. Semond, J. Y. Duboz, M. de Micheli, X. Checoury, and P. Boucaud. Phase-matched second harmonic generation with on-chip GaN-on-Si microdisks. *Scientific Reports*, 6:34191 EP –, 09 2016.

[57] Helge Rütz, Kai-Hong Luo, Hubertus Suche, and Christine Silberhorn. Quantum frequency conversion between infrared and ultraviolet. *Physical Review Applied*, 7(2):024021, 2017.

[58] Aiko Samblowski, Christina E. Vollmer, Christoph Baune, Jaromír Fiurášek, and Roman Schnabel. Weak-signal conversion from 1550 to 532 nm with 84% efficiency. *Opt. Lett.*, 39(10):2979–2981, May 2014.

[59] Nicolas Sangouard, Christoph Simon, Hugues de Riedmatten, and Nicolas Gisin. Quantum repeaters based on atomic ensembles and linear optics. *Rev. Mod. Phys.*, 83:33–80, Mar 2011.

[60] Emma R. Schmidgall, Srivatsa Chakravarthi, Michael Gould, Ian R. Christen, Karine Hestroffer, Fariba Hatami, and Kai-Mei C. Fu. Frequency control of single quantum emitters in integrated photonic circuits. *Nano Letters*, 18(2):1175–1179, 2018.

[61] Katharina Schneider, Pol Welter, Yannick Baumgartner, Herwig Hahn, Lukas Czornomaz, and Paul Seidler. Gallium phosphide-on-silicon dioxide photonic devices. *J. Lightwave Technol.*, 36(14):2994–3002, Jul 2018.

[62] E. Fred Schubert. *Light-Emitting Diodes*. Cambridge University Press, 2 edition, 2006.

[63] Ichiro Shoji, Takashi Kondo, Ayako Kitamoto, Masayuki Shirane, and Ryoichi Ito. Absolute scale of second-order nonlinear-optical coefficients. *J. Opt. Soc. Am. B*, 14(9):2268–2294, Sep 1997.

[64] Chawin Sitawarin, Weiliang Jin, Zin Lin, and Alejandro W Rodriguez. Inverse-designed photonic fibers and metasurfaces for nonlinear frequency conversion. *Photonics Research*, 6(5):B82–B89, 2018.

[65] A.J. Stolk, K.L. van der Enden, M.-C. Roehsner, A. Teepe, S.O.J. Faes, C.E. Bradley, S. Cadot, J. van Rantwijk, I. te Raa, R.A.J. Hagen, A.L. Verlaan, J.J.B. Biemond, A. Khorev, R. Vollmer, M. Markham, A.M. Edmonds, J.P.J. Morits, T.H. Taminiau, E.J. van Zwet, and R. Hanson. Telecom-band quantum interference of frequency-converted photons from remote detuned nv centers. *PRX Quantum*, 3:020359, Jun 2022.

[66] Anna Tchebotareva, Sophie L. N. Hermans, Peter C. Humphreys, Dirk Voigt, Peter J. Harmsma, Lun K. Cheng, Ad L. Verlaan, Niels Dijkhuizen, Wim de Jong, Anaïs Dréau, and Ronald Hanson. Entanglement between a diamond spin qubit and a photonic time-bin qubit at telecom wavelength. *Phys. Rev. Lett.*, 123:063601, Aug 2019.

[67] Lillian Thiel, Alan D. Logan, Srivatsa Chakravarthi, Shivangi Shree, Karine Hestroffer, Fariba Hatami, and Kai-Mei C. Fu. Precise electron beam-based target-wavelength trimming for frequency conversion in integrated photonic resonators. *Opt. Express*, 30(5):6921–6933, Feb 2022.

[68] Nicole Thomas, Russell J. Barbour, Yuncheng Song, Minjoo Larry Lee, and Kai-Mei C. Fu. Waveguide-integrated single-crystalline gap resonantors on diamond. *Optics Express*, 22:13555, 2014.

[69] Tim van Leent, Matthias Bock, Robert Garthoff, Kai Redeker, Wei Zhang, Tobias Bauer, Wenjamin Rosenfeld, Christoph Becher, and Harald Weinfurter. Long-distance distribution of atom-photon entanglement at telecom wavelength. *Physical Review Letters*, 124(1):010510, 2020.

[70] Thomas Walker, Koichiro Miyanishi, Rikizo Ikuta, Hiroki Takahashi, Samir Vartabi Kashanian, Yoshiaki Tsujimoto, Kazuhiro Hayasaka, Takashi Yamamoto, Nobuyuki Imoto, and Matthias Keller. Long-distance single photon transmission from a trapped ion via quantum frequency conversion. *Physical Review Letters*, 120(20):203601, 2018.

[71] Cheng Wang, Michael J. Burek, Zin Lin, Haig A. Atikian, Vivek Venkataraman, I-Chun Huang, Peter Stark, and Marko Lončar. Integrated high quality factor lithium niobate microdisk resonators. *Opt. Express*, 22(25):30924–30933, Dec 2014.

[72] Cheng Wang, Zhaoyi Li, Myoung-Hwan Kim, Xiao Xiong, Xi-Feng Ren, Guang-Can Guo, Nanfang Yu, and Marko Lončar. Metasurface-assisted phase-matching-free second harmonic generation in lithium niobate waveguides. *Nature Communications*, 8(1):2098, 2017.

[73] Jia-Qi Wang, Yuan-Hao Yang, Ming Li, Xin-Xin Hu, Joshua B. Surya, Xin-Biao Xu, Chun-Hua Dong, Guang-Can Guo, Hong X. Tang, and Chang-Ling Zou. Efficient frequency conversion in a degenerate $\chi^{(2)}$ microresonator. *Phys. Rev. Lett.*, 126:133601, Mar 2021.

[74] Jonas H. Weber, Benjamin Kambs, Jan Kettler, Simon Kern, Julian Maisch, Hüseyin Vural, Michael Jetter, Simone L. Portalupi, Christoph Becher, and Peter Michler. Two-photon interference in the telecom c-band after frequency conversion of photons from remote quantum emitters. *Nature Nanotechnology*, 14(1):23–26, Jan 2019.

[75] D. J. Wilson, K. Schneider, S. Hoenl, M. Anderson, T. J. Kippenberg, and P. Seidler. Integrated gallium phosphide nonlinear photonics. *ArXiv e-prints*, August 2018.

[76] Richard Wolf, Ingo Breunig, Hans Zappe, and Karsten Buse. Cascaded second-order optical nonlinearities in on-chip micro rings. *Opt. Express*, 25(24):29927–29933, Nov 2017.

[77] Xiaona Ye, Shijie Liu, Yuping Chen, Yuanlin Zheng, and Xianfeng Chen. Sum-frequency generation in lithium-niobate-on-insulator microdisk via modal phase matching. *Opt. Lett.*, 45(2):523–526, Jan 2020.

[78] Sebastian Zaske, Andreas Lenhard, Christian A Keßler, Jan Kettler, Christian Hepp, Carsten Arend, Roland Albrecht, Wolfgang-Michael Schulz, Michael Jetter, Peter Michler, and Christoph Becher. Visible-to-telecom quantum frequency conversion of light from a single quantum emitter. *Physical Review Letters*, 109(14):147404, 2012.

[79] David E. Zelmon, David L. Small, and Dieter Jundt. Infrared corrected Sellmeier coefficients for congruently grown lithium niobate and 5 mol.% magnesium oxide–doped lithium niobate. *J. Opt. Soc. Am. B*, 14(12):3319–3322, Dec 1997.